Title

EXCITED STATE PRODUCTION IN THIN FOILS FOR NEUTRAL INJECTION IN CONTROLLED THERMONUCLEAR FUSION EXPERIMENTS

Author

Bornstein, Isaac.

Publication Date

1971

Thesis/dissertation

UCRL-20253

EXCITED STATE PRODUCTION IN THIN FOILS FOR NEUTRAL INJECTION IN CONTROLLED THERMONUCLEAR FUSION EXPERIMENTS

Isaac Bornstein
(Ph.D. Thesis)

January 1971

AEC Contract No. W-7405-eng-48

LAWRENCE RADIATION LABORATORY
UNIVERSITY of CALIFORNIA BERKELEY

UCRL-20253

DISCLAIMER

DISCLAIMER

EXCITED STATE PRODUCTION IN THIN FOILS FOR NEUTRAL INJECTION IN CONTROLLED THERMONUCLEAR FUSION EXPERIMENTS

Contents

EXCITED STATE PRODUCTION IN THIN FOILS FOR NEUTRAL INJECTION IN CONTROLLED THERMONUCLEAR FUSION EXPERIMENTS

Isaac Bornstein

Lawrence Radiation Laboratory
University of California
Berkeley, California 94720

January 5, 1971

ABSTRACT

Thin foils have been suggested as a charge-exchange medium for neutral injection into controlled thermonuclear fusion devices. In the experiments described here, the excited state fraction, neutral fraction, and negative beam fractions are measured for deuterons in the energy range $10 < E < 100$ keV for thin carbon foils and for carbon foils with freshly evaporated exit layers of carbon, magnesium, niobium, and gold. Foil lifetimes are also measured for 5 μg carbon foils.

In addition, a review is made of the literature on foil stopping power and scattering from foils.

Foils are shown to have higher excited state yields at energies below 20 keV H^+ than gases or vapors. In particular, carbon foils have a higher excited state yield than the others tested.

I. INTRODUCTION

One method of producing a hot plasma is to inject energetic neutral atoms into a magnetic containment vessel.[1,2] In this method it initially was hoped that sufficient atoms would be ionized by collisions with background gas and trapped in the field to form a plasma. Early experiments[3] showed that at pressures below 10^{-7} torr the trapping efficiency remained constant, rather than decreasing with decreasing pressure. This enhanced trapping was found to be due to Lorentz ionization of atoms in excited states.[4] If a highly excited atom is passed through a magnetic field, the $\vec{V} \times \vec{B}$ force appears in the atom's frame of reference as an electric field which can ionize the atom. For example, with a field of 45 kG, a hydrogen atom with an energy of 30 keV will experience an electric field of 108 kV/cm. This is sufficient to ionize states down to principal quantum number $n = 10$.

In the aforementioned experiment, the neutral particles were formed by dissociating H_3^+ in water vapor. In subsequent experiments, other vapors and gases have been used as neutralizing and excitation media, one of the best at energies of 10 to 30 keV being magnesium vapor.[5] Berkner et al.[6] have made measurements in magnesium vapor and Fig. 1 shows their results for excited state yield and neutral fraction as a function of target thickness at 15 keV and Fig. 2 shows the excited state yield as a function of energy. As can be seen, there is a peak in the excited state curve at a target thickness of 7×10^{14} atoms/cm^2. This is a result of excited atoms being removed from the beam by further collisions with the target gas.

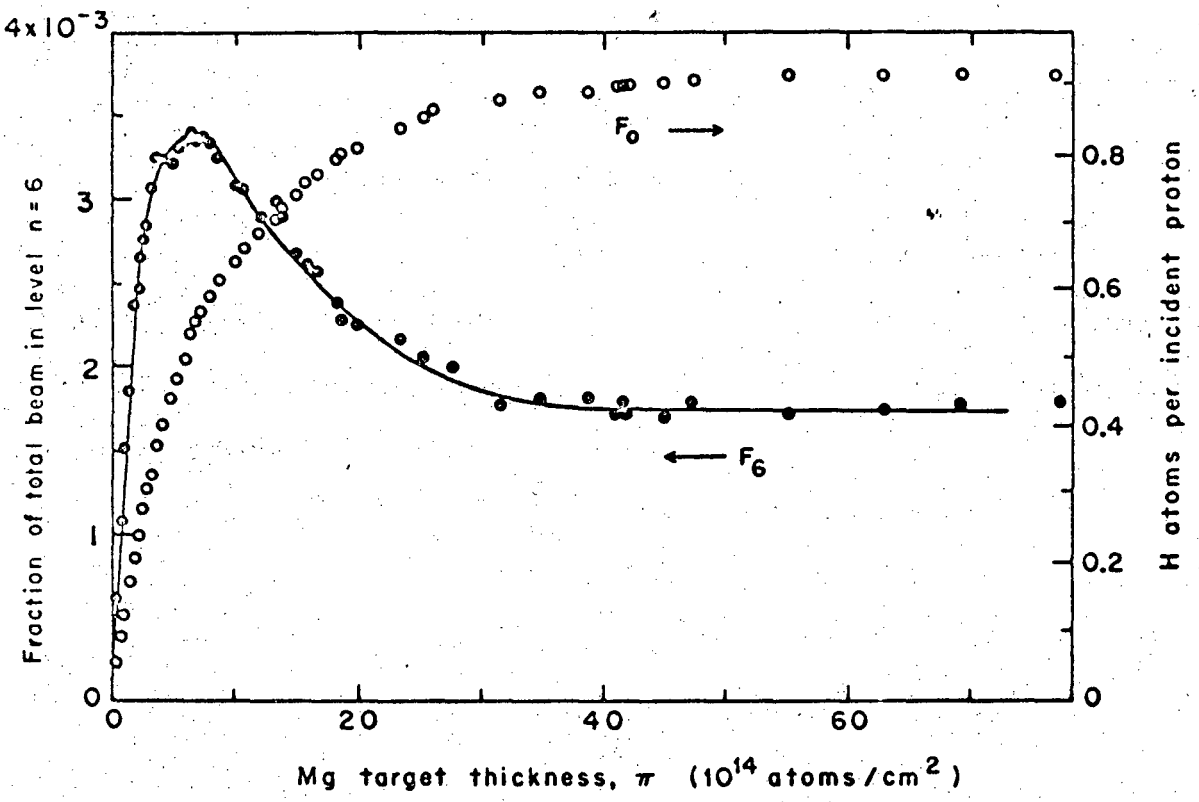

Fig. 1. Excited state yield in the level n = 6 and neutral fraction for protons in magnesium vapor as a function of target thickness (from Ref. 6).

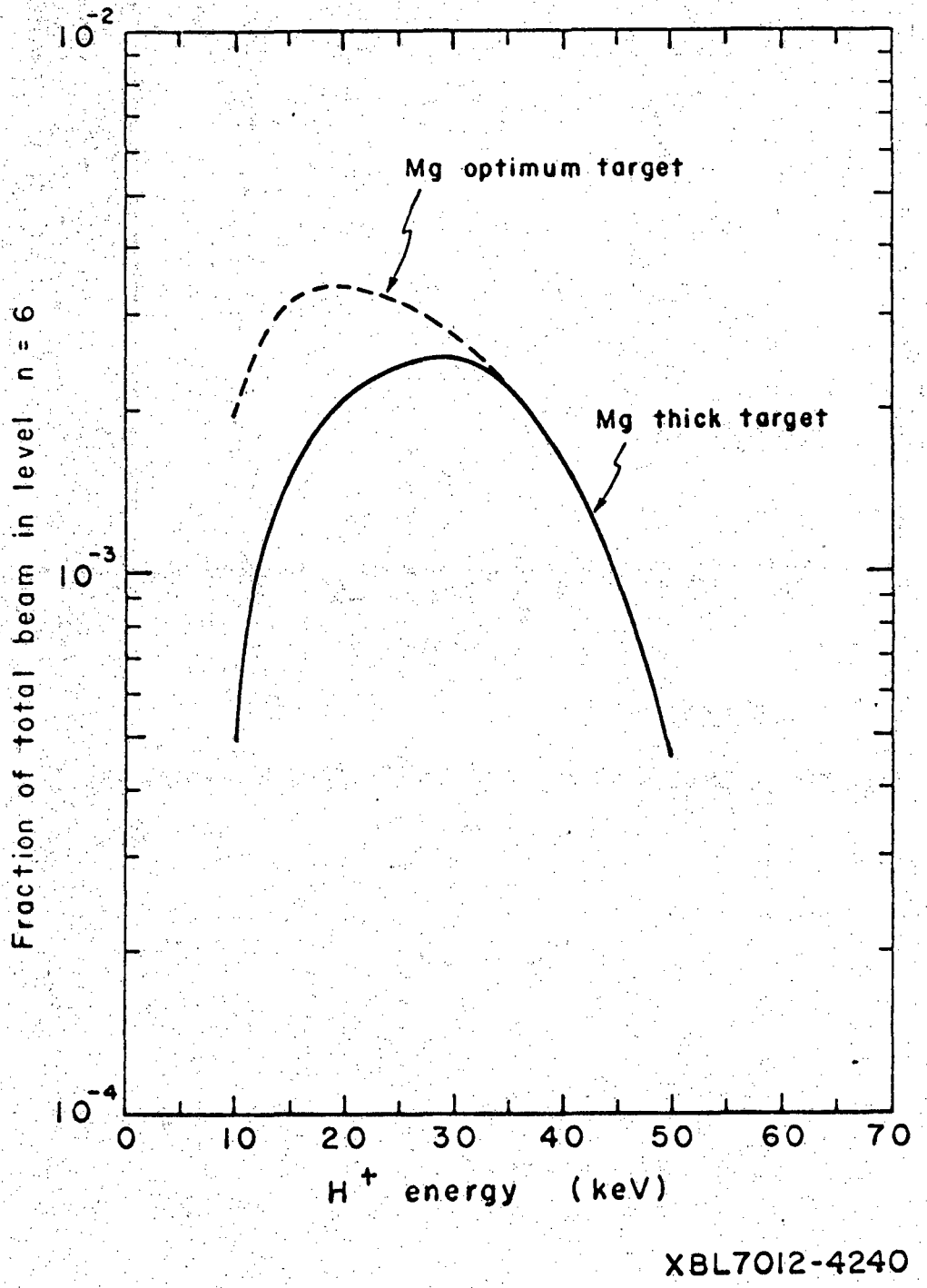

Fig. 2. Excited state yield from Mg vapor as a function of energy (from Ref. 6).

Another charge exchange medium is the thin, self-supporting foil, the thinnest available of which is two or three orders of magnitude thicker than the optimum magnesium vapor target. Very little is known about the mechanism of charge exchange in solids. Trubnikov and Yavlinskii[7] have made a rough calculation which shows that the various n values of the excited states are populated according to the same n^{-3} scaling which applies to gases. McLelland[8] has proposed a different model which roughly fits the experimental results, and also predicts n^{-3} scaling.

Experimentally, it was originally observed that all foil materials gave the same output neutral fraction. Then, in 1955, Phillips[9] showed that the neutral fraction was strongly dependant on the exit surface of the foil. What had previously been measured was the neutral fraction attributable to surfaces contaminated with adsorbed gases or diffusion pump oil. By depositing fresh layers on a foil under a high vacuum he was able to measure the neutral fraction from the foil and watch it approach that of "dirt". It was Phillips' experiments that demonstrated the need for high vacuum and clean foil exit surfaces; in these experiments at a pressure of 10^{-6} torr a monolayer of background gas will build up in one second and equilibrium will be established in a few minutes.

In 1964, Sweetman et al.[10] at Culham Laboratory measured the yield at the level n = 11 from a carbon foil for 20 to 100 keV H^0 atoms and reported that it exceeded the yield from a hydrogen gas target. It was this increased excited state yield that formed the motivation for the further study of foils as a charge exchange medium.

Kaminsky[11] has shown that in the case of 0.6 to 2 MeV $^{3}He^{+}$ through monocrystalline copper foils, axial channeling can have a marked effect on the charge states emerging from a foil. Further investigation of the effect of channeling on excited state yields would be interesting.

In my experiment, I have measured excited state yields from several foil materials. Beryllium foils were used initially, but because of toxicity problems, carbon was chosen as a substrate. It is commercially available[12] in various thicknesses. Clean carbon was evaporated in order to compare clean and dirty foils. Magnesium was chosen because of the effectiveness of magnesium vapor, gold to give another comparison with the data of Phillips, and niobium because it has a low sputtering yield[13] and would hopefully give a longer lasting foil.

Besides higher excited state yields, foils have the advantage over gases in that they do not introduce a heavy pumping load due to gas streaming out of the neutralization chamber. Foils do have some disadvantages, namely increased scattering of the beam, sputtering, and the tendency to "burnup". I have made some measurements on foil lifetimes, and the other two problems are discussed in appendices.

II. PRESENT THEORY ON EXCITED STATE PRODUCTION

Very little theoretical effort has been expended on neutralization and excited state production in foils, with the result that little is known of the mechanism by which they occur. I am aware of only three papers that have been published on this topic in recent times, two of them by the same group. Yavlinskii, Trubnikov, and Elesin[14] have assumed that the recombination process takes place at the exit of the foil because the Debye shielding length inside a metal foil is so short that the protons are too well shielded to caputre an electron. At the surface of the foil, the proton captures an electron forced out of the metal under the influence of the electron pressure within. The capture is treated along the lines of the ion-ion recombination theory of Langevin. In the case $V_p \ll v_0$ they obtain

$$F^+ = \exp\left[-\sqrt{\frac{436}{E_p}\left(\frac{n_0}{10^{22}}\right)^{1/3}}\right],$$

where V_p = proton velocity

v_0 = velocity at Fermi surface

n_0 = electron density (cm^{-3})

E_p = proton energy (keV)

F^+ = positive fraction of emerging beam

In the case $V_p \gg v_0$

$$F^+ = \exp\left[-\frac{6.5}{E_p}\left(\frac{n_0}{10^{22}}\right)^{1/2}\right].$$

In comparing their calculations with Phillips'[9] data (see Fig. 3)

Fig. 3. Proton fraction of beam at exit of a metal foil as a function of energy (theoretical and experimental studies). A, Ref. 7, theoretical study; B, Ref. 9, experimental data for silver; C, Ref. 14, theoretical study assuming proton velocity less than that of electrons at Fermi surface; D, Ref. 14, theoretical study assuming proton velocity greater than that of electrons at Fermi surface.

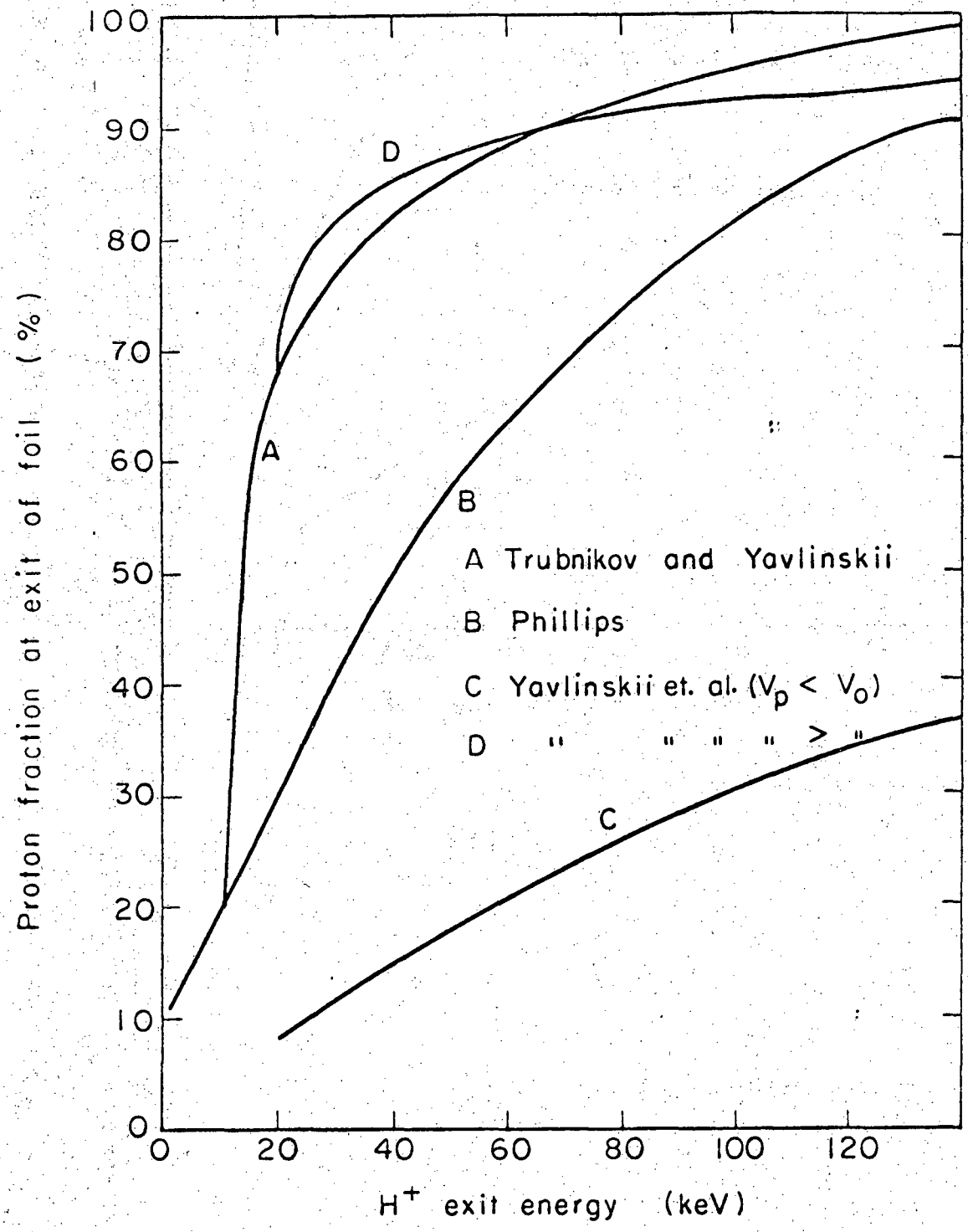

XBL7012-4229

Fig. 3

Yavlinskii et al. state that the energy range covered corresponds to values of V_p/v_0 between 1.75 and 7 and therefore the experimental result should and does fall between their curves.

In a later paper, Trubnikov and Yavlinskii[7] consider the case of tunnel recombination near the surface of a metal foil. The recombination process is assumed to be the result of a tunnel transition of an electron in the metal to a level in an atom that has the same energy. Previous workers had carried out the calculation in two parts; first, the ion was considered to be at rest some distance R from the surface and the transition probability was calculated using time-independant perturbation theory. Then, these individual probabilities were integrated over the range of R to obtain the overall probability. This approach, called the "fixed ion approximation" (it is essentially the assumption that $V_p \ll v_0$), leads to the following results

$$w_1 = 0 \quad \text{(transition to the ground state is impossible)}$$

$$w_2 = 1 - \exp\left(-\frac{0.2e^2}{\hbar V_p}\right)$$

$$w_3 = 1 - \exp\left(-\frac{0.08e^2}{\hbar V_p}\right)$$

w_4 and higher are insignificant

where w_i is the transition probability to the state n = i.

Trubnikov and Yavlinskii maintain that the above approach is inconsistant as the motion of the ion is not taken into account. Therefore, they use time-dependant perturbation theory to calculate w_1 for the case $V_p \gg v_0$, the result being shown in Fig. 3 (this is actually a plot of $1 - w_1$). The fact that the calculated values of w_1 are smaller than the observed values is explained by the presence of other

recombination processes including tunneling to lower levels and the process considered in their previous paper. Finally, Trubnikov and Yavlinskii show that the various excited states are populated according to

$$w_n = \frac{w_1}{n^3} .$$

McLelland[8] maintains that the assumptions of Yavlinskii, Trubnikov, and Elesin, namely Debye shielding and the applicability of Langevin's theory, would make their results inapplicable to semi-metals such as graphite. He therefore performed calculations based on two different methods of recombination. First he considers recombination with conduction electrons and reports that the calculated yield of both excited and neutral atoms falls off much more sharply than the experimental results. Next he considers a free electron model in which the proton gives rise to an internal shower of positive energy electrons. Some of these will have velocities close to that of the proton and will thus be candidates for possible capture. Using this model he derived the equation

$$N_n = \frac{2^7 \pi \lambda^7 V_0^2 M m_p a}{\hbar^2 n^3 m_e k_p} \frac{N}{\Omega d^2} \int d\underline{k}_e \frac{1}{K_e} |h_\alpha(k_0)|^2 \frac{1}{k_e} f(E) \left\{ \frac{\sin\left[(K_{oz} - K_e)a\right]}{(K_{oz} - K_e)a} \right\}^2 \frac{1}{\left\{ \left[\frac{m_p}{M} (K_{oz} - K_e) \right]^2 + \frac{\lambda^2}{n^2} \right\}^4}$$

where

λ = inverse Bohr radius

V_0 = depth of electron-lattice potential well

$M = m_e + m_p$

m_e = electron mass

m_p = proton mass

a = thickness of foil

k_p = proton wave number

N = total number of electrons available for capture

Ω = total solid angle from which capture takes place

d = transverse dimension of foil

k_e = electron wave number

K_e = electron wave number in center of mass

$f(E) = \frac{1}{35^2} Ee^{-E/35}$ = electron energy distribution

K_{oz} = z-component of initial wave number in center of mass

$$h_\alpha(k_0) = \frac{1}{4\pi} \int d\underline{r} \frac{e^{-\alpha r}}{r} e^{i\underline{k}_0 \cdot \underline{r}} \frac{e^{ik_0 r}}{r}$$

α = screening factor in the Coulomb potential

k_0 = initial wave number of the reduced mass

In Fig. 4 are plotted his results for the two models. The curves are normalized to 1 at a proton energy of 20 keV as the term $(N/\Omega d^2)$ cannot be calculated exactly. McLelland also reports a n^{-3} distribution among the various states. In a later section I will show his theoretical results compared to various experimental results.

Thus the theory for excited state production in solids is in much worse shape than the theory in gases. McLelland's theory applies only

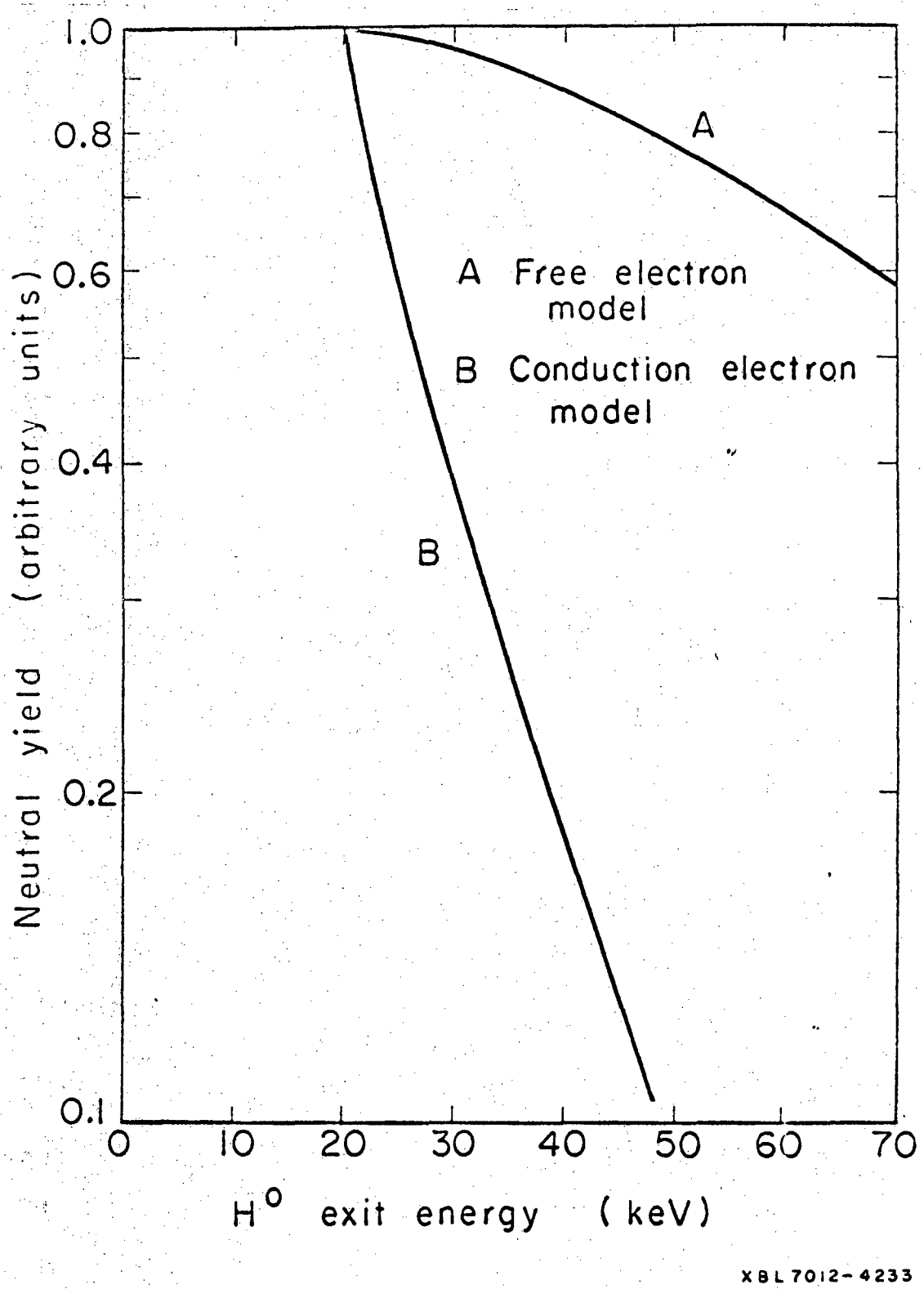

Fig. 4. Theoretical results for excited state yields and neutral fractions by McLelland.[8] Results are shown normalized to 1 at 20 keV. A, free electron model; B, conduction electron model.

to semi-metals and not to metals where conduction electrons play a more important role. It would also be interesting to see what his theory predicts at proton energies below 20 keV. The theories of Yavlinskii et al. and Trubnikov and Yavlinskii are incomplete in that they do not smoothly cover the energy range of interest or they do not consider all processes involved. No one has considered the effect of channeling on excited state production.

III. EXPERIMENTAL INVESTIGATION

A. Apparatus

A block diagram of the apparatus used is shown in Fig. 5.

1. Accelerator

The accelerator used for the experiments described herein is a Texas Nuclear Corporation Model 9500 Research Series Accelerator. This accelerator consists of an rf ion source, a 150-kV power supply, and various beam focusing devices. Ions produced in the rf source are extracted through the high-voltage canal with a 0 to 5 kV extraction potential. If desired, the beam can now be pulsed by means of a pair of plates immediately after the canal. An einzel lens provides initial electrostatic focusing for the beam as it exits the source and then is accelerated to the desired energy. All energy measurements were made through a calibrated voltage divider attached to the extractor. In the drift tube following the acceleration column are a set of vertical and horizontal deflectors followed by a dual electrostatic quadrupole lens. The accelerator is pumped by a liquid-nitrogen-baffled oil diffusion pump. To prevent pump oil from contaminating the later sections of the vacuum system, a narrow pumping impedance was placed in the beam tube immediately after the pump. All vacuum seals in the accelerator are made with rubber O-rings.

2. Magnet and Beamline Pumps (Fig. 6)

The switching magnet serves two purposes. First, it momentum analyzes the beam, allowing one to choose between H^+, H_2^+, H_3^+, or whatever else might be in the beam. In addition it allows two separate experiments to be constructed in the experimental area without

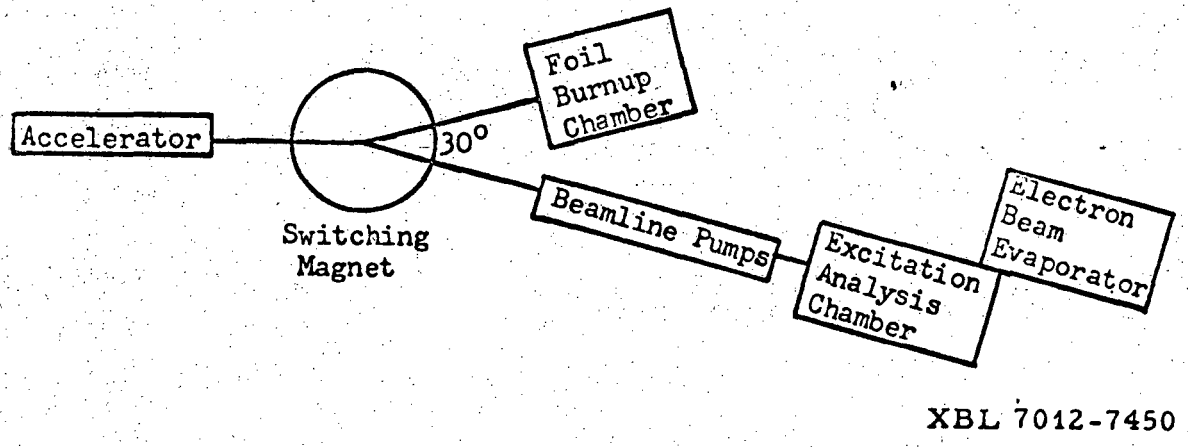

Fig. 5. A block diagram of the apparatus.

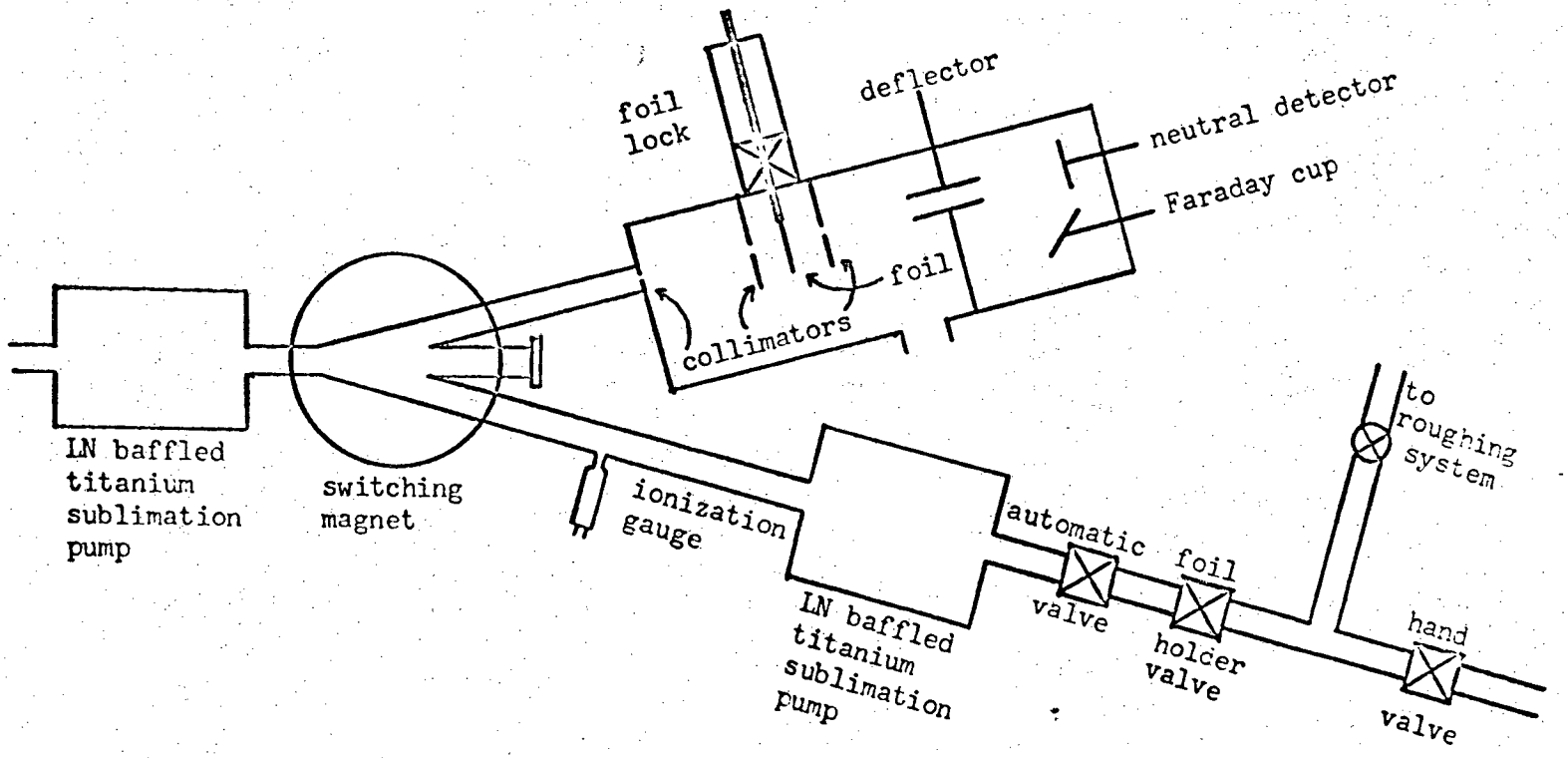

Fig. 6. Switching magnet, beamline pumps, and foil burnup chamber.

disturbing each other. A neutral port is provided for studies involving the whole beam or neutrals. In order to prevent contamination of the high vacuum in the excitation analysis chamber, two liquid-nitrogen-baffled titanium sublimation pumps are used on the beamline. These periodically evaporate a fresh layer of titanium on a liquid-nitrogen-cooled surface and are used to trap any oil that might come from the accelerator and maintain a beamline pressure in the range of 10^{-7} torr. Should the pressure rise too high, resulting from a failure of the accelerator pumps or a broken source, the automatic valve will close to protect the analysis chamber. If one desires to experiment with neutrals, a neutralizing foil can be placed in the foil holder valve and a magnet can be used to sweep away all the charged particles. The beamline section can be roughed using the roughing system of the analysis chamber, which is a clean roughing system using no mechanical pumps. All vacuum seals in this section are made with copper gasketted Varian flanges.

3. Excitation Analysis Chamber (Fig. 7)

This chamber constitutes the ultrahigh vacuum section of the system; normal operating pressure is approximately 2×10^{-9} torr. To achieve this high vacuum, several different pumping systems are used. Initial roughing to a vacuum of about 25 in. of mercury is done with an "aspirator."[15] This is a device very similar to a perfume atomizer in which nitrogen gas at 80 psi is flowed past an orifice leading to the vacuum system. In addition to providing an oil-free high-pressure roughing system, the aspirator will tend to make nitrogen the major component of the remaining gas, hence simplifying further pumping. To

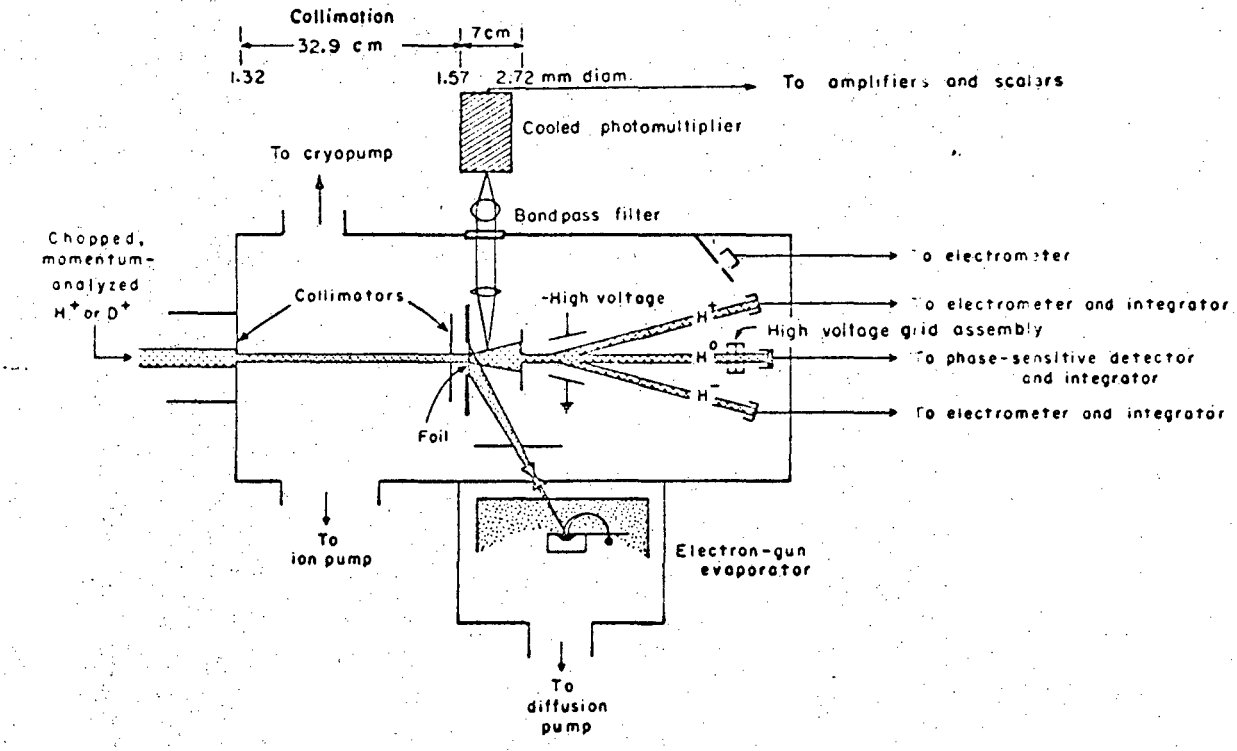

Fig. 7. Excitation analysis chamber (inset shows collimation).

lower the pressure to approximately 5 microns, liquid-nitrogen-cooled sorption pumps are used. At this pressure, the gate valve to the ion pump can be slowly opened and the pressure lowered to the high 10^{-8} torr range. By baking the system at a temperature of 250°C the pressure was further lowered to about 2×10^{-8} torr. To facilitate baking, a quartz heating lamp was permanently installed in the chamber. The liquid-helium cryopump[16] consists of an outer liquid-nitrogen baffle and shield, and an inner container of liquid helium. Filling the nitrogen shield lowers the pressure to 9×10^{-9} torr, and adding liquid helium lowers the pressure further to 2×10^{-9} torr. This pressure is lower than the base pressure of our ion pump and therefore the pump is closed off at this time.

Carbon foils[12] are positioned in the beamline by means of a foil lock containing a bellows seal. When fully retracted the foil lock can be closed off from the system and it can be pumped down or let up to air through a series of needle valves leading to the roughing system. In this manner, foils can be changed without affecting the vacuum in the main system. To prevent the need for excessive foil changing, the foil holders were designed to hold as many as three 1/4-in. diameter foils at a time.

The beam entering the chamber is collimated twice, passed through the foil, collimated again and electrostatically deflected to analyze the charge components. The positive and negative components are collected by Faraday cups connected to Keithley Model 410 picoammeters. A block diagram of the electronics is given in Fig. 8. The neutral particles are collected by a pyroelectric crystal detector.[17] With

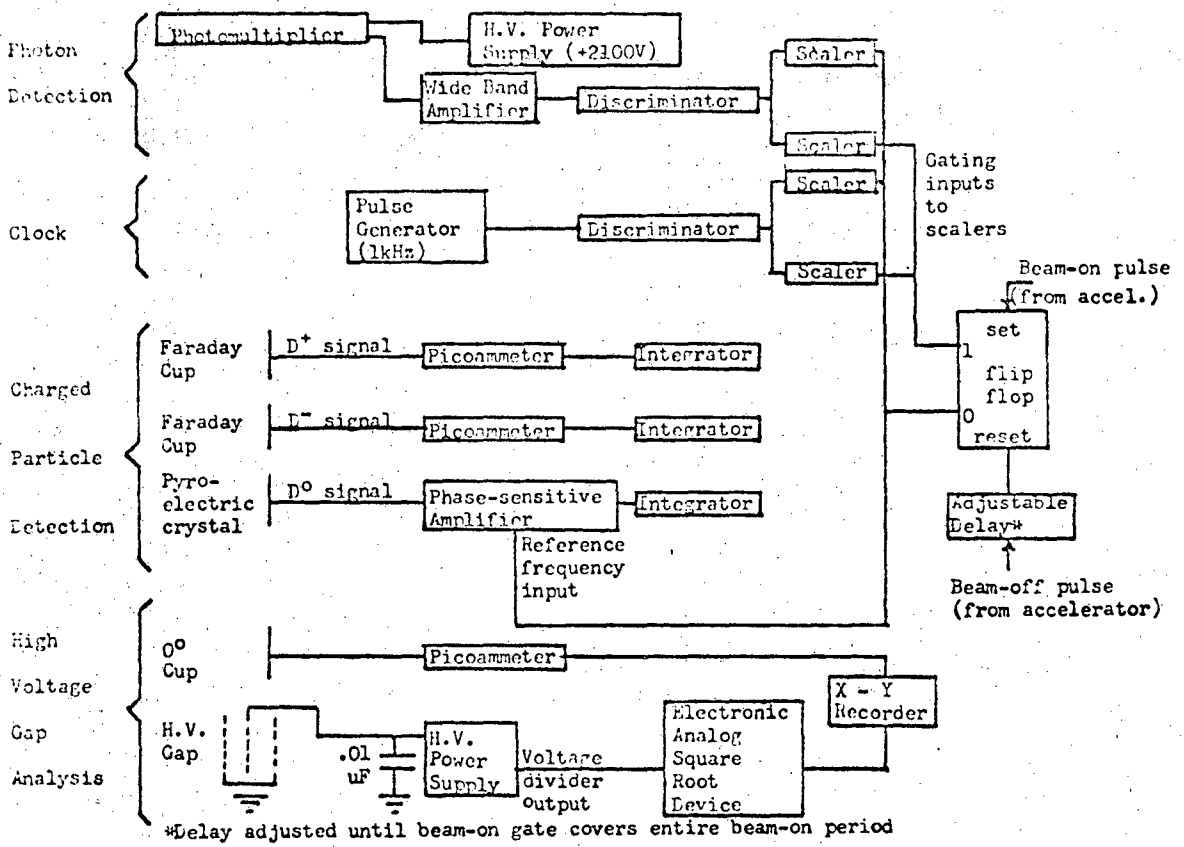

Fig. 8. A block diagram of the electronics.

the current available, at beam energies below 20 keV, the pyroelectric crystal is not sufficiently sensitive to give accurate readings and is replaced by a lithium-drifted surface-barrier detector, using the same electronics as did the pyroelectric crystal and therefore monitoring mean current. There is an additional Faraday cup covered with a narrow collimating slit; measuring the relative deflection voltages needed to bring the beam into the cup both with and without a foil, one can determine the energy loss in the foil. All the Faraday cups and the neutral detector are situated in a transverse magnetic field of about 400 gauss to suppress spurious currents caused by secondary electron emission.

Two different methods were used to measure excited state yields in these experiments. The first method was to count the de-excitation photons at 4101 Å resulting from the decay of the n = 6 level of neutral hydrogen. Originally, a monochromator was used to view the photons,[18] but size limitations placed the monochromator slit far from the beam with resulting loss of efficiency. Therefore, a new optical system was designed around a bandpass filter. As it was desired to obtain the maximum light transmission to the phototube, the front lens of the optical system was placed in a window recessed into the chamber and only 2 in. from the beamline. The rest of the system consisted of a second lens to focus the light on the photocathode of the phototube and a bandpass filter with 83.5 Å width about 4101 Å. A EMI type 6256S phototube, cooled to -20°C to remove background noise, was used to count the photons. Thermal insulation was placed between the phototube and the optical system to prevent frosting of the lenses and

filter.

The other method used was to electrostatically ionize the atoms in a strong electric field and measure the resulting current.[19] A high voltage gap was designed consisting of three grids of 96% transparent tungsten mesh, 7/8 in. in diameter. The outer pair are grounded and the inner one can be set at any desired potential. The grids are spaced 1/8 in. apart on the upstream side and 5/16 in. on the exit side. Voltages up to 15 kV could be applied without sparking, which is equivalent to 50 kV/cm. As will be shown in Appendix A, the excited state yield is proportional to the slope of the de-excitation current plotted vs the square root of the voltage. An electronic analog square root device was connected to a voltage divider output of the high voltage power supply, and its output connected to an X-Y recorder. The other axis was driven by the output of a Kiethley 410 picoammeter connected to the neutral cup. A plot was obtained by running the power supply up to 9 kV and then shutting it off with the recorder running. To lengthen the voltage decay time to 5 sec, a 0.1 μF capacitor was attached across the high-voltage supply. It was found that the slope obtained depended on the polarity of the high voltage used. The negative voltage was shown to give slopes 25 to 13% low, due to beam steering, in the energy range 30 to 100 keV.

4. Electron Beam Evaporator

In order to place fresh surfaces on the rear of the foils, an electron beam evaporator was hung on the rear of the analysis chamber. The filament is maintained at a positive potential of 6 kV and the resulting electron beam is focused and bent by a pair of permanent magnets into a crucible placed in a depression in the water-cooled copper base

of the evaporator. Evaporator power is continuously adjustable up to 3 kW, allowing one to evaporate most materials, including niobium and carbon. A series of collimators aim the evaporated material through a valve to the back of the foil. Due to the collimation, the analysis chamber pressure rises only to the low 10^{-8} torr range during evaporation and falls rapidly as soon as the valve is closed. The evaporator is pumped by a liquid-nitrogen-baffled 6-in. oil diffusion pump and has water-cooled shields and a liquid-nitrogen baffle in the evaporating region itself. A shuttered viewing window is provided for observing the evaporation and to allow replenishing of the evaporant without totally dismantling the unit.

5. Foil Burnup Chamber (Fig. 6)

At the beam levels of this experiment, the foils had a very long lifetime. In actual applications, the beam levels would be much higher and it was desired to obtain some measure of what the foil lifetime would be. In order to obtain beams of sufficient intensity to "burn up" a foil in a reasonable length of time, it was necessary to construct a chamber closer to the accelerator than the analysis chamber. Beam intensity in the burnup chamber was on the order of microamperes through a 1/16 in. diameter hole, or hundreds of microamperes per square centimeter. An initial collimator was used to keep the relatively poor vacuum of the chamber from contaminating the beamline. The beam is then collimated, passed through the foil, and collimated again. Charged particles are then deflected into a Faraday cup and neutrals are detected by the secondary emission from a flat plate. Small permanent magnets attached to the Faraday cup suppress secondaries on

it. The neutral detector is monitored by a Keithley model 410 pico-ammeter whose output is used to drive a strip chart recorder. The breakage of the foil is noted by the sudden drop in the neutral signal. The chamber is pumped by a liquid-nitrogen-baffled oil diffusion pump and has a base pressure of 2×10^{-6} torr.

B. Experimental Procedure

1. Optical Method

The basic quantity being measured is the photomultiplier counts per particle detected. The acceptance angle of the optical system is such that it will observe a much wider spread of beam than will be passed by the final collimator. As scattering from the foil increases, the particle detection rate will drop and the counts per particle will rise even with no change in the excited state yield. Thus the efficiency is a function of beam scattering and it is necessary to measure it every time conditions change, which for practical purposes means every time a foil or energy was changed and after each evaporation. In order to obtain the optical efficiency of the lens system, one first measures a known reaction yield. The known reaction used for the calibration was the excitation and subsequent decay of N_2 gas by proton beams. The optical band head from this decay is at 3914 Å, which is sufficiently close to the 4101 Å hydrogen line for the relative efficiencies of the optical system to be the same at the two wavelengths. Nitrogen gas was bled into the analysis chamber through a needle valve and the pressure measured with an ionization gauge, which was calibrated against a capacitance manometer. With the foil in place and the 3914 Å filter in the filter drawer, four sets of measurements were taken at pressures between 2×10^{-6} and 9×10^{-6} torr (the measurements are identical to those taken with the 4101 Å filter and will be described later). After the measurements are completed, the needle valve is closed and the system allowed to pump down to its base pressure. The 3914 Å filter is removed and the 4101 Å filter is placed in the filter

drawer.

As a preliminary, the deflection voltages necessary to bend the beam into the slit cup are measured. From these and the acceleration potential, one can determine the exit energy from the foil. From the energy loss in the foil and known stopping power cross sections, (see Appendix D) one can estimate the thickness of the foil.

The basic quantities to be measured are the positive current emerging from the foil, the negative current, the neutral beam equivalent current, and the photon count from the photomultiplier. Since the pyroelectric neutral detector is an energy-sensitive device, it is necessary to calibrate it by repeating the measurements with the deflection voltages off. In this manner the known charged beams could be added to the neutral beam and the resultant sum measured. From this sum the calibration factor of the neutral detector is calculated. The neutral detector also requires a beam which is slowly pulsed at 10 to 15 cycles/sec. A gating logic circuit was arranged to allow a set of counters to be turned on and off as the beam was pulsed.

Essentially, therefore, there were seven basic measurements. First, a pair of gated counters were attached to a one kilocycle per second oscillator and used to measure the total on and off times of the beam. Another pair of gated counters are attached to the photomultiplier tube. The beam-off counter in that case is a measurement of background noise in the optical system. The three remaining measurements are the integrated outputs of the particle counters. When the deflecting voltage is turned off, the measurements are repeated except, of course, for the charged particle counters, which now read zero. In

general, these sets of measurements were repeated several times.

Measurements taken with the deflection voltage off are used to calibrate the neutral detector so that one can obtain a total particle flux. Dividing this into the photomultiplier counts, one obtains the count rate per detected particle. In the case of the nitrogen calibration, one can compared this count rate with the known excitation cross section to obtain the system's optical efficiency. Knowing the efficiency, one can then get the excited state yield from the count rate in a second set of measurements. The method and theory of obtaining the excited state yields is discussed further in Appendix A.

2. Electric Gap Method

This method has the advantage of being simpler and more direct. There is no need for lengthy calibrations of the optical system nor for having the beam pulsed all the time. To start off, the exit beam energy is measured as before. Then a reading is taken of the charged currents with the deflection voltage on, and again, using the neutral detector as a Faraday cup, with the deflection voltage off. This latter measurement gives the transmission of the grid assembly and the collimator in front of the neutral detector. The beam pulser is turned on and the neutral detector is read with the deflection voltage on and off, in order to obtain a neutral fraction. With the pulser off, the gap power supply is turned on to 9 kV and the scales of the X-Y recorder are properly set. The square root of the gap voltage is fed to the Y-axis while the ionized current in the neutral port goes to the X-axis. With the pen down on the paper, the gap power supply is turned off and the slowly discharging capacitor across the supply allows the recorder

to obtain a plot of root E vs I. As will be shown in Appendix A, the excited state yield is proportional to the slope of this plot if we assume that the excited state populations are proportional to n^{-3}.

3. Evaporation

Before evaporating, the liquid-helium cryopump is filled with one or two inches of liquid helium, allowing the analysis chamber to settle to its lower pressure. The pot of evaporant is heated at a power below that required for evaporation to allow it to outgas, and then a small liquid-nitrogen trap in the line between the evaporation chamber and the analysis chamber is filled. Using the positive beam as a monitor, through the foil, the evaporator is raised to the proper power level, the shutter valve between the chambers is opened, and the evaporation commences. When the beam current drops by 30 to 50%, which usually takes about one minute, the shutter is closed and the evaporator turned off. At this point the sequence of measurements is begun again.

4. Foil Burnup

Using the switching magnet, the beam is routed to the 15° west beamline and is tuned for maximum intensity in the Faraday cup. The neutral detector output is monitored by a Keithley 410 picoammeter which in turn runs a strip chart recorder. The initial beam current is noted, the recorder started, and a foil inserted in the beam path. When the foil breaks, as indicated by a drop in the neutral signal, the foil is removed and inspected. During irradiation the beam current is held constant ± 10 percent. Note that a change in beam intensity will affect both neutral and charged components in the same

direction, while a break in the foil will increase the charge component and decrease the neutral component.

IV. RESULTS

A. Excited States and Charge States

The measured excited state fractions for "dirty" carbon foils are shown in Fig. 9, for "clean" carbon in Fig. 10, for magnesium in Fig. 11, for niobium in Fig. 12, and for gold in Fig. 13. The experimental error is ±37% in the optical method and ±19% in the high-voltage gap method. The sources of error are discussed in Appendix C. The curves are drawn only to guide the eye and have no other significance. As can be seen, the results of the high-voltage gap and optical methods are in agreement with each other, and with the results of Sweetman et al.[10] and Berkner et al.[18] for carbon. A comparison with McLelland's theory is shown in Fig. 14.

The corresponding neutral fraction curves for carbon, magnesium, niobium, and gold are shown in Figs. 15 through 18 and the negative beam fractions are shown in Figs. 19 through 22. For those foils for which other data[9,20] are available, the agreement is good.

From these results it seems that at low energies (< 15 keV D^+) a dirty carbon foil provides the best charge-exchange medium. This is fortunate as carbon foils are easily obtainable, and it is relatively difficult to keep a foil clean for any long period of time. While making low-energy measurements on magnesium, it was found that with a background pressure of 1×10^{-8} torr the excited state yield would change from that characteristic of Mg to that characteristic of dirty carbon in a period of about an hour, as shown in Fig. 23. At low energies in magnesium the excited state yield of considerably lower than in dirty carbon and the negative fraction is considerably higher.

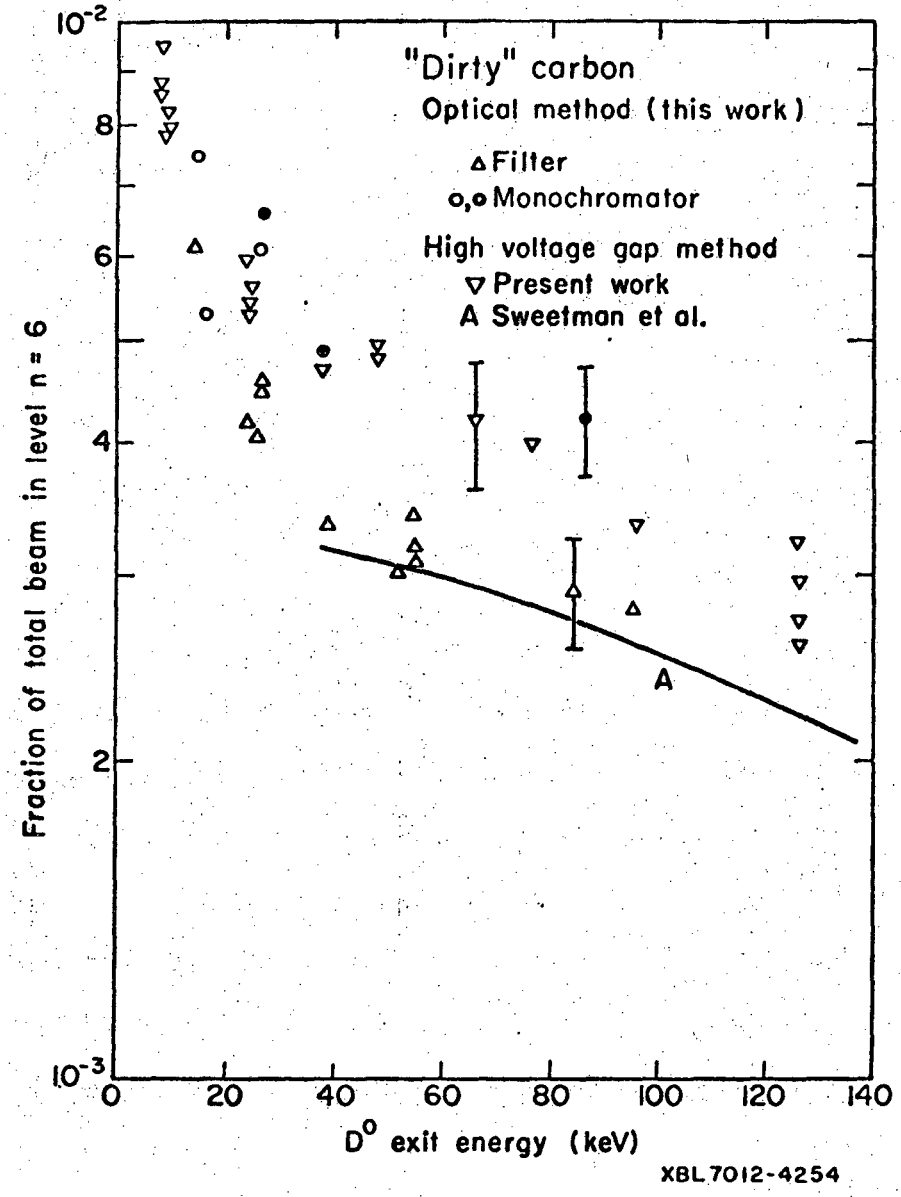

Fig. 9. Excited state yield from a "dirty" carbon foil. Optical method: △, present work, using a filter system; o, •, Ref. 18, using a monochromator (• are proton results plotted at twice the proton energy). High-voltage gap method: ▽, present work; A, Ref. 10, extrapolated to n = 6 using n^{-3} rule. Estimated random uncertainties are indicated at representative points. Systematic uncertainties are estimated to be ±35% in the optical method and ±10% in the high-voltage gap method.

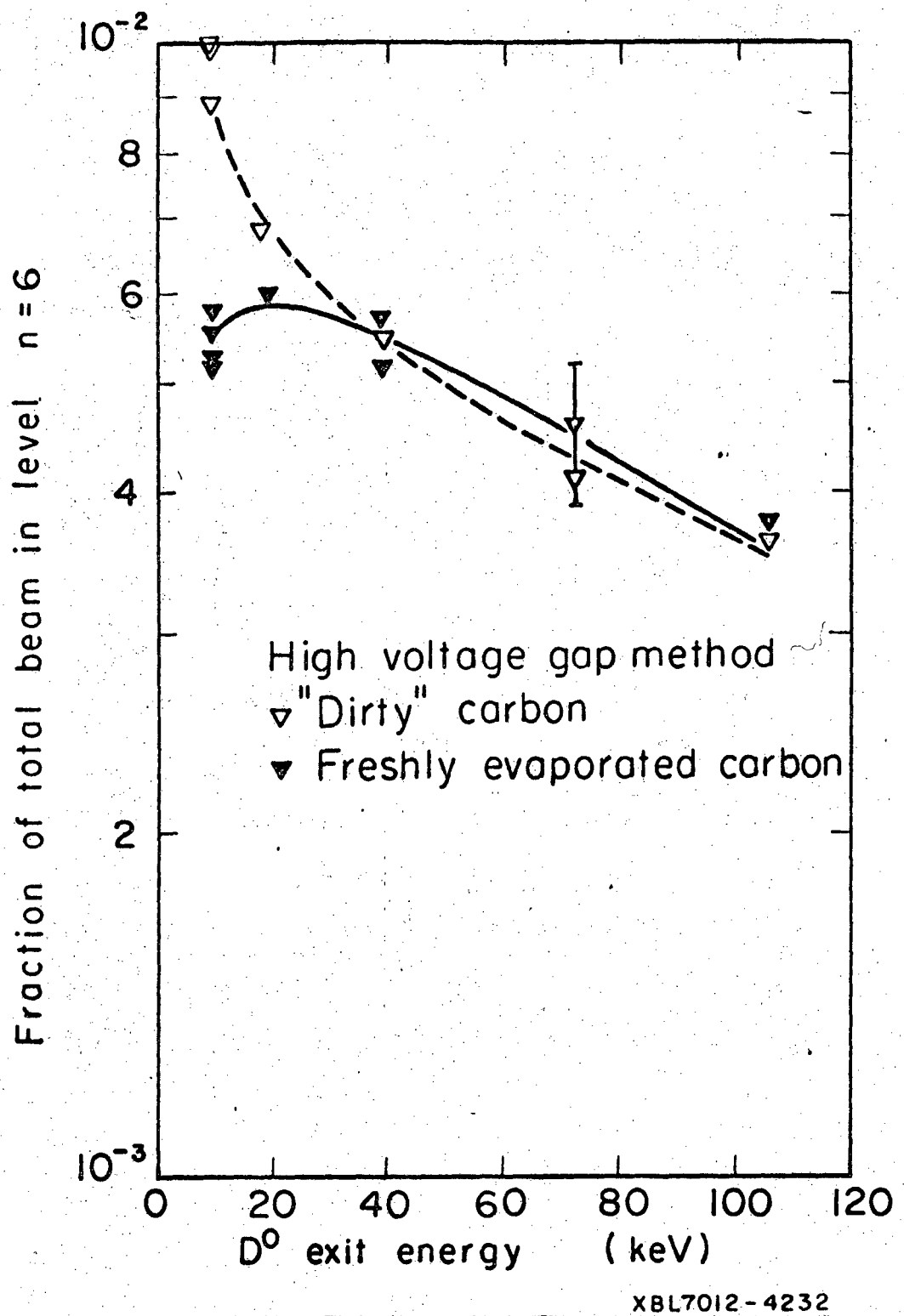

Fig. 10. Excited state yield from "dirty" carbon as compared with that from freshly evaporated carbon using high-voltage gap method. The estimated random uncertainty is shown at a representative point. The lines have been drawn to guide the eye and have no other significance.

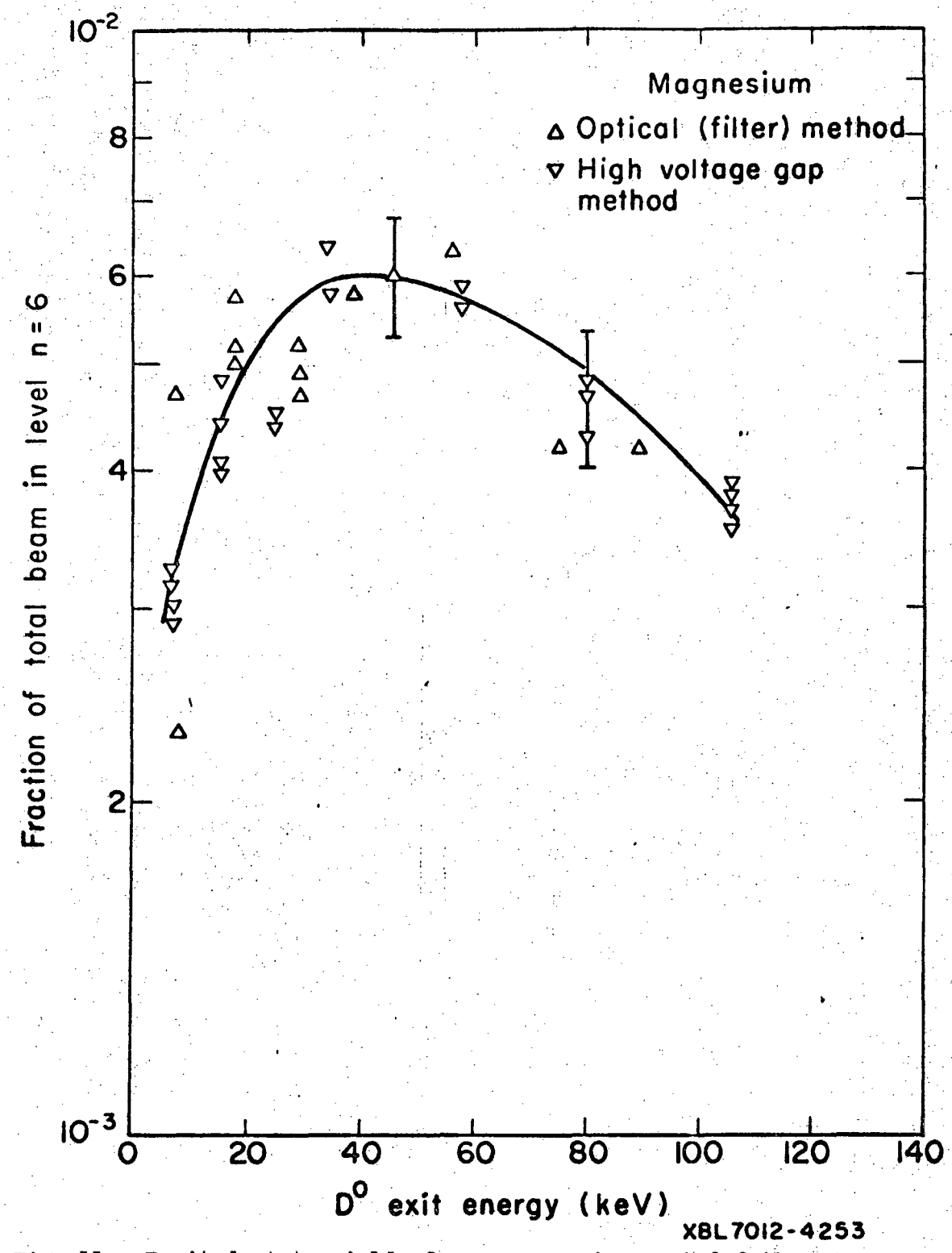

Fig. 11. Excited state yields from a magnesium-coated foil: Δ, optical method; ∇, high-voltage gap method. Estimated random uncertainties are indicated at representative points. The line has been drawn to guide the eye and has no other significance.

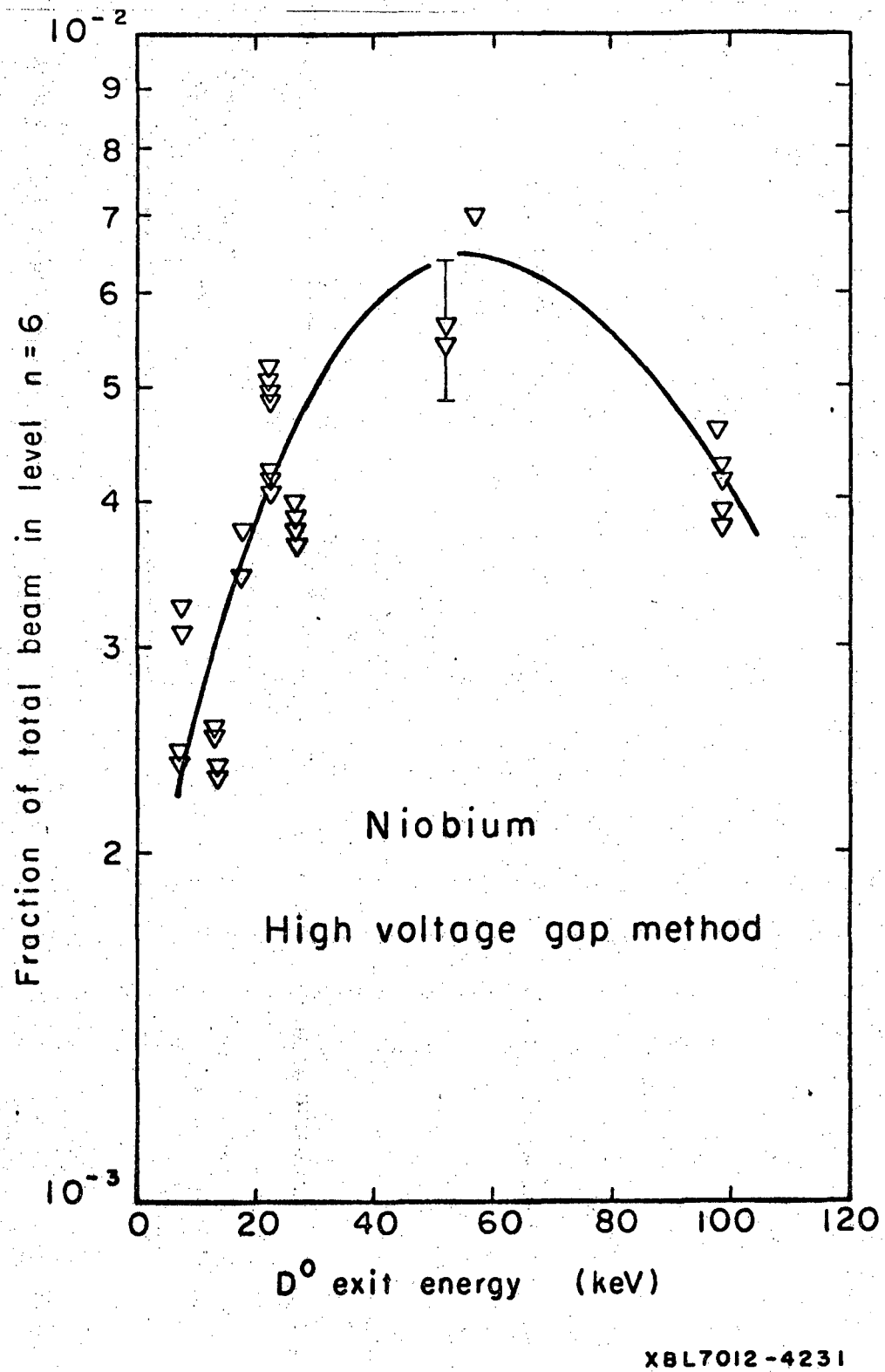

XBL7012-4231

Fig. 12. Excited State yields from a niobium-coated foil using the high-voltage gap method. Estimated random uncertainty is shown at a representative point. The line has been drawn to guide the eye and has no other significance.

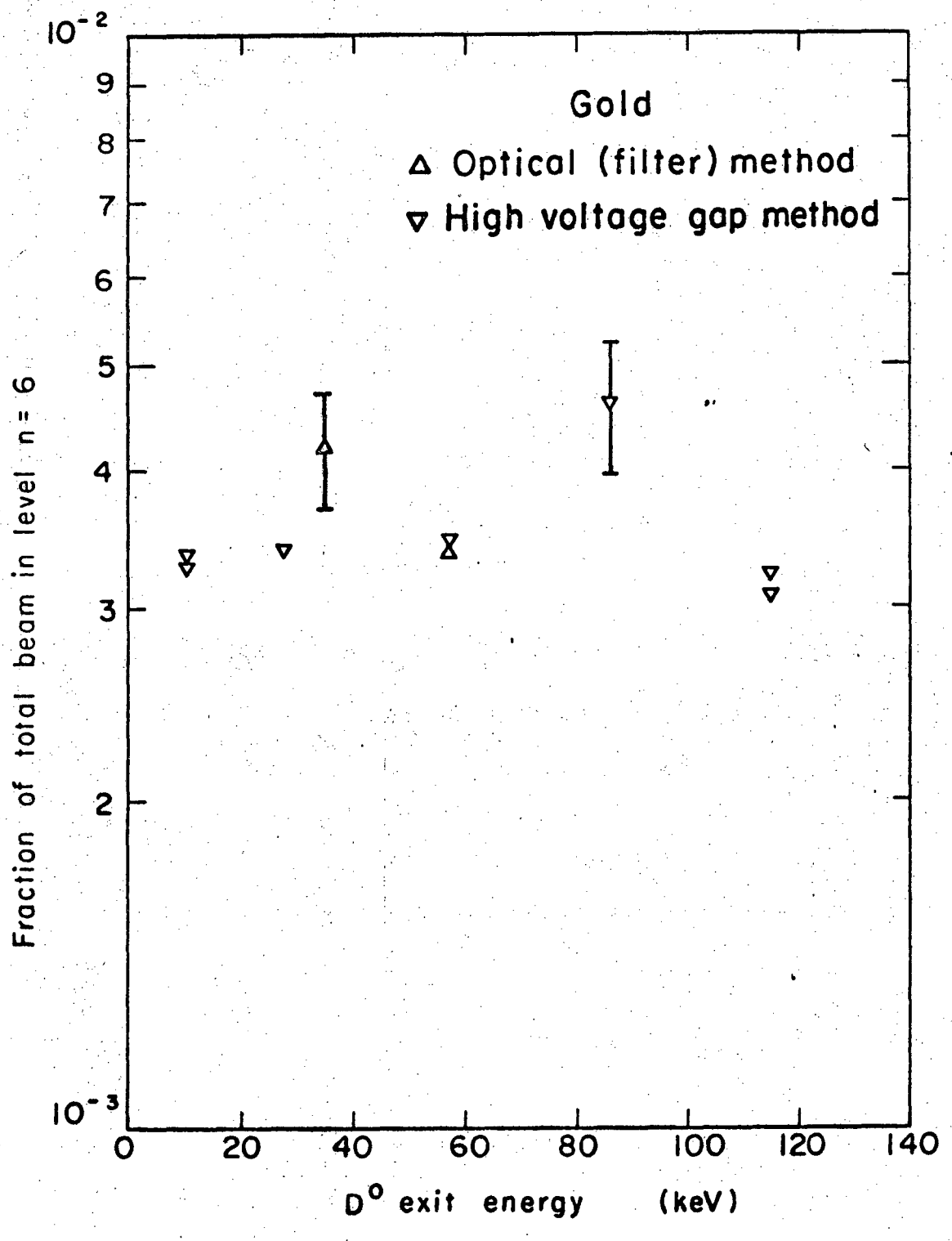

XBL 7012-4252

Fig. 13. Excited state yields from a gold-coated foil: Δ, optical method; ▽, high-voltage gap method. Estimated random uncertainties are shown at representative points.

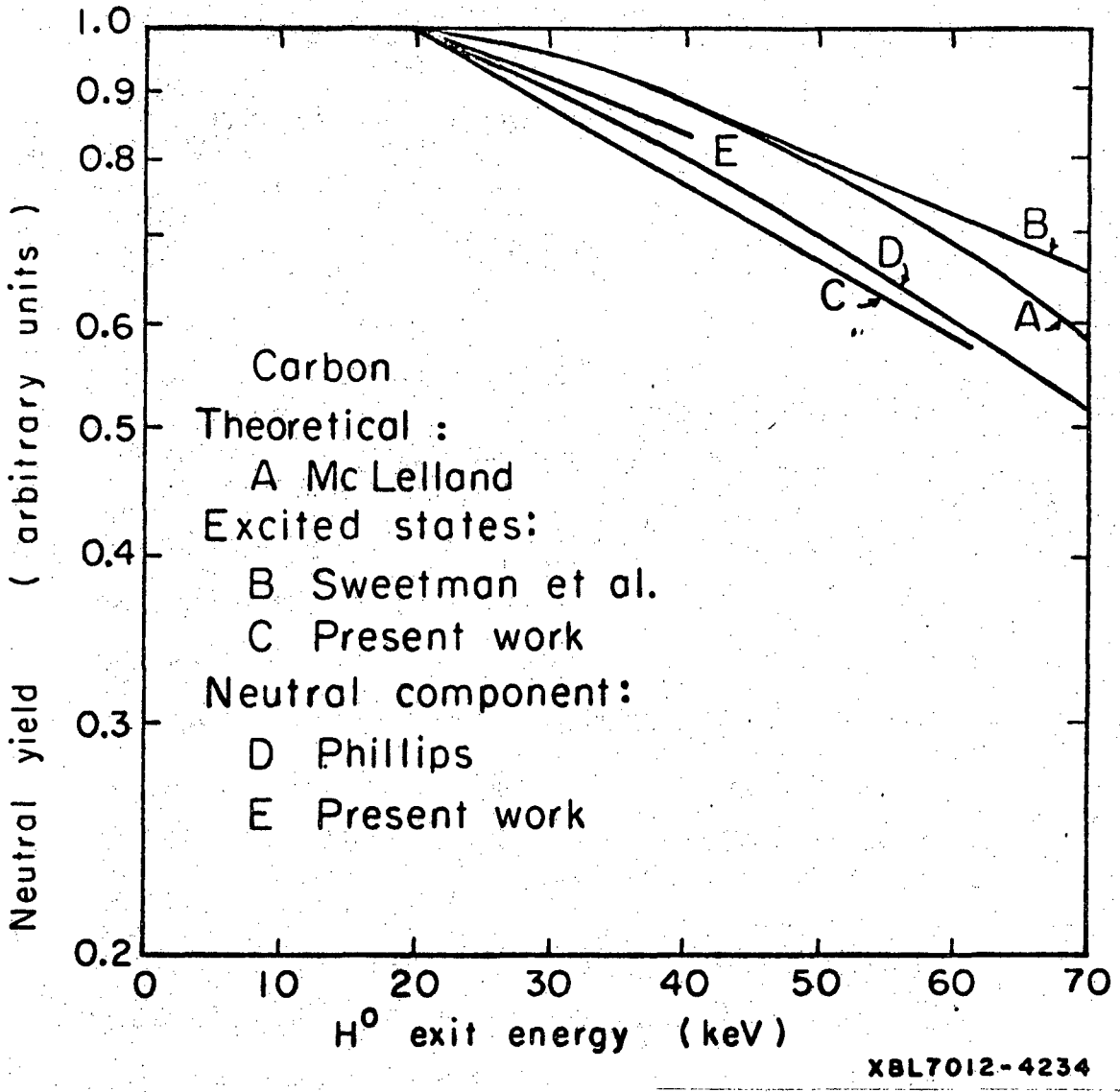

Fig. 14. A comparison of the relative energy dependence of theoretical and experimental excited state yields and neutral beam fractions. Theoretical results (Ref. 8) are for graphite, experimental results are for dirty surfaces. As can be seen in Fig. 10, the energy dependence of the excited state yield for clean and "dirty" carbon is the same in this energy range. Deuterium results of this experiment are plotted at half the deuteron energy. Theoretical: A, Ref. 8. Excited state yields: B, Ref. 10; C, present work. Neutral beam fractions: D, Ref. 9; E, present work.

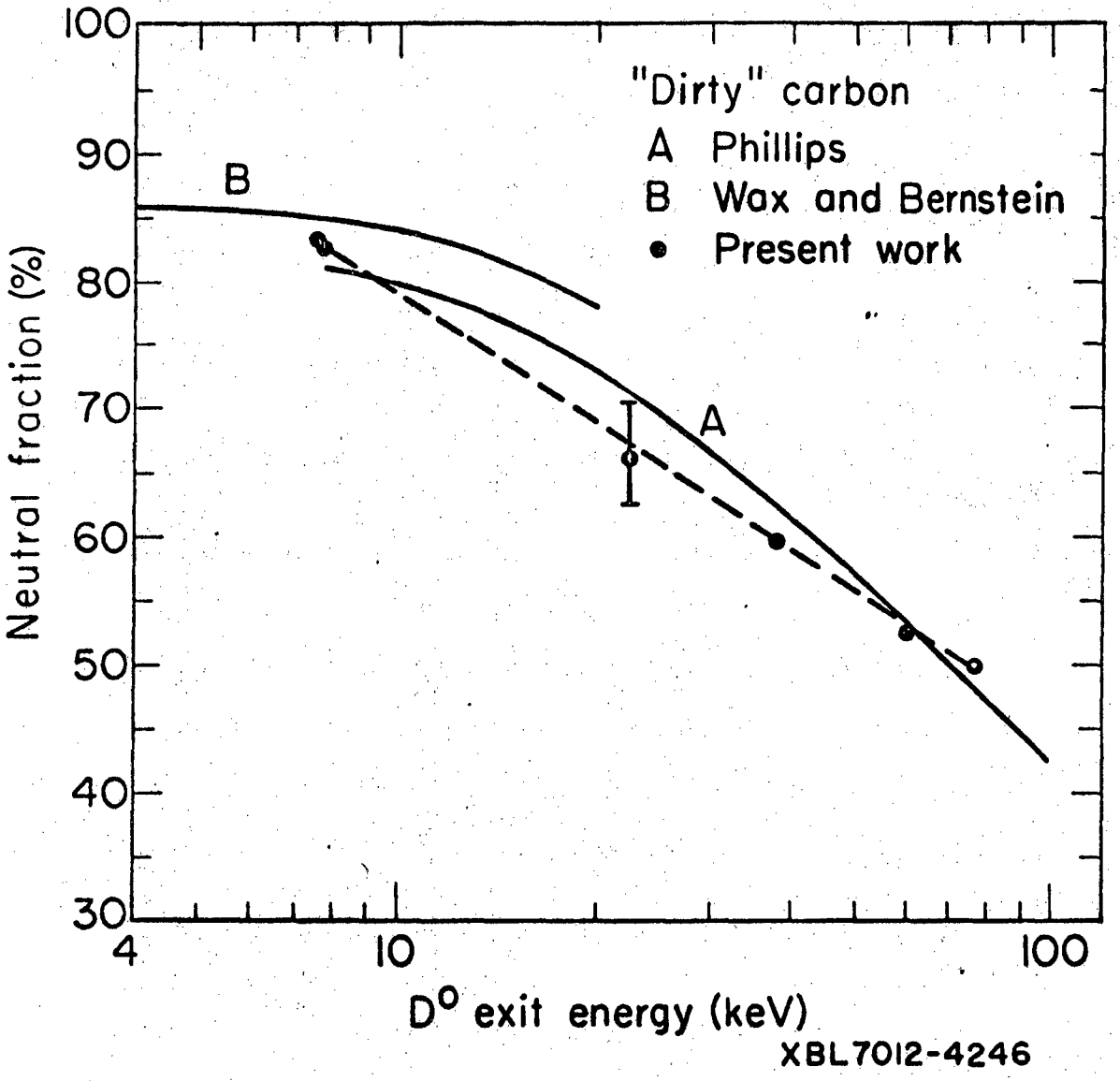

Fig. 15. Neutral fraction from a "dirty" carbon foil: A, Ref. 9; B, Ref. 20; •, present work. The H atom results of Refs. 9 and 20 have been plotted at twice the H energy. The estimated random uncertainty is shown at a representative point. The dashed line is to guide the eye and has no other significance.

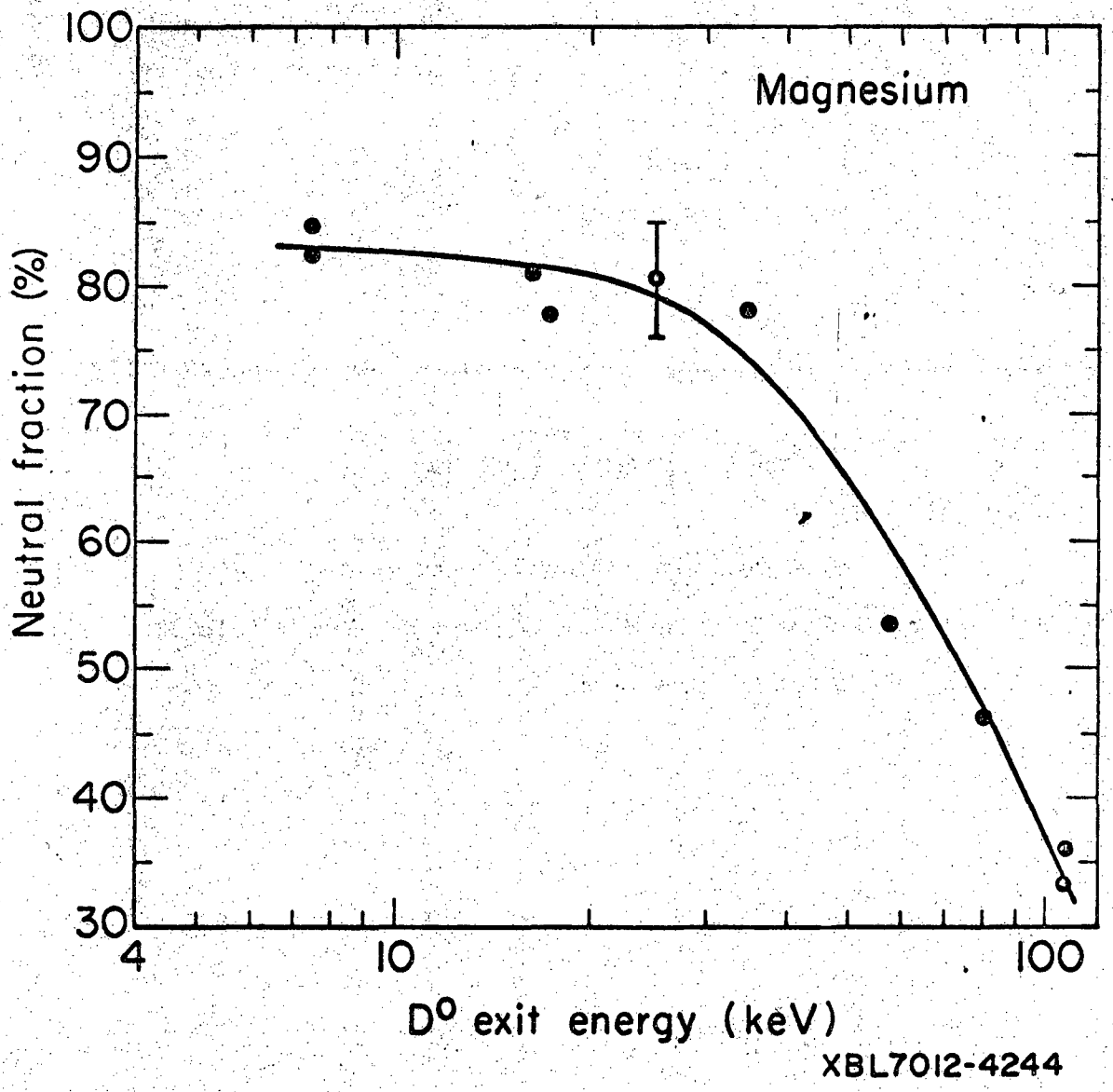

Fig. 16. Neutral fraction from a magnesium-coated foil. The estimated random uncertainty is shown at a representative point. The line has been drawn to guide the eye and has no other significance.

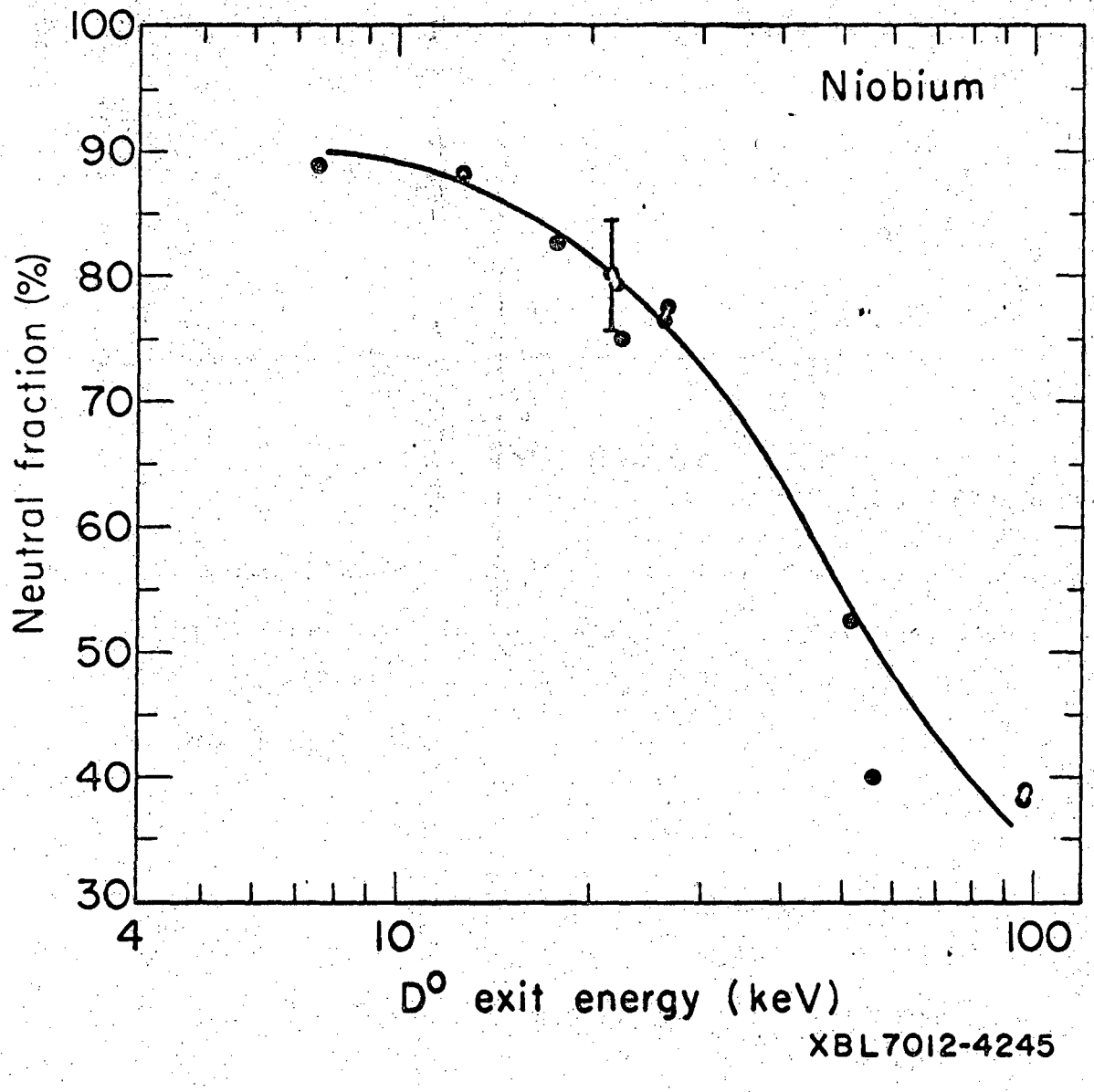

Fig. 17. Neutral fraction from a niobium-coated foil. The estimated random uncertainty is shown at a representative point. The line has been drawn to guide the eye and has no other significance.

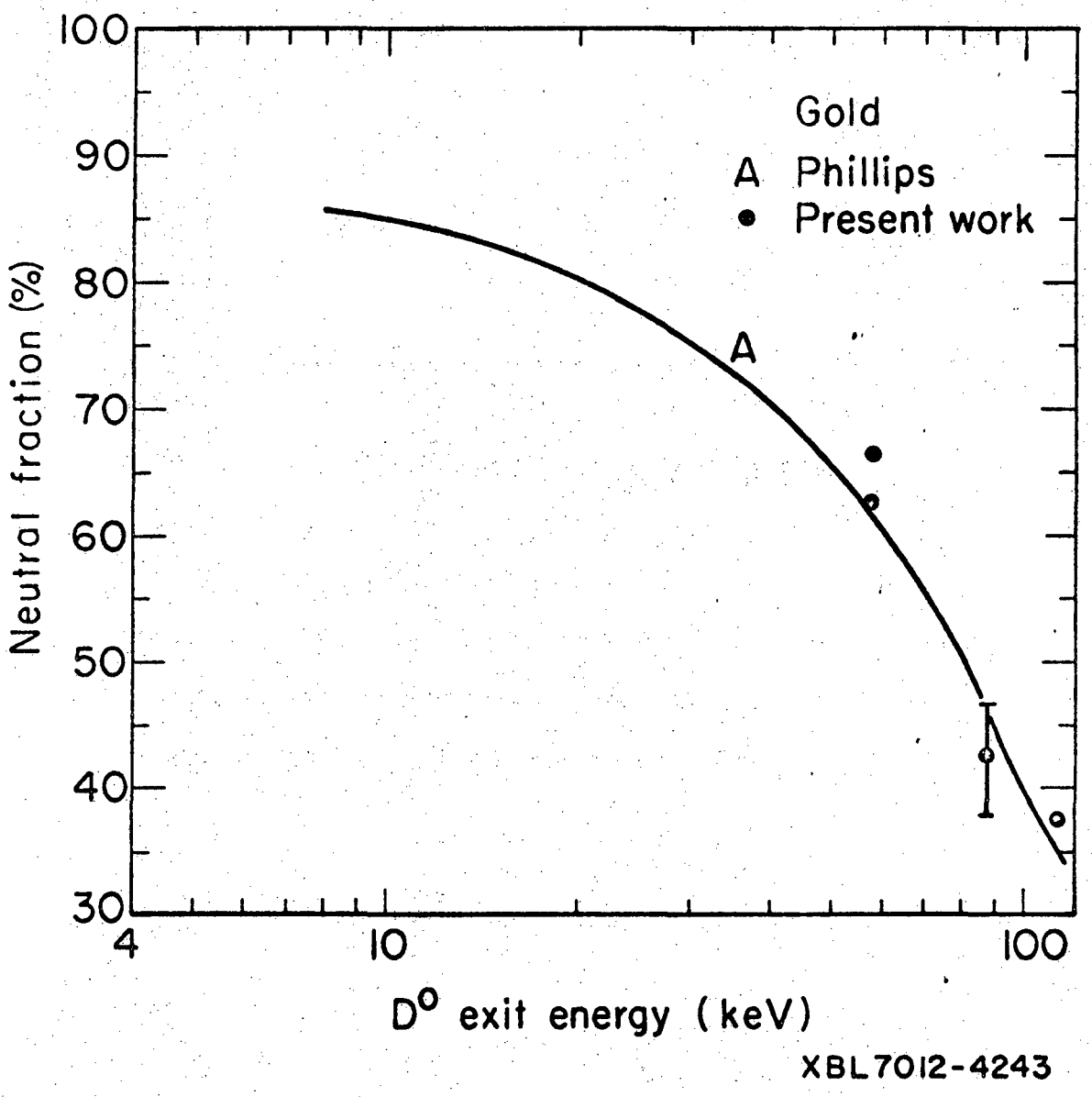

Fig. 18. Neutral fraction from a gold-coated foil: A, Ref. 9; •, present work. The H atom results of Ref. 9 have been plotted at twice the H energy. The estimated random uncertainty is shown at a representative point.

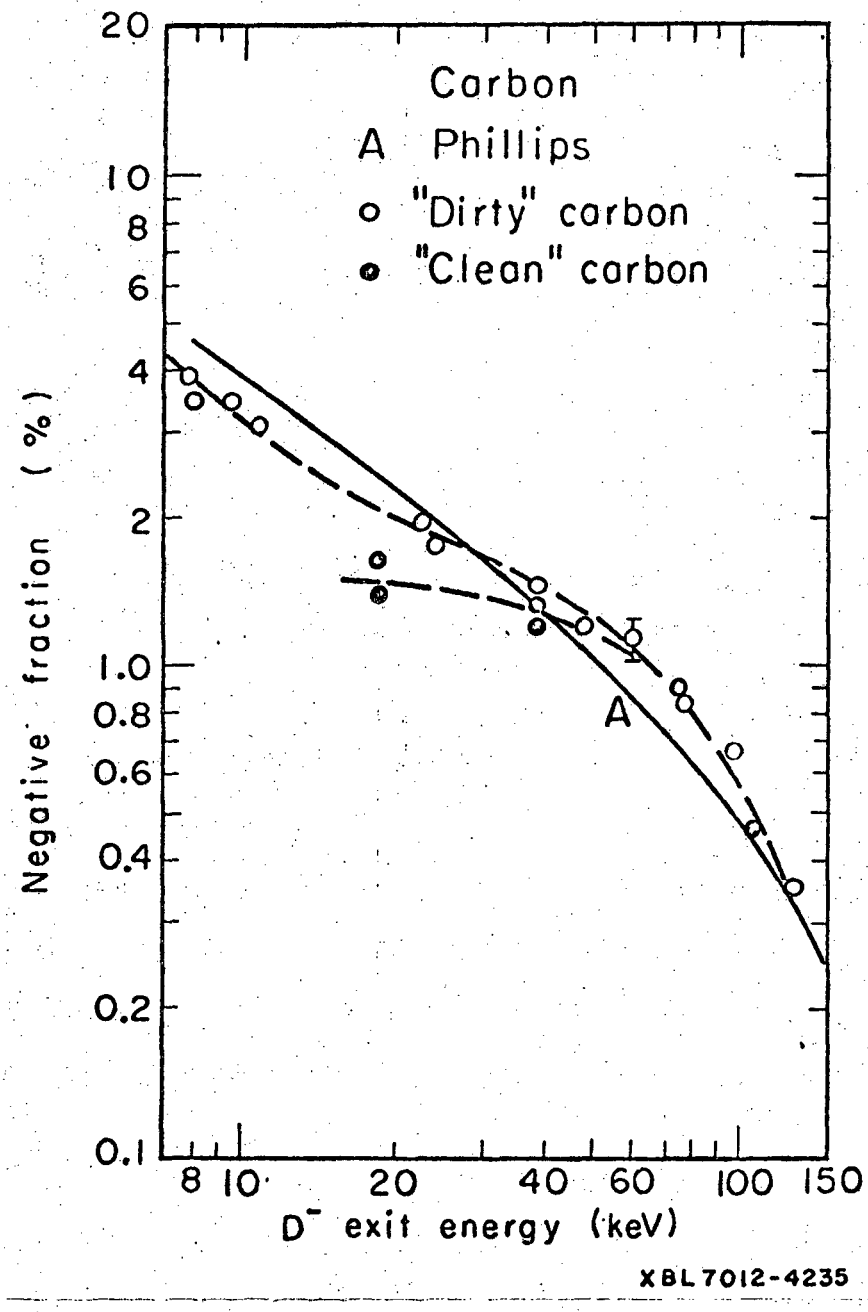

Fig. 19. Negative fraction from a carbon foil: A, Ref. 9 (for dirty surfaces); ●, "dirty" carbon; o, clean carbon. The estimated random uncertainty is shown at a representative point. The H^- data of Ref. 9 has been plotted at twice the H^- energy. The dashed lines have been drawn to guide the eye and have no other significance.

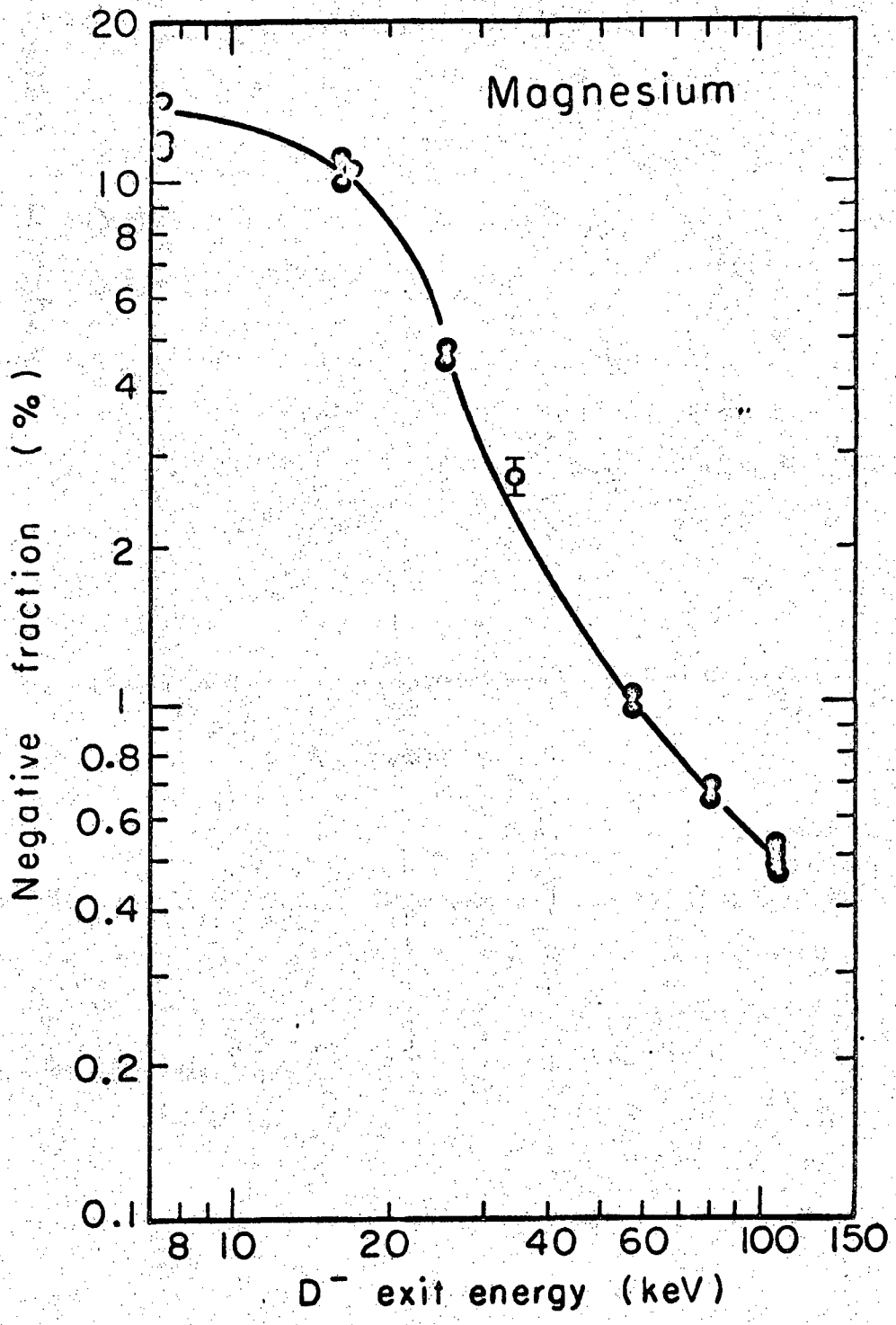

XBL7012-4236

Fig. 20. Negative fraction from a magnesium-coated foil. The estimated random uncertainty is shown at a representative point. The line has been drawn to guide the eye and has no other significance.

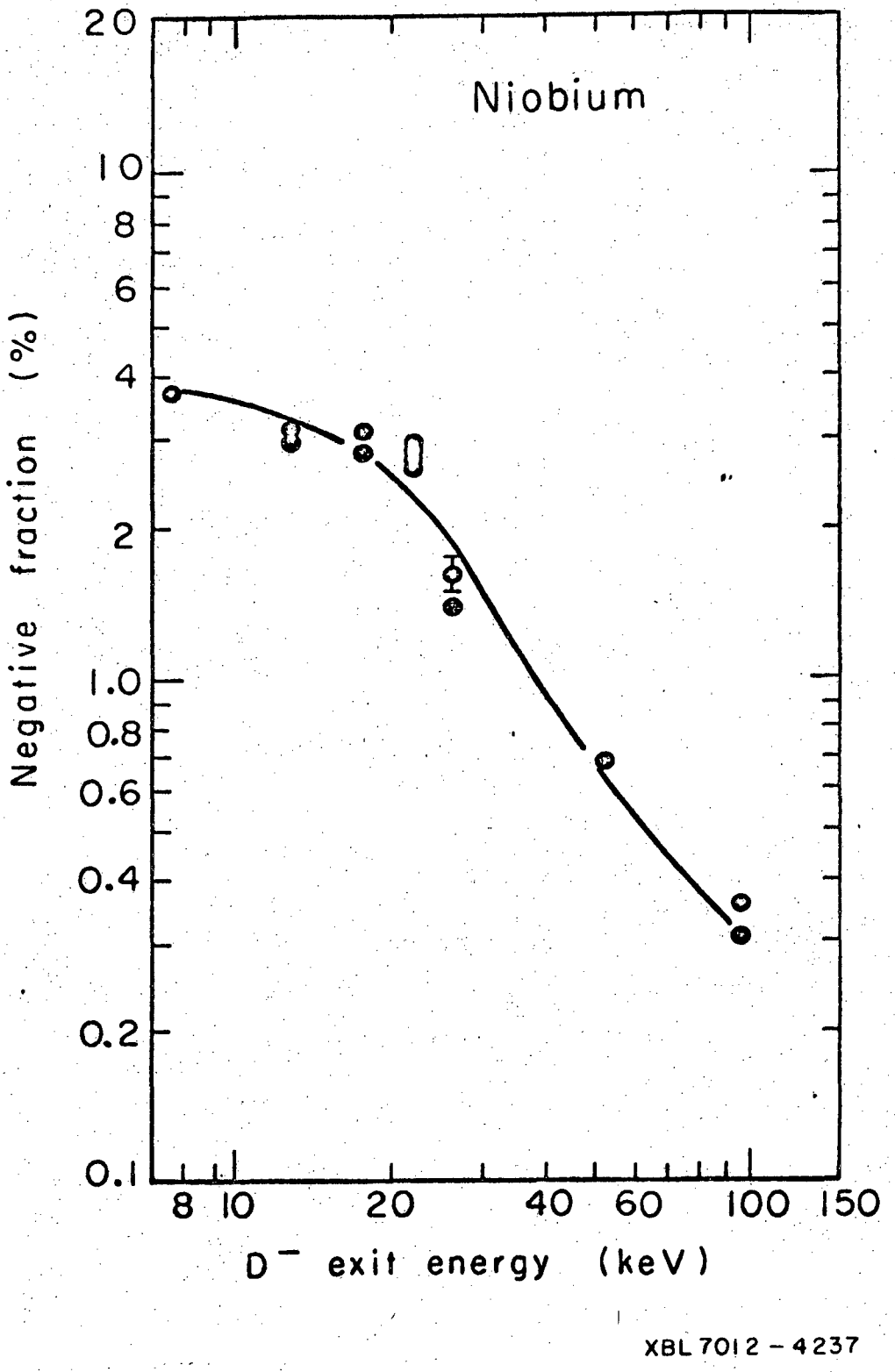

Fig. 21. Negative fraction from a niobium-coated foil. The estimated random uncertainty is shown at a representative point. The line has been drawn to guide the eye and has no other significance.

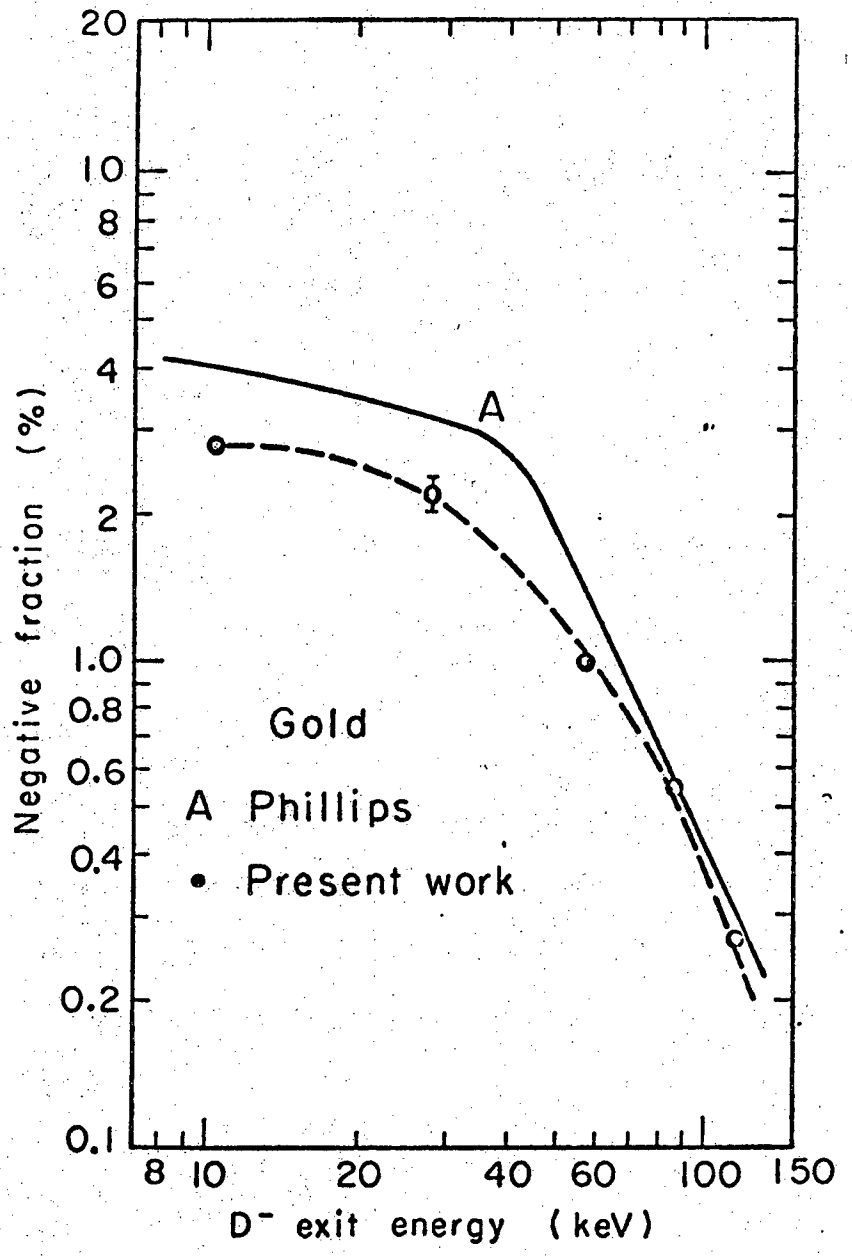

Fig. 22. Negative fraction from a gold-coated foil: A, Ref. 9; •, this experiment. The estimated random uncertainty is shown at a representative point. The H^- data of Ref. 9 has been plotted at twice the H^- energy. The dashed line has been drawn to guide the eye and has no other significance.

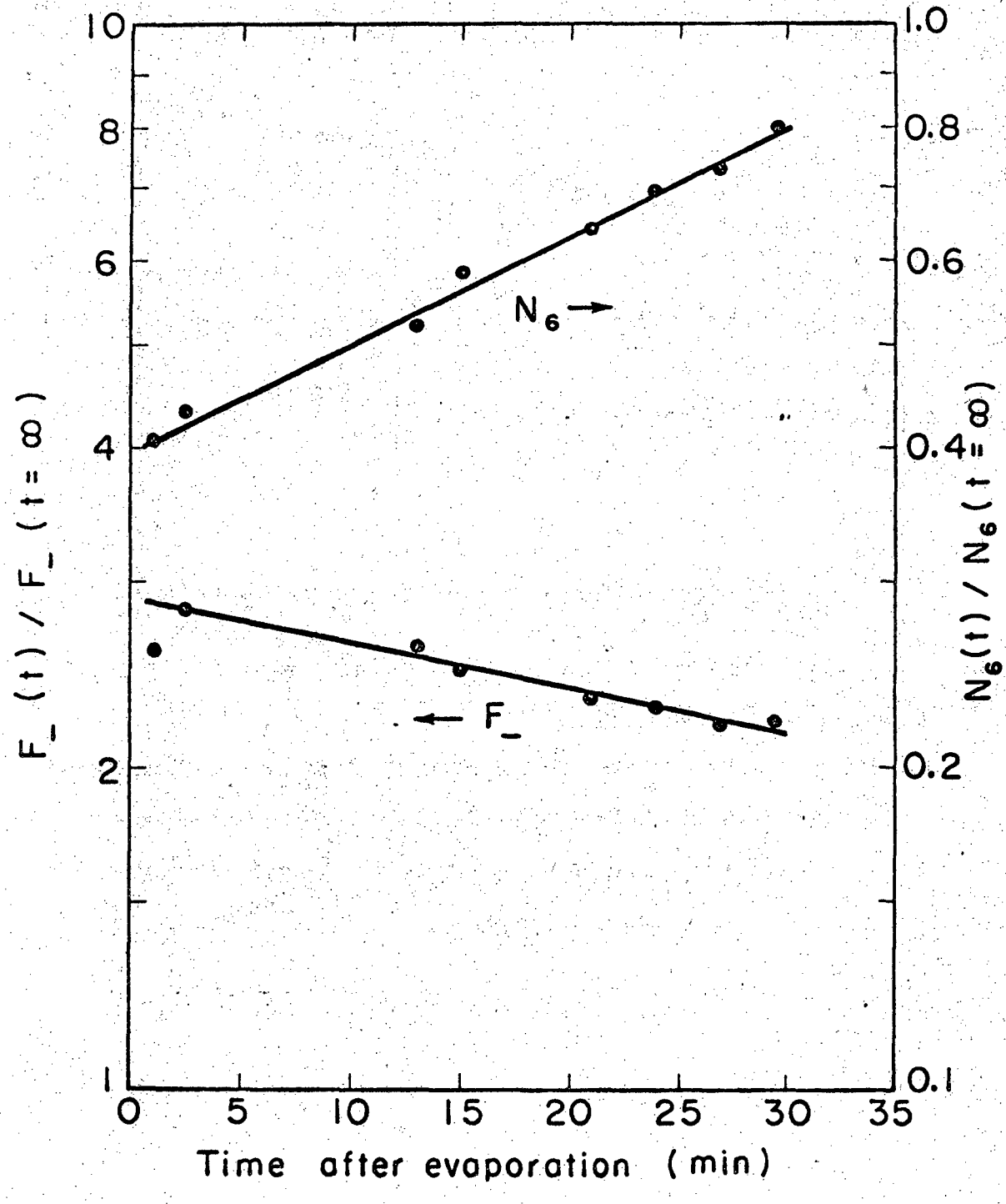

XBL7012-4230

Fig. 23. The time variation of the negative and excited beam components after evaporation. Presumably this is due to contamination of the surface by the background gas. $P = 1 \times 10^{-8}$ torr. Exit energy = 8.2 keV D^+.

This, coupled with the relatively high pressure, made the foil dirtying more noticeable than it was with the other materials and at other energies. A measurement was made of the polarization of the 4101 Å line for 60 and 25 keV D^+. It was found to be polarized in the direction parallel to the beam by 2 to 4 percent.

B. Foil Burnup

Figure 24 shows the results of the foil burning experiments. The average beam intensity for these runs was 0.1 mA/cm^2 though it varied from 0.03 to 0.3 mA/cm^2.

At incident energies of below 45 keV the beam drilled neat round holes in the foils and the break was sharp and sudden. At higher energies several attempts yielded only mixed results. On most attempts, the foil would tear at some point out of the beam line and slowly crinkle and rip, all the while exposing fresh pieces of foil to the beam. One foil was still intercepting the beam after receiving a dose of 3 coulombs/cm^2. Another foil tore in such a way as to remove itself from the beamline quickly; this is the point shown at 80 keV. In an attempt to overcome this effect, the foils were mounted on a tungsten wire mesh of 60 lines/in. and 1.5 mil wire (82.8% transparent). The beam illuminated approximately ten squares in the mesh. With these mesh mounted foils, two effects were noted. First, at 80 keV the foil broke after about 0.5 coulombs/cm^2 or half of the non-mesh value. In addition, the separate holes of the mesh would burn through in rapid succession at high energies and more slowly at low energies (i.e., the variance about the mean mesh hole life was small at high energies and large at low energies).

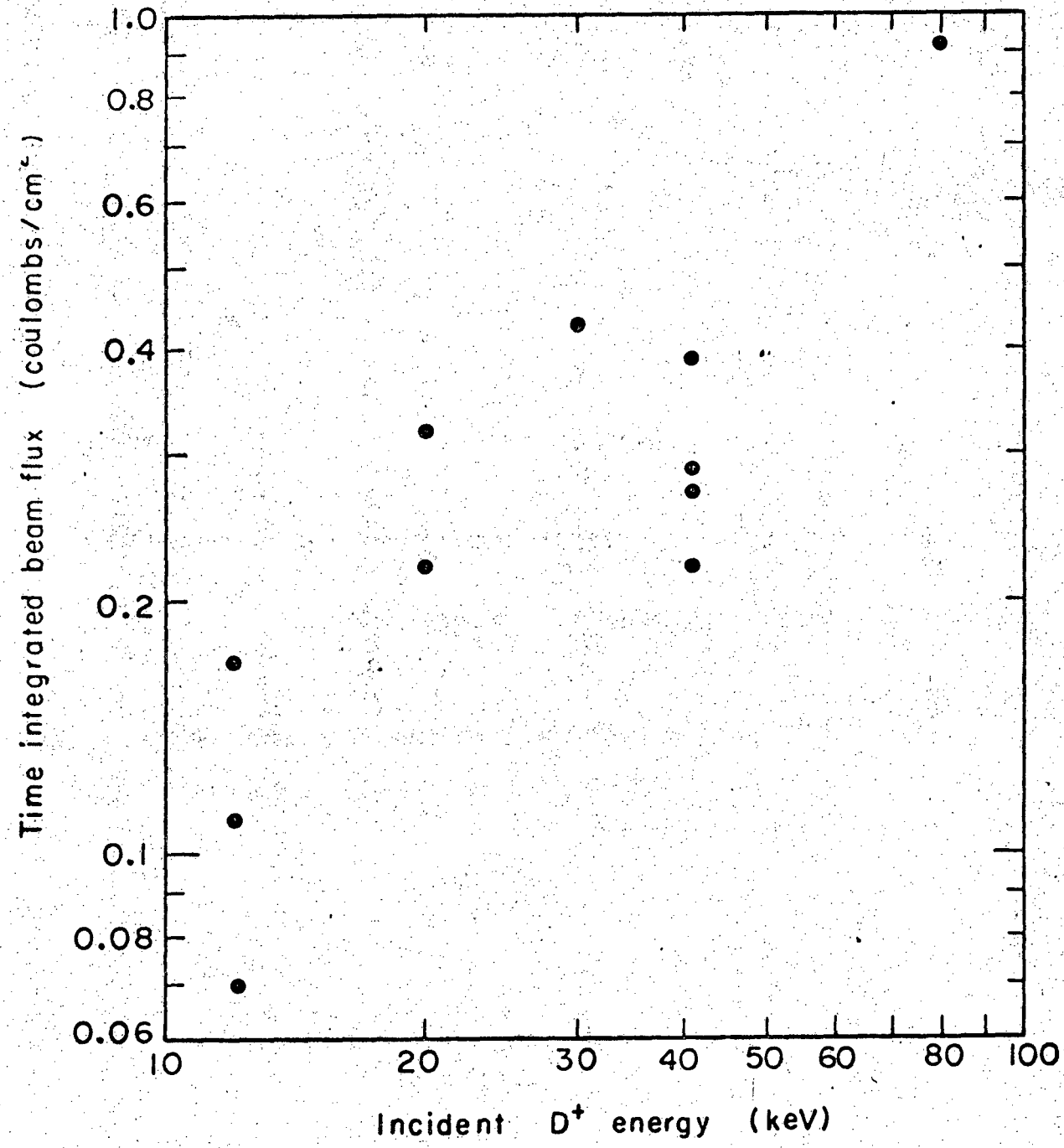

XBL7012-4257

Fig. 24. Time integrated beam flux (coulombs/cm^2) at which 5 μg/cm^2 carbon foils are destroyed vs incident deuteron energy.

Other data available on foil lifetimes are the works of Hunt et al.,[21] Sawyer,[22] Snouse,[23] and Sweetman et al.[10] Hunt's foils were mounted on an 80% transmission, 100 lines/in. tungsten photoetched grid. Table I shows a comparison of that experiment and my experiments with meshes.

Sawyer used self supporting aluminum and silicon monoxide foils. He found that aluminum would tend to oxidize in the beam, due to residual gas in the system, and hence become thicker. The silicon monoxide foils would only oxidize slightly and then remain stable in thickness. He reported that an 8-$\mu g/cm^2$ SiO foil backed with approximately 12 $\mu g/cm^2$ of amorphous carbon could survive irradiations of 0.01 mA/cm^2 for several hours without visible damage.

Snouse used self supporting aluminum oxide foils that were purposely attached loosely to the holder. As a result the foil would not rip as it crinkled in the beam. With a 50-$\mu A/cm^2$, 50-keV H^+ beam he ran a total of 0.8 C through a foil and estimated that it could withstand up to 10 C without breaking. He claims, in fact, that at such low beam levels, the buildup of contaminants on the foil surface would be faster than the loss due to sputtering and the foils might last forever.

Sweetman et al. used 5 to 10-$\mu g/cm^2$ carbon foils and reported a lifetime of about 0.1 C at 40-keV H^+ with currents of up to 8 mA/cm^2.

One possible explanation of foil burnup is sputtering, both forward and backward (see Appendix F). Assuming a 5 μg carbon foil with 20-keV D^+ incident, the total sputtering yield is approximately ~~0.025~~ 0.060 atoms/ion. An irradiation of 0.19 coulomb/cm^2 will have sputtered

Table I. Foil lifetimes (from Ref. 21).

	Thickness Å	Incident energy (keV)	Incident ion	Current density ($\mu A/cm^2$)	Incident charge ($coulomb/cm^2$)
Carbon	340	20	H_2	45	0.073
	380	21	H_3	44	0.064
Carbon on Rhenium	300(C) + 200(Re)	21	H_3	49	0.42
	300(C) + 400(Re)	27	H_3	25	0.2
	590(C) + 130(Re)	28	H_3	72	0.13
Vanadium	500	20	H_3	48	0.017
Gold	500	20	H_3	49	0.25
Titanium	500	20	H_3	52	0.56
Rhenium	180	20	H_2	44	0.17
	370	20	H_2	38	0.14
	500	20	H_2	47	0.05
	170	18,25,30	H_3	24,58,82	1.4
	170	20,25	H_3	29,56	0.85
	500	24	H_3	56	1.3
	500	20	H_3	54	2.1
Carbon (this experiment)	250	30	D	140	0.3
	250	50	D	360	0.6
	250	80	D	250	0.5

7.2×10^{16} particles, which is 1.4 $\mu g/cm^2$ or about 30% of the foil's mass. Thus sputtering is an important factor in foil failure.

Another factor in foil burnup is evaporation (see Appendix G) due to the heating effect of the beam. Assume again a 20-keV D^+ beam incident of a 5 μg carbon foil. The stopping power of the foil is 0.45 $keV/\mu g/cm^2$ (stopping powers are taken from Appendix D) so the beam loses about 2.25 keV in the foil. If we have a 152 mA/cm^2 beam and assume black-body radiation as the only heat loss mechanism, the foil temperature in the beam will be 2439°K. At this temperature the vapor pressure of carbon is about 2.1×10^{-7} atm,[24] which gives an evaporation rate of 6.2×10^{16} particles/cm^2/sec. At this rate, 30% of the foil will evaporate in approximately 1 sec. Therefore, with a beam flux of 152 mA/cm^2 the foil deterioration due to evaporation is approximately equal to that due to sputtering. It can be shown, however, that in carbon evaporation varies as the 10th power of the flux and whereas at high fluxes it would be important, at low fluxes (i.e., the conditions of this experiment) it is unimportant.

V. CONCLUSIONS

Foils have three main advantages over vapors for use as a charge exchange medium for controlled thermonuclear fusion experiments. These are:

1. The excited state yield at low energies from a foil is much greater than from a gas or a vapor. As can be seen from a comparison of Figures 2 and 9, at a proton energy of 10 keV (deuteron energy of 20 keV), the excited state yield from a dirty carbon foil is a factor of three higher than that from an optimum magnesium vapor target which is considered to be one of the best gaseous excitation media.[5] Among those tested, the foil material giving the highest yield at low energies is dirty carbon. This is fortuitous as it eliminates the need for evaporators, high vacuum near the foil, etc.

2. Rather than being a significant source of contaminants, foils can serve as a barrier between good and poor vacuum regions.[22,23,25,26] The only contaminants emanating from a foil are those particles sputtered or evaporated off. This would eliminate the need for strong differential pumping between the source and the plasma chamber.

3. A foil can be placed closer to the plasma than a gaseous target, which may give geometrical advantages.

However, there are three disadvantages to foils:

1. Scattering: a 5 μg carbon foil at 20 keV will scatter deuterons with an rms angle of about 2.5 degrees (see Appendix E). This is greater than the scattering from a gas neutralizer but comparable to the divergence of present day ion sources.

2. Forward sputtering: a 5 μg carbon foil at 20 keV has a

forward sputtering yield of 1.3% (see Appendix F). The sputtered atoms have a mean energy of a few eV, but the charge and angular distributions are presently unknown.[27] In some devices it might be necessary to prevent these cold high Z atoms from contaminating the plasma.

3. Foil burnup: the limited life of the foils will limit their applicability, depending of course on the current they will have to transmit. Concerning the Phoenix experiment, Sweetman[10] estimated the minimum neutral beam requirement to be 0.2 coulomb equivalent. This is at the limit of the current capacity of a single foil and would imply the need for splitting the beam into several portions and passing it through several foils. Each of these foils would have to be replaced at each startup.

Topics for further experimental research would include the angular dependance and charge states of sputtered particles emitted in the forward direction, the effects of channeling, scattering of deuterons at energies below about 30 keV, better methods of supporting foils, and investigation of other materials.

Topics for theoretical research would include a complete theory of the excited state yields in metals, a theory describing the yield in semi-metals at low energies, or a general theory applicable to all materials.

ACKNOWLEDGMENTS

I wish to thank Dr. Robert V. Pyle for his encouragement and guidance throughout the course of this work. I am grateful to Dr. Klaus Berkner and to J. Warren Stearns fro their assistance during long days and nights of data taking. My thanks also goes to Vincent J. Honey who designed and constructed much of the electronic equipment and to the mechanical shops of Harlan Hughes and Louis Biagi who constructed the vacuum chambers. Margret Thomas typed the many drafts of this report for which I am also grateful.

This research was performed under the auspices of the U.S. Atomic Energy Commission and, in part, under the tenure of a Nuclear Science and Engineering fellowship granted by the A.E.C.

APPENDICES

A. Theory Relevant to the Experimental Calculations

1. Optical Method

There are two basic sets of measurements: in the first, the de-excitation counts per incident particle are measured, and the second is a system calibration using nitrogen gas.

The counts observed by the photomultiplier during the nitrogen calibration is given by the following equation:

(Photomultiplier counts) = (system efficiency) x (particle flux)
x (interaction cross section) x (gas density)
x (interaction length)

In our system, the interaction length was 1.5 cm. Therefore the above equation becomes (at room temperature):

$$\text{Counts/particle} = 4.83 \times 10^{16}\ \epsilon\sigma p$$

where ϵ is the optical efficiency of the system

σ is the interaction cross section in cm^2

p is the gas pressure in torr

But (counts/particle)/p is just the slope of a straight line fit to a plot of counts/particle vs pressure. Therefore,

$$\epsilon = \frac{\text{slope}}{4.83 \times 10^{16}\ \sigma}$$

The interaction cross section is a combination of that for deuteron impact and that for deuterium atom impact. These cross sections[28-37] are shown in Fig. 25 and Fig. 26. Thomas et al.[32] have shown that deuterium impact cross sections are the same as that of hydrogen atoms with half the deuterium energy.

There remains one more factor to calculate in order to obtain

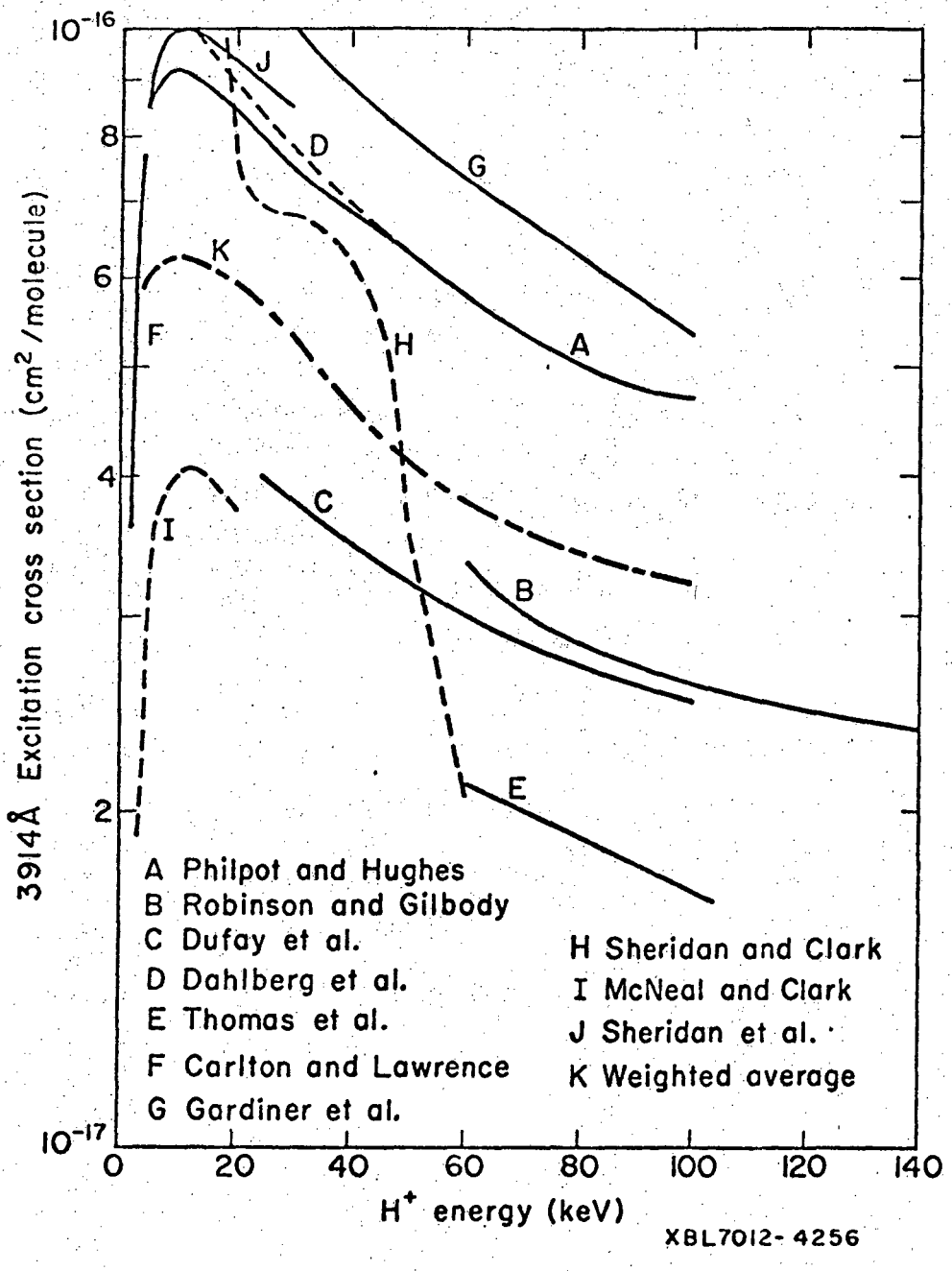

Fig. 25. Available data on the excitation of the 3914 Å band in N_2^+ by H^+ impact. Solid lines indicate absolute measurements, dashed lines indicate relative measurements. A, Ref. 28; B, Ref. 29; C, Ref. 30; D, Ref. 31; E, Ref. 32; F, Ref. 33; G, Ref. 34; H, Ref. 35; I, Ref. 36; J, Ref. 37; K, weighted average curve. For a description of the averaging techniques see Appendix H.

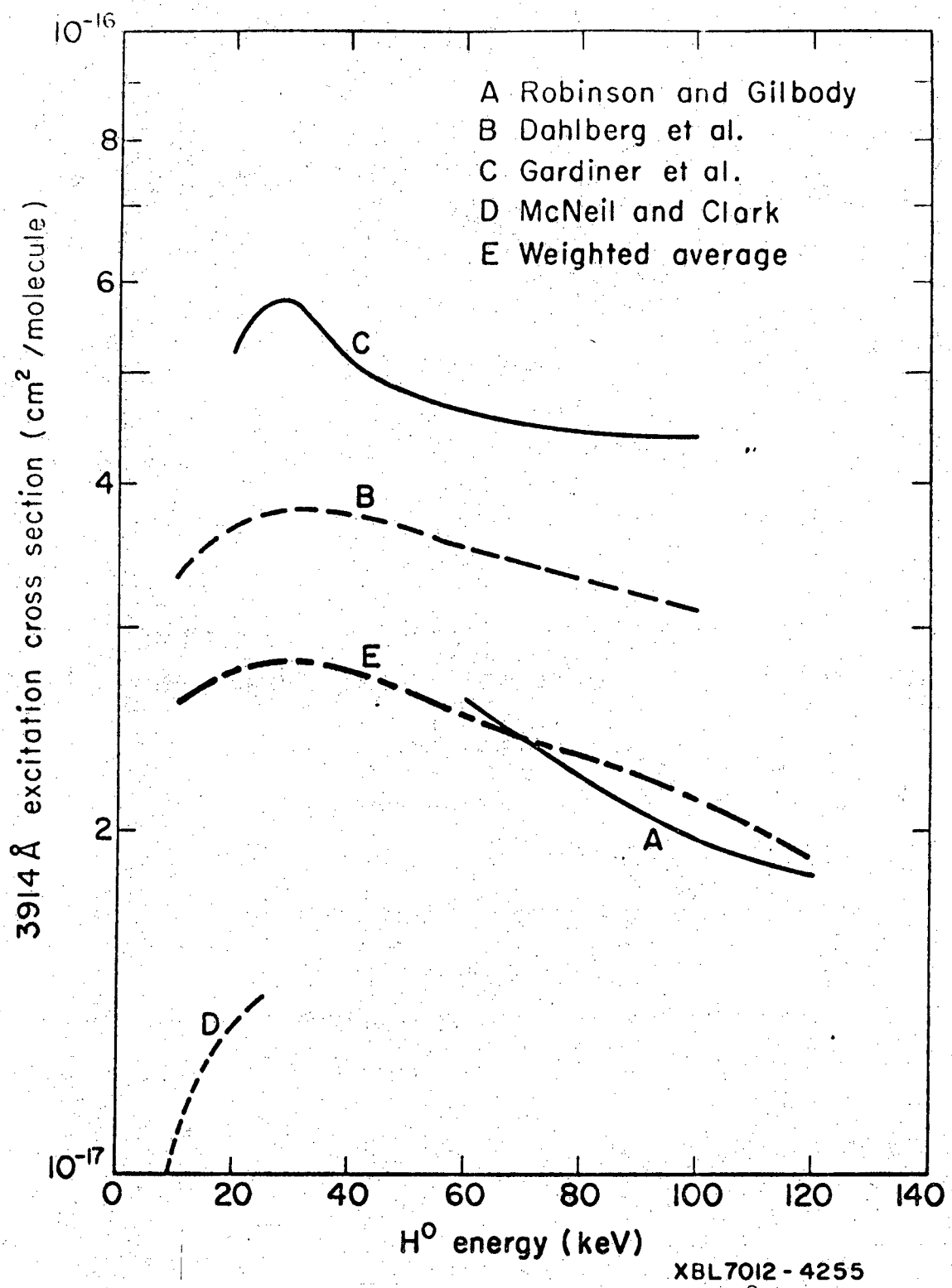

Fig. 26. Available data on the excitation of the 3914 Å band in N_2^+ by H^0 impact. Solid lines indicate absolute measurements; dashed lines indicate relative measurements. A, Ref. 29; B, Ref. 31; C, Ref. 34; D, weighted average curve. For a description of the averaging technique used, see Appendix H.

the optical efficiency of the system. The excited atoms in the beam are constantly decaying, some will decay before the observation region and some after so we have to compensate for the fact that we are not observing the decay of all the excited particles.

The 4101 Å line is emitted by the following transitions:

$6S \rightarrow 2p$

$6p \rightarrow 2S$

$6d \rightarrow 2p$

We can assume[6] that cascading into these states is unimportant.

The probability that an excited atom will de-excite, emitting 4101 Å radiation, in the observation region is equal to the product of probability[38] that the atom will not decay by any means before the observation region with the probability that it will decay through one of the above transitions in the observation region. The numbers appropriate to the calculation are shown in Table II. Using them, one calculates[6] that

$$N_6^0 = N(D_\delta) \times 10^3 \times \left[\frac{46.8}{\sqrt{E}} - \frac{23.7}{E}\right]^{-1}$$

where

N_6^0 = fraction of total beam in state n = 6 at the exit of the foil

$N(D_\delta)$ = observed fraction of total beam in state n = 6

E = deuteron energy in keV.

A plot of the coefficient of $N(D_\delta)$ is given in Fig. 27. This coefficient can be called a decay correction as it corrects the observed excited state yield for decay de-excitations occurring outside the observation field or resulting from other transitions.

Table II. Data required to calculate decay correction.

State	De-excitation rate by any transition[38]	Transition	Mean life (sec)[38]
6S	1.87×10^{6}/sec	6S → 2p	1.3×10^{-6}
6p	2.45×10^{7}	6p → 2S	3.5×10^{-7}
6d	8.39×10^{6}	6d → 2p	2.0×10^{-7}

Distance from foil to observation region = 1.275 cm

Length of observation region = 1.5 cm

Assume states are statistically populated (in the ratio of $2\ell + 1$)

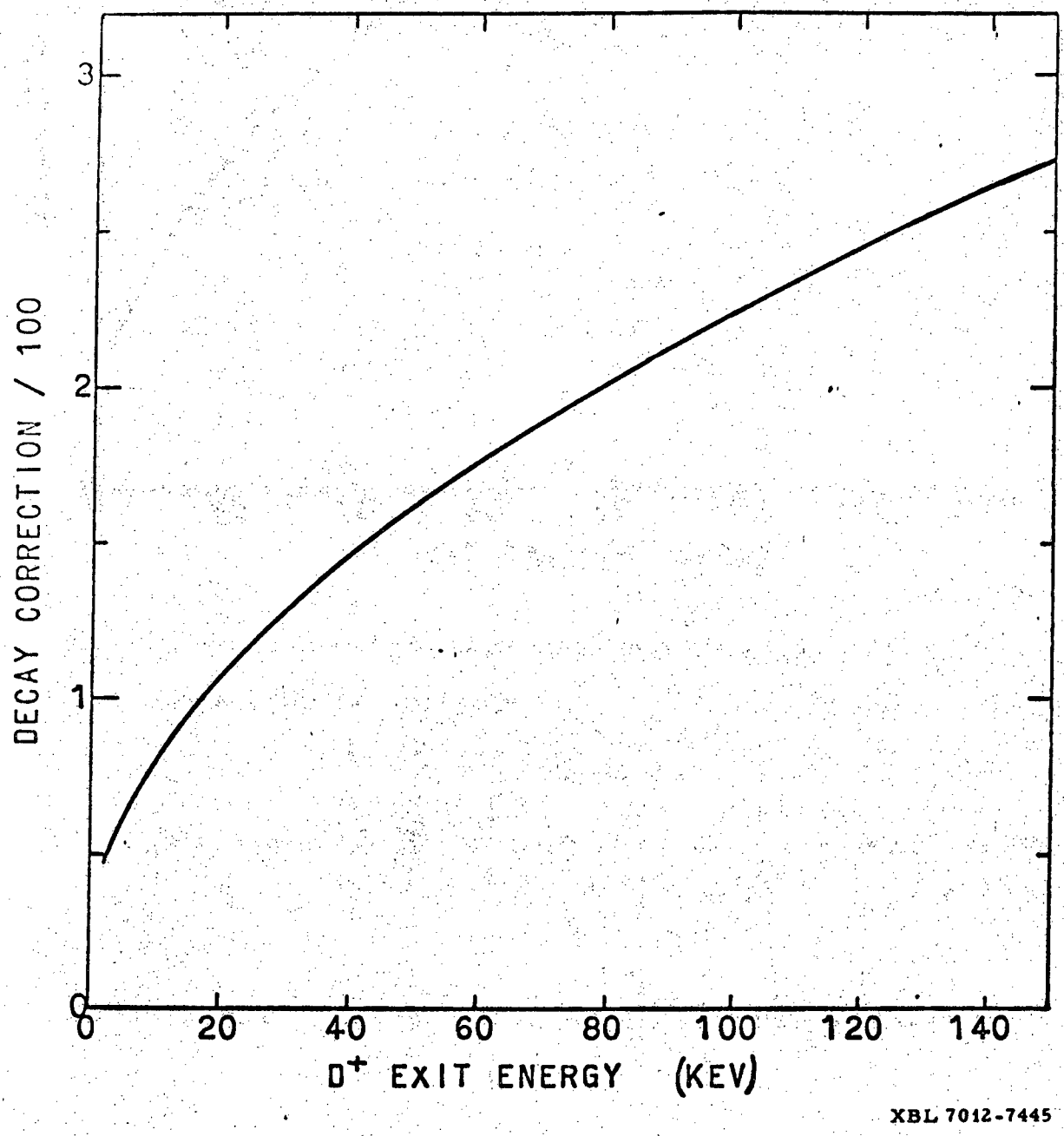

Fig. 27. Decay correction vs deuteron exit energy for our experimental configuration (see Appendix A).

The total excited state yield is therefore given by

$$N_6^0 = \frac{\text{(counts/particle) x (decay correction)}}{\epsilon}$$

2. High Voltage Gap Method

As can be seen above, data reduction in the optical method is a long involved process which took almost as long as the data collection itself. In the high voltage gap method, however, data reduction is considerably simplified, allowing results to be calculated almost immediately.

Consider, for example, a Bohr atom in state n. The binding energy of the electron is given by

$$W_n \sim \frac{1}{n^2}$$

and its radius is given by

$$r_n \sim n^2$$

If one imposes an external electric field of such a magnitude that an electron gains W_n eV while revolving from one side of the nucleus to the other, i.e.

$$E_n = \frac{W_n}{2r_n} = \frac{b}{n^4}$$

(where b is a constant), the atom will be ionized. This is the principle of the high voltage gap method. For the Bohr atom we find

$$b = \frac{13.58 \text{ eV}}{2 \times 0.5292 \text{ Å}} = 1.28 \times 10^6 \text{ kV/cm}$$

The Bohr atom approach, of course, ignores tunneling. A more accurate calculation, assuming a statistical distribution over substates and using the data of Riviere[39] gives

$$E_n = \frac{4.29 \times 10^5}{n^{3.82}} \text{ kV/cm}$$

for transition times on the order of 10^{-10} to 10^{-9} seconds. As will soon be shown, the results will not be far off if we do, however, assume that $E_n = b/n^4$.

To analyze the gap data, what is needed is a relationship between the measured current and the voltage across the gap. The current results from the ionization of the excited states, so first we will derive the relationship between the current and the state. We will assume (according to the theories of Trubnikov and Yavlinskii[7] and McLelland[8]) that the relative populations of the various n states are proportional to n^{-3}. Therefore we write

$$\frac{dI}{dn} = -\frac{a}{n^3}$$

where a is a constant. Integrating, we get

$$I = \frac{a}{2} \cdot \frac{1}{n^2}$$

Since $1/n^2 = \sqrt{E/b}$, we have $I = \left[a/(2\sqrt{b})\right]\sqrt{E}$, where I = fraction of neutral beam which has been ionized in gap and E = electric field in gap (kV/cm).

The data of Riviere then gives $b = 6.8 \times 10^5$. Therefore

$$I = 6.1 \times 10^{-4} a \sqrt{E}.$$

Had we not made the simplifying assumption that $E_n \sim n^{-4}$, the equation would have been

$$I = 5.62 \times 10^{-4} \, aE^{0.524}.$$

At 25 keV the simplified equation differs from the more accurate one by only 1.5%.

Neither I nor E are measured quantities so let us define the

following:

V = the voltage applied to the gap (kV)

I_+^0 = the current of ionized particles produced by the gap

I^0 = the equivalent neutral current passing through the gap

I^+, I^- = the charge currents measured at their respective Faraday cups

I_{TOT}^o = the charge current measured in the neutral cup with the deflection voltage off

We can now write

$$E = cV \qquad \text{where } c = \text{constant of geometry}$$

$$I = \frac{I_+^0}{I^0}$$

and therefore

$$\frac{I_+^0}{\sqrt{V}} = 6.1 \times 10^{-4}\, a I^0 \sqrt{c}$$

This is m, the slope of the curve plotted by our X-Y plotter.

Therefore

$$a = \frac{m}{6.1 \times 10^{-4}\, I^0 \sqrt{c}}$$

I^0 is obviously given by

$$I^0 = I^+ \frac{F^o}{F^+} T$$

where F^o = neutral fraction of beam

F^+ = positive fraction of beam

T = transmission of grid assembly

F^o, as in the optical method, is measured by taking the ratio of the neutral detector readings with the deflection voltage on and off. This is the only measurement requiring a pulsed beam, all other measurements in the gap method can be made with a D.C. beam.

The transmission is given by:

$$T = \frac{I^o_{TOT}}{I^+ - I^-}$$

F^+ is not measured directly but is calculated from:

$$F^o + F^+ + F^- = 1$$

$$\frac{F^-}{F^+} = \frac{I^-}{I^+}$$

combining, we get

$$F^+ = \frac{(1-F^o)I^+}{I^+ + I^-}$$

and finally,

$$I^o = \frac{F^o}{1-F^o} \frac{I^+ + I^-}{I^+ - I^-} I^o_{TOT}$$

we also have

$$\frac{N_6^o}{F^o} = \frac{a}{6^3} = \frac{a}{216}$$

and therefore

$$N_6^{\,o} = \frac{m}{0.132\sqrt{c}} \frac{1 - F^o}{I^o_{TOT}} \cdot \frac{I^+ - I^-}{I^+ + I^+}$$

Due to the small dimensions of the high voltage gap grid assembly, it would be difficult to make an accurate direct measurement of c; therefore, it was measured indirectly as follows:

As can be seen in Fig. 28, there is a low voltage break point at which the plot is no longer a straight line. This is due to the ioni-

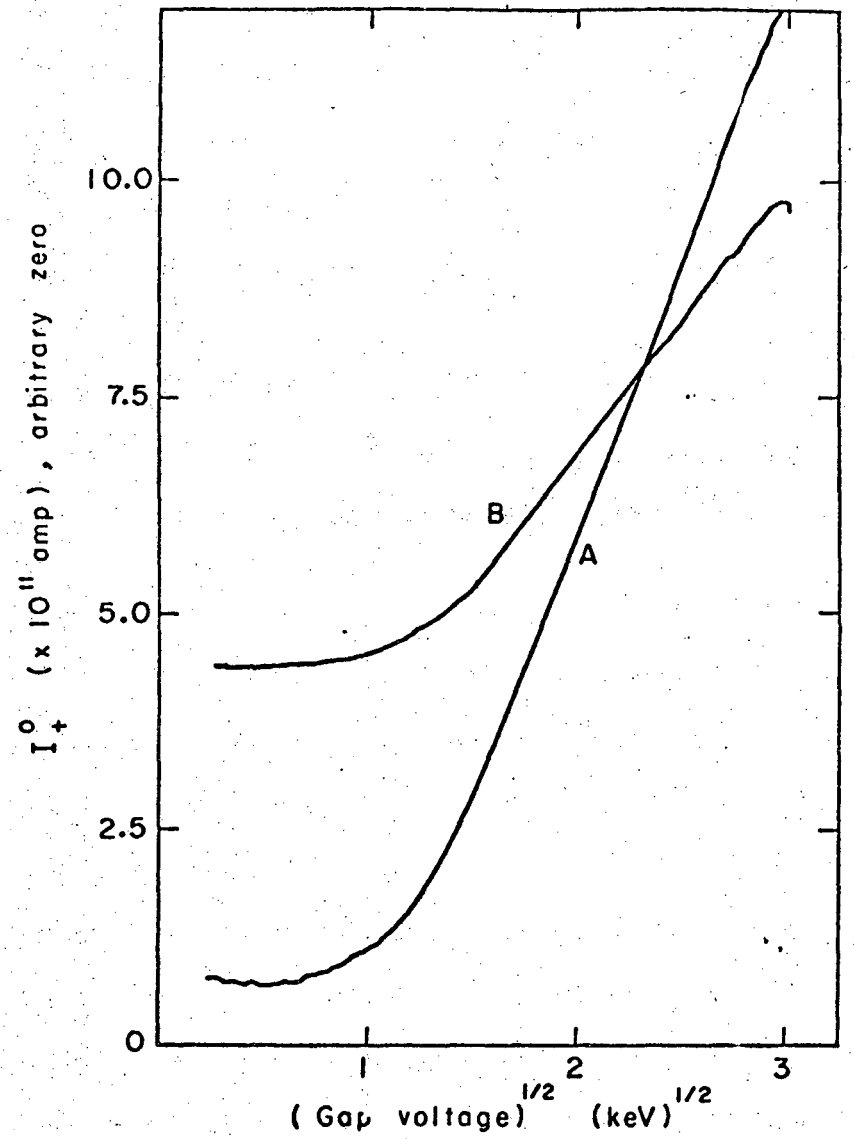

Fig. 28. A typical high-voltage gap measurement made with 71.8-keV deuterons out of a carbon foil. Curve A: 4.7×10^{-8} A beam out of a "dirty" foil. Slope from 1.5 to $3\sqrt{\text{keV}}$ = 6.15×10^{-11} A/$\sqrt{\text{keV}}$. Curve B: 2.25×10^{-8} A beam out of the same foil with a layer of clean carbon deposited on the exit surface. Slope from 1.5 to $3\sqrt{\text{keV}}$ = 3.1×10^{-11} A/$\sqrt{\text{keV}}$. The range from 1.5 to $3\sqrt{\text{keV}}$ corresponds to an electric field of range 7.5 to 30 kV/cm or a range of n from about 18 to 12.

zation of highly excited atoms by the deflection voltage. These atoms are then swept away with the charged beam and do not enter the gap. Figure 29 shows a plot of the break point voltage vs deflection voltage. From the slope of this curve, we see that 1 kV on the gap has the same "ionizing power" as 4.08 kV on the deflection plates. A two dimensional plot of the field between the deflection plates showed that field to be 640 volts/cm per kilovolt of applied voltage. Thus we see that 1 kV on the gap is equivalent to a field of $0.64 \times 4.08 = 2.61$ kV/cm, and c = 2.61. Thus, we have

$$N_6^0 = 4.69\, m \frac{1 - F^0}{I^0_{TOT}} \cdot \frac{I^+ - I^-}{I^+ + I^-} .$$

It should be noticed that there is no decay correction. This is due to the fact that the high voltage gap os sufficiently close to the foil to make the decay correction negligible.

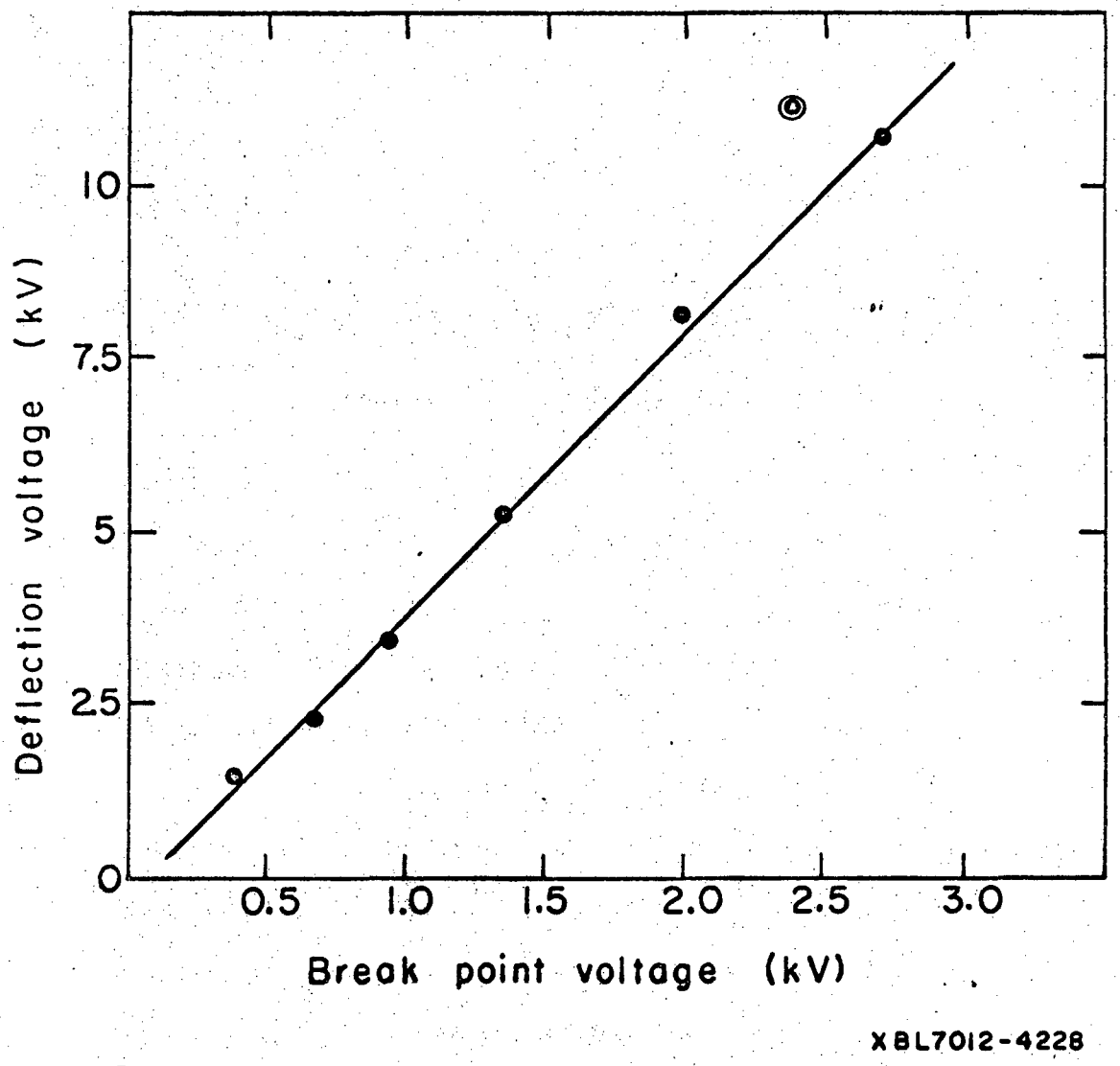

XBL7012-4228

Fig. 29. Deflection voltage vs "breakpoint" voltage. For a given deflection voltage, the breakpoint voltage is the lowest gap voltage which will ionize states which were not ionized in the deflector. The line shown is a least squares fit to the data, ignoring the circled point which is obviously in error. The fact that the line does not go through the origin is probably an indication of a systematic error in the measurement of the breakpoint. At most, this would introduce a 2% error in the excited state yields.

B. Sample Calculations

1. Optical Method

(a) Determine exit energy and foil thickness

Accelerator potential = 60.14 kV

Deflector voltage without foil = 10.94 kV

Deflection voltage with foil = 10.04 kV

$$\text{Energy at exit of foil} = \frac{10.04}{10.94} \times 60.15 = 55.19 \text{ kV}$$

$$\text{Energy loss in foil} = 60.14 - 55.19 = 4.95 \text{ kV}$$

$$\text{Stopping power of foil} = 0.62 \text{ keV}/\mu g/cm^2$$

$$\text{Thickness of foil} = \frac{4.95}{0.62} \approx 8 \ \mu g/cm^2$$

(b) Calibrate integrators on charged particle detectors

With electrometer set on full scale, an integration time of 100 seconds gave an integrator reading of 49.62.

$$\text{Integrator constant} = \frac{100 \text{ sec}}{49.62 \times 1.6 \times 10^{-19} \text{ coulomb/particle}}$$

$$= 1.26 \times 10^{19} \text{ particle/ampere}$$

Note that: Integrator constant x reading x electrometer scale = total particles reaching detector.

(c) Readings with 4101 Å filter and deflection voltage on

Time (beam on)	22.007 sec
Time (beam off)	19.285 sec
Photomultiplier counts (beam on)	47249
Photomultiplier counts (beam off)	61
Neutral detector reading	1.0
Neutral detector scale	2 mV
Positive beam detector reading	12.83
Positive beam detector scale	10×10^{-8} A

(The negative beam was not recorded as it was sufficiently small to have an insignificant effect on the calculation).

d) Readings with the deflection voltage off

Time (beam on)	31.788	seconds
(beam off)	27.853	seconds
Photomultiplier counts (beam on)	58440	
(beam off)	86	
Neutral detector reading	1	
scale	5	mV

True counts (deflector on) $= 47249 - \frac{22.0}{19.3}\,61 =$ 47179

(deflector off) $= 58440 - \frac{31.8}{27.9}\,86 =$ 58342

F^0 = Neutral fraction $= \frac{1x2x58342}{1x5x47179} =$ 49.5 percent

Neutral detector calibration constant

$$K = \frac{12.83x10x10^{-8}x1.26x10^{19}x\frac{58342}{47179}}{(1-.495)x1x5} = 7.91 \times 10^{12}$$

Counts per particle in the total beam leaving the foil

$$= \frac{58342}{1x5x7.91x10^{12}} = 1.475 \times 10^{-9}$$

Now, the 3914 Å filter was inserted and nitrogen gas bled into the analysis chamber. the same data taking and analysis procedures are followed; the data and results are shown in Table III. Figure 30 shows a plot of the counts/particle vs the nitrogen pressure. The finite net counting rate at zero pressure is observed in all cases and is attributed to H_ζ decay photons from atoms produced in the foil. The straight line shown is a least squares fit and has the equation

$$\text{Counts/particle} = 0.974 \times 10^{-4} \times \text{pressure} - 0.343 \times 10^{-10}$$

TABLE III

A sample nitrogen calibration showing data and results

DATA										RESULTS	
		Time (sec)		Photomultiplier Counts		Neutral Detector scale(mV) reading		Positive beam detector reading	scale		
Pressure (torr)	Deflection Voltage	beam on	beam off	beam on	beam off				(amp)	Neutral Fraction	Counts / Particle
6.5×10^{-8}	ON	22.481	19.696	975	195	1	2	12.84	10×10^{-8}	41.8%	2.00×10^{-11}
	OFF	29.927	26.009	1085	262	1	5				
2.25×10^{-6}	ON	21.681	18.972	6517	471	1	2	12.85	10×10^{-8}	49.3%	1.87×10^{-10}
	OFF	30.187	26.330	7731	320	1	5				
4.25×10^{-6}	ON	21.932	19.192	12448	239	1	2	12.93	10×10^{-8}	51.8%	3.61×10^{-10}
	OFF	30.792	26.969	16105	308	1	5				
5.95×10^{-6}	ON	22.454	19.670	19412	239	1	2	12.84	10×10^{-8}	51.9%	5.69×10^{-10}
	OFF	30.878	27.031	25228	357	1	5				
9.0×10^{-6}	ON	23.104	20.104	30048	480	1	2	12.70	10×10^{-8}	54.7%	8.35×10^{-10}
	OFF	31.825	27.809	40725	349	1	5				

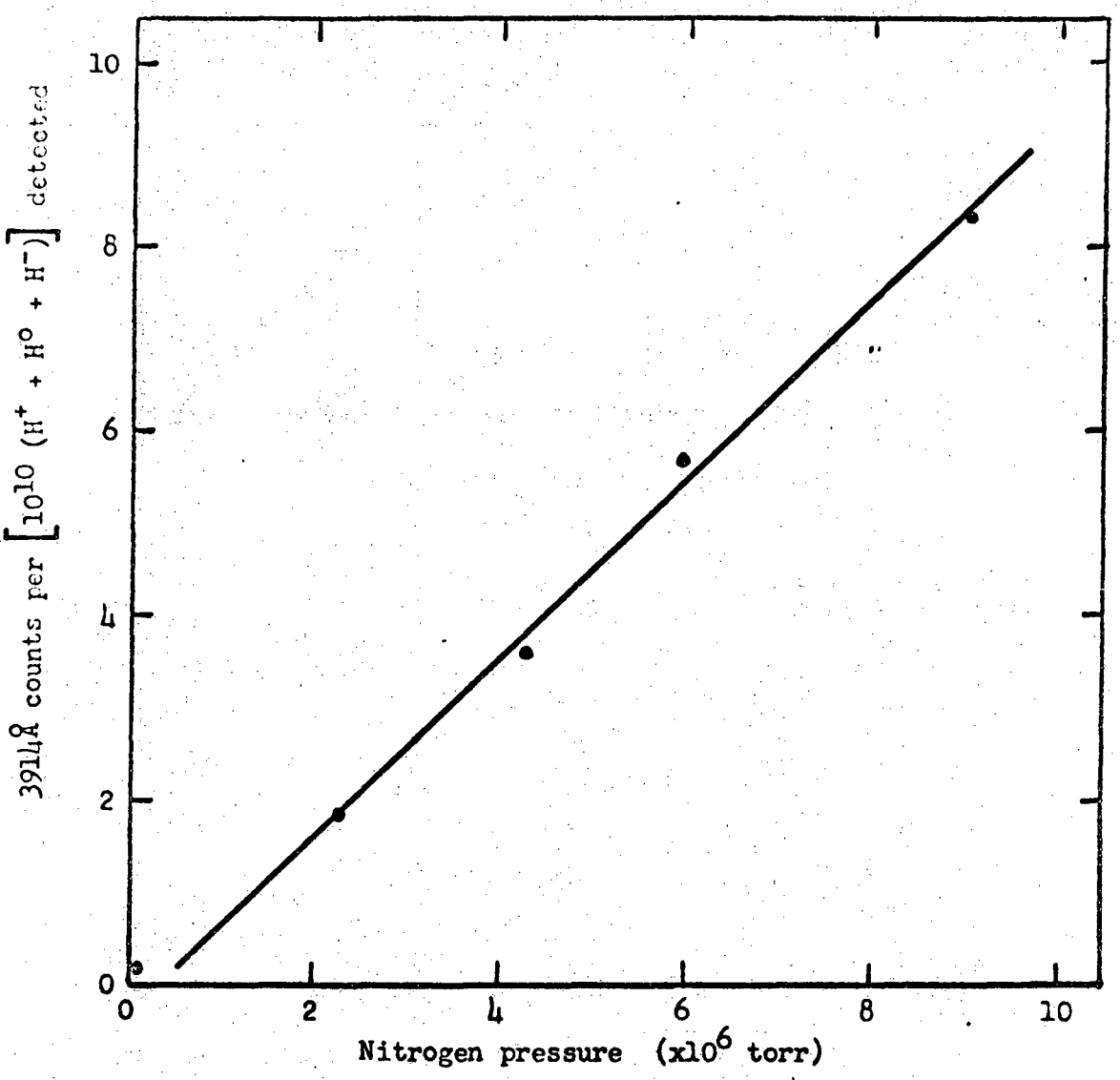

XBL 7012-7442

Fig. 30. A sample calibration of the optical efficiency using the 3914 Å band head of N_2^+. The line shown is a least squares fit.

The slope of the line in Fig. 30 is therefore

$$\frac{d(\text{counts/particle})}{dp} = 4.83 \times 10^{16}\ \epsilon\sigma$$

$$\epsilon = \frac{0.974 \times 10^{-4}}{4.83 \times 10^{16}\ \sigma} = \frac{2.02 \times 10^{-21}}{\sigma}$$

To this we must add the relative efficiencies[40] of the two filters which are

$$\frac{\epsilon_{4101}}{\epsilon_{3914}} = 1.45$$

$$\epsilon = \frac{2.02 \times 10^{-21}}{\sigma} \times 1.45 = \frac{2.93 \times 10^{-21}}{\sigma}$$

From Fig. 25 and Fig. 26 we see that at 55 keV the interaction cross sections are approximately

$$\sigma_{D^+} = 5.5 \times 10^{-17}\ \text{cm}^2$$

$$\sigma_{D^0} = 2.8 \times 10^{-17}\ \text{cm}^2$$

Since the neutral fraction is 51.9%, the effective cross section is

$$\sigma_{eff} = F^0\sigma_{D^0} + (1 - F^0)\sigma_{D^+} = 4.1 \times 10^{-17}\ \text{cm}^2$$

In the above calculation we have assumed, in the absence of any data to the contrary, that the cross section for D^- impact is the same as for D^+ impact. Only in the case of low energy beams through magnesium does D^- form a significant fraction of the emerging beam.

Thus the nitrogen calibration gives the optical efficiency of the system to be

$$\epsilon = 7.15 \times 10^{-5}$$

From Fig. 27 we see that at 55.2 keV the decay correction is 170. We have now accumulated all the data necessary, and get as a result

$$N_6^0 = \frac{(\text{counts/particle}) \times (\text{decay correction})}{\epsilon}$$

$$= \frac{1.475 \times 10^{-9} \times 170}{7.15 \times 10^{-5}} = 3.51 \times 10^{-3}$$

2. High Voltage Gap Method

Using the data in Table IV, we can analyze the curves in Fig. 28. First, however, we have to make one slight correction to the formula given in Appendix A. Since the beam current might change between the time the currents were measured and the time the X-Y recorder plot was made, we replace I_{TOT}^0 by

$$I_{TOT}^0 \frac{I_c^+}{I^+}$$

Where I_c^+ is the positive beam current at the time the curves were plotted. We have therefore

$$\text{Beam energy} = 75.3 \frac{15.61}{16.38} = 71.8 \text{ keV}$$

For a dirty carbon foil

$$F^0 = \frac{2}{3.65} = 54.8\%$$

$$F^- = \frac{I^-}{I^- + I^+} (1-F^0) = \frac{7 \times 10^{-10}}{9 \times 10^{-10} + 5 \times 10^{-8}} (1-.548) = 0.62\%$$

Accelerator Energy = 75.3 KeV

Deflector Voltage with foil = 15.61 KeV

without foil = 16.38 KeV

		Dirty Foil	Foil with Layer of Clean Carbon
I^+		5×10^{-8}	2.25×10^{-8}
I^-		7×10^{-10}	3.8×10^{-10}
I^o_{TOT}		3.3×10^{-8}	1.65×10^{-8}
Neutral Detector	Deflector ON	2.0	1.0
	Deflector OFF	3.65	2.15
(From Fig. 28) m		6.15×10^{-11}	3.1×10^{-11}
I^+_c		4.7×10^{-8}	2.25×10^{-8}

Data Associated with Fig. 28

TABLE IV

$$N_6^0 = 4.69 \times 3.1 \times 10^{-11} \times \frac{1 - 0.465}{1.65 \times 10^{-8} \times \frac{2.25 \times 10^{-8}}{2.25 \times 10^{-8}}} \times \frac{2.25 \times 10^{-8} - 3.8 \times 10^{-10}}{2.25 \times 10^{-8} + 3.8 \times 10^{-10}}$$

$$= 0.00455$$

3. Foil Burnup

In a sample run, the following data were collected:

Beam energy = 15 kV

Beam intensity = 0.55 μA

Beam spot size = 1/16 in. diameter

Recorder chart speed = 4 in. per hr.

Chart length to break = 6.88 in.

Therefore

$$\text{Beam area} = \frac{\pi d^2}{4} = \frac{2 \times (2.54/16)^2}{4} = 0.02 \text{ cm}^2$$

$$\text{Irradiation time} = \frac{6.88}{4} = 1.72 \text{ hr} = 6200 \text{ sec}$$

$$\text{Total charge through foil} = \frac{0.55 \times 10^{-6} \times 6200}{0.02} = 0.17 \text{ coulomb/cm}^2$$

C. Estimates of Uncertainties

1. Optical Method

The uncertainties incurred in this method can be divided into data errors and systematic errors. The former would include statistical errors in the count rates (~ 1%), in the neutral fractions (~ 3%), in the positive beam electrometer and integrator (~ 5%), and in slope errors from the nitrogen calculation (~ 10%).

Systematic errors would include the measurement of the interaction length (~ 10%), the calculation of the decay correction (~ 15%), the reported values of the 3914 Å nitrogen excitation cross section (~ 30%) (see appendix H), and the measurement of the relative filter transmissions (~5%).

Thus the total data random uncertainty is ±12%, with a possible systematic error of ±35%. At low energies, the data errors would tend to increase for several reasons: (1) F^0 is large so $\Delta F^0/(1 - F^0)$ will be large; (2) F^- is large so the error associated with it has to be added in; (3) beam currents are small due to the inefficiency of the accelerator at low energies, and hence the quality of all measurements would tend to decrease; (4) the approximation used in evaluating the decay correction is less valid; and (5) the error in the nitrogen excitation cross section is greater.

2. High Voltage Gap Method

Since integrators were not used, the errors in meter readings will tend to be greater in this method. The data errors are neutral fraction (~ 7%), I^0_{TOT} (~ 7%), slope of X-Y plot (~ 10%), errors in charge beam measurements (~ 3%). This latter quantity is usually small as charge measurements always appear as ratios.

Systematic errors would include those in the measurements of b and c. For b I will assume ±20% based on the consistency of the results of several experimenters,[19,39,41] so the error in $\sqrt{b}$ is ±10%. The geometric factor c is the result of two measurements, each of which would have a possible 10% error so the error in c is ~14% and the error in $\sqrt{c}$ is ±7%.

Thus the total random data errors are ±14% and the total systematic error is ±12%. At lower energies the error will be greater because (1) F^0 is large so $\Delta F^0/(1 - F^0)$ will be large; (2) F^- is large so $(I^+ - I^-)/(I^+ + I^-)$ will have a larger error; (3) I^0_{TOT} will be small due to the cancellation of the positive and negative beams and will be greatly affected by small steering effects; (4) beam currents are small so the quality of all measurements is poor; (5) noise pickup becomes comparable to the ionized current and hence the slope measurements become poor; and (6) the gap voltage is comparable to the beam energy and hence large steering effects occur.

D. Stopping Power

The stopping power of a target foil is defined by the equation[42]

$$-\frac{dE}{dx} = NS,$$

where N is the atom density of the target and S is the stopping cross section per atom. In the energy range of interest (< 100 keV), S can be written as the sum

$$S = S_e + S_n,$$

where S_e represents the energy loss to electrons in the target and S_n represents the energy loss to recoiling atoms.

S_n is small compared to S_e but becomes more significant at incident velocities below $v_0 = e^2/\hbar$, the velocity of the first Bohr orbit in hydrogen (25 keV for protons). Van Wijngaarden and Duckworth[42] give the following equations for the stopping cross sections

$$S_e = Z_1^{5/6}\left(8\pi e^2 a_0\right)\left[\frac{Z_1 Z_2}{(Z_1^{2/3} + Z_2^{2/3})^{3/2}}\right]\left(\frac{E}{E'}\right)^{1/2},$$

where Z_1 and Z_2 are the atomic numbers of the incident particle and target atom, respectively, a_0 is the Bohr radius, E is the incident particle energy, and E' is the kinetic energy of the incident particle when its speed equals $v_0 Z_1^{2/3}$, and

$$S_n \simeq 2\pi \frac{M_1}{M_2} e^4 \frac{Z_1^2 Z_2^2}{E} \ln\left[\frac{2a}{Z_1 Z_2 e^2}\frac{M_2}{M_1 + M_2}E\right],$$

where M_1 and M_2 are the respective masses of the incident particle and target atom and a is a screening parameter given by

$$a = \frac{0.8853\, a_0}{(Z_1^{2/3} + Z_2^{2/3})^{1/2}} .$$

More detailed discussions of stopping power can be found in Refs. 43, 44, and 45.

Three common units are used in reporting stopping powers, namely:

$$\frac{\text{keV}}{\mu\text{g/cm}^2} , \qquad \frac{\text{eV}}{\text{atom/cm}^2} , \qquad \text{and } \frac{\text{eV}}{\text{Å}} .$$

They are related by

$$1\ \frac{\text{keV-cm}^2}{\mu\text{g}} = 10^9\ \frac{W}{N}\ \frac{\text{eV-cm}^2}{\text{atom}}$$

$$1\ \frac{\text{keV-cm}^2}{\mu\text{g}} = 10\ d\ \frac{\text{eV}}{\text{Å}}$$

where W is the atomic weight of the target atom, N is Avogadro's number, and d is the density of the foil in gm/cm^3.

In Figs. 31 through 36 I have plotted the available stopping power data[42,46-62] for six different foil materials, using the above conversions where necessary in order to use the same axes for all curves. In some cases, as for instance carbon (Fig. 35) and copper (Fig. 36), there is good agreement among the various experimenters but others (gold, Fig. 34) show as much as a factor of 3 variation in reported values. In an attempt to minimize these errors, I plotted the stopping power vs Z_2 at several energies and drew smooth curves through the points (Fig. 37). This graph is also useful for obtaining reasonable values for the stopping power in foils for which data is questionable or nonexistent. The region between Z = 47 (silver) and Z = 79 (gold)

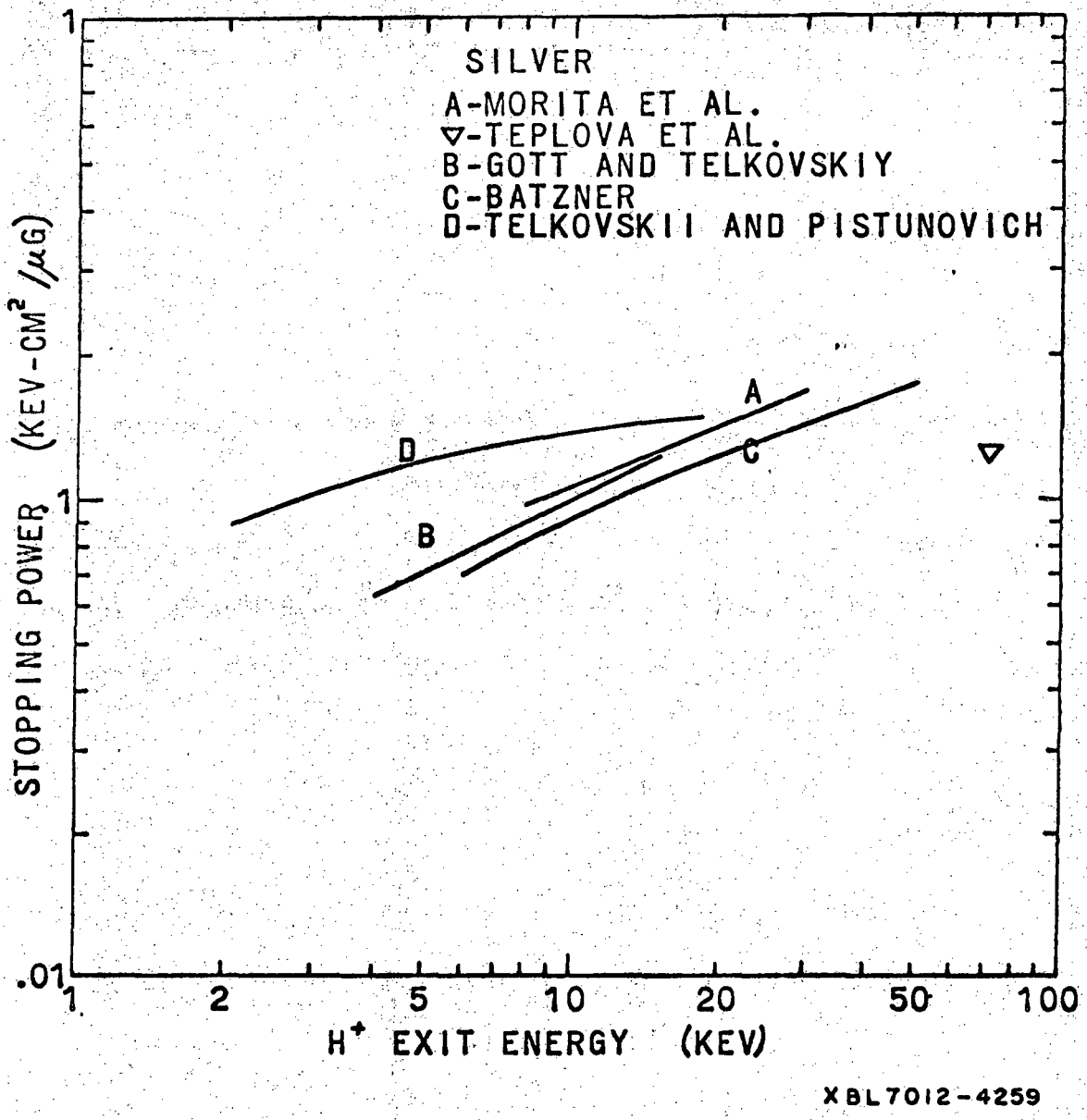

Fig. 31. Stopping power of silver foils for protons. A, Ref. 46; ▽, Ref. 47; B, Ref. 48; C, Ref. 49, D, Ref. 50.

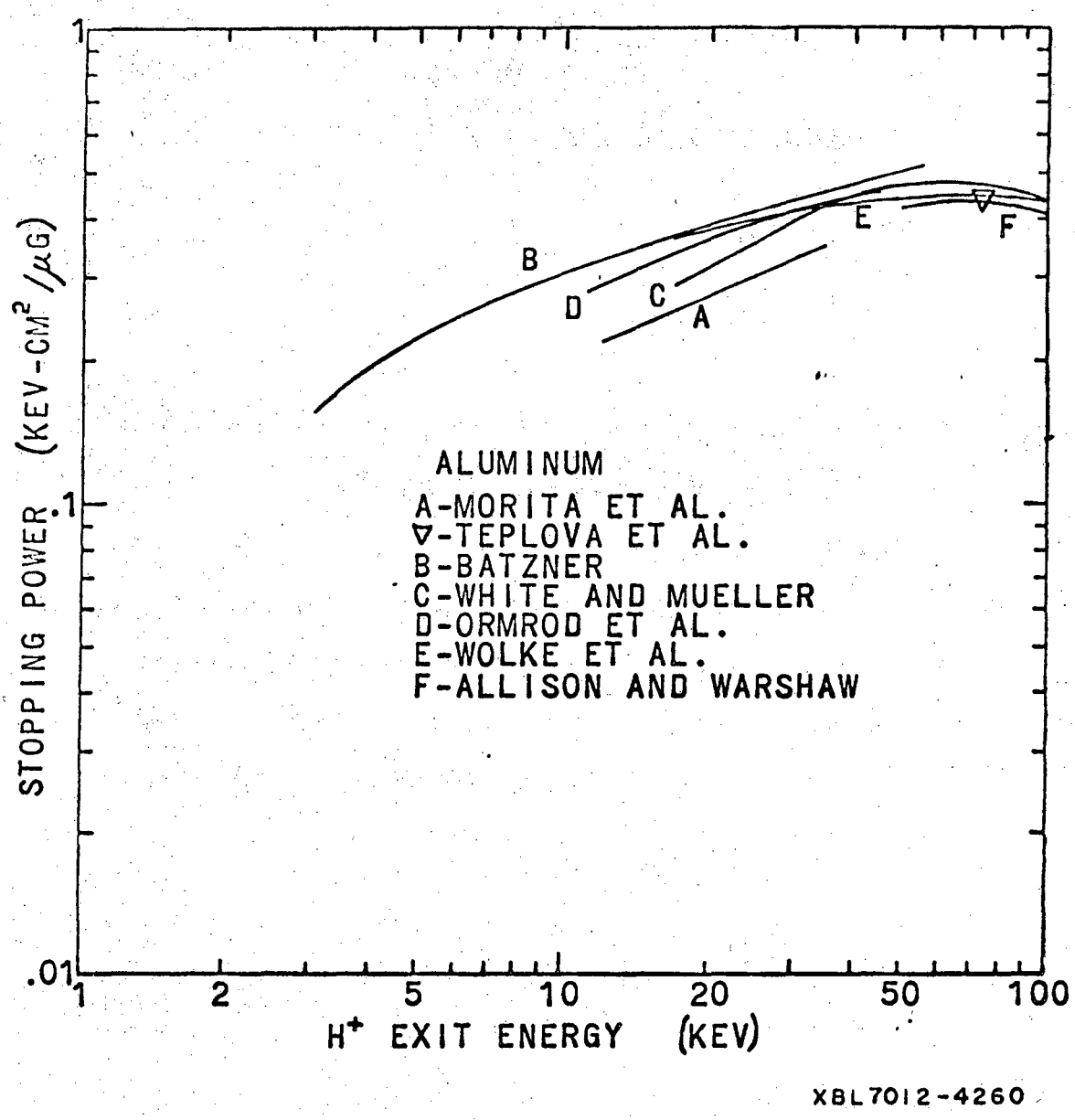

Fig. 32. Stopping power of aluminum foils for protons. A, Ref. 46; ∇, Ref. 47; B, Ref. 49; C, Ref. 51; D, Ref. 52; E, Ref. 53; F, Ref. 54. The data of Ref. 53 for tritons is plotted at one-third of the triton energy.

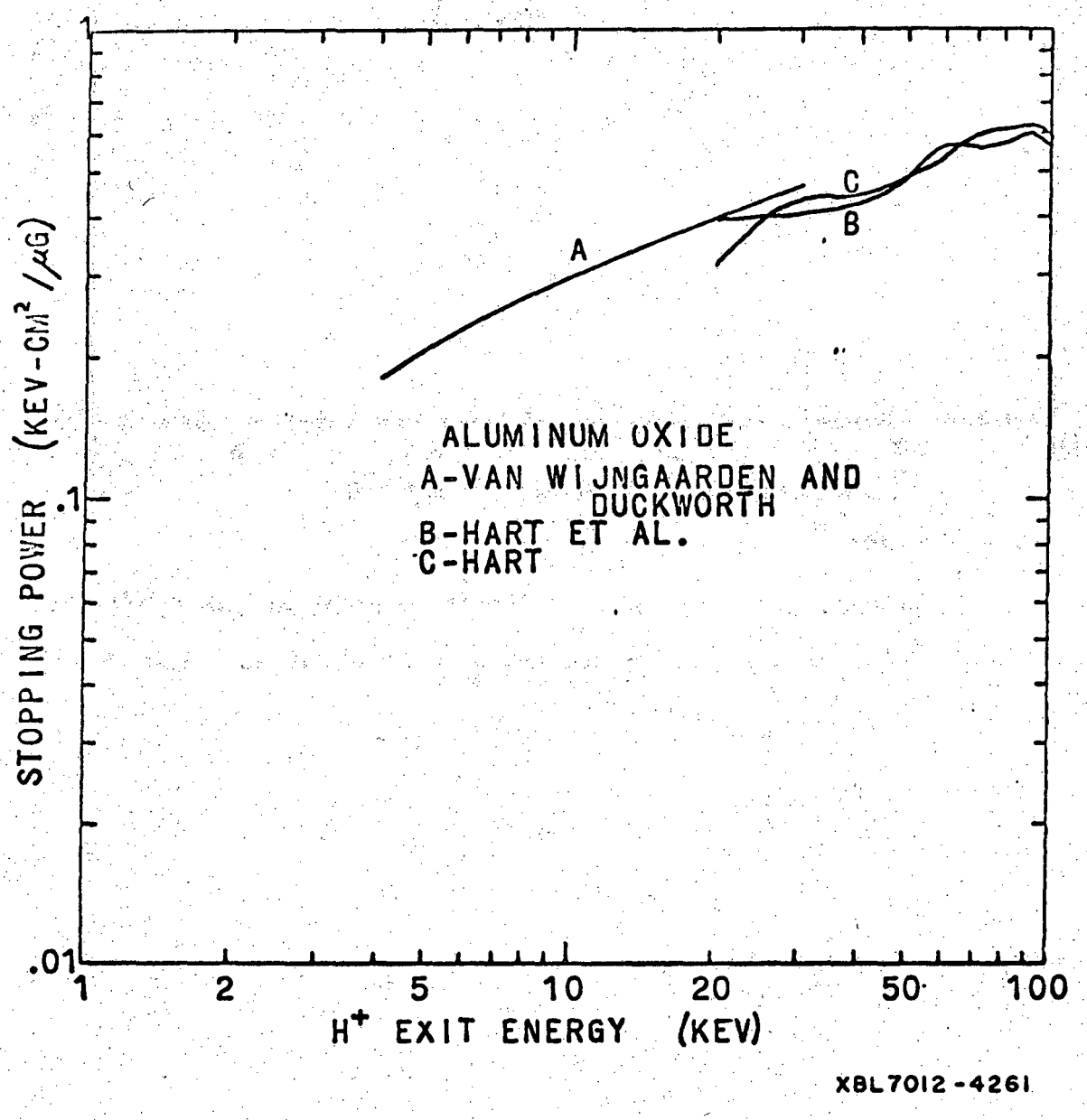

Fig. 33. Stopping power of aluminum oxide foils for protons.

A, Ref. 52; B, Ref. 55; C, Ref. 56.

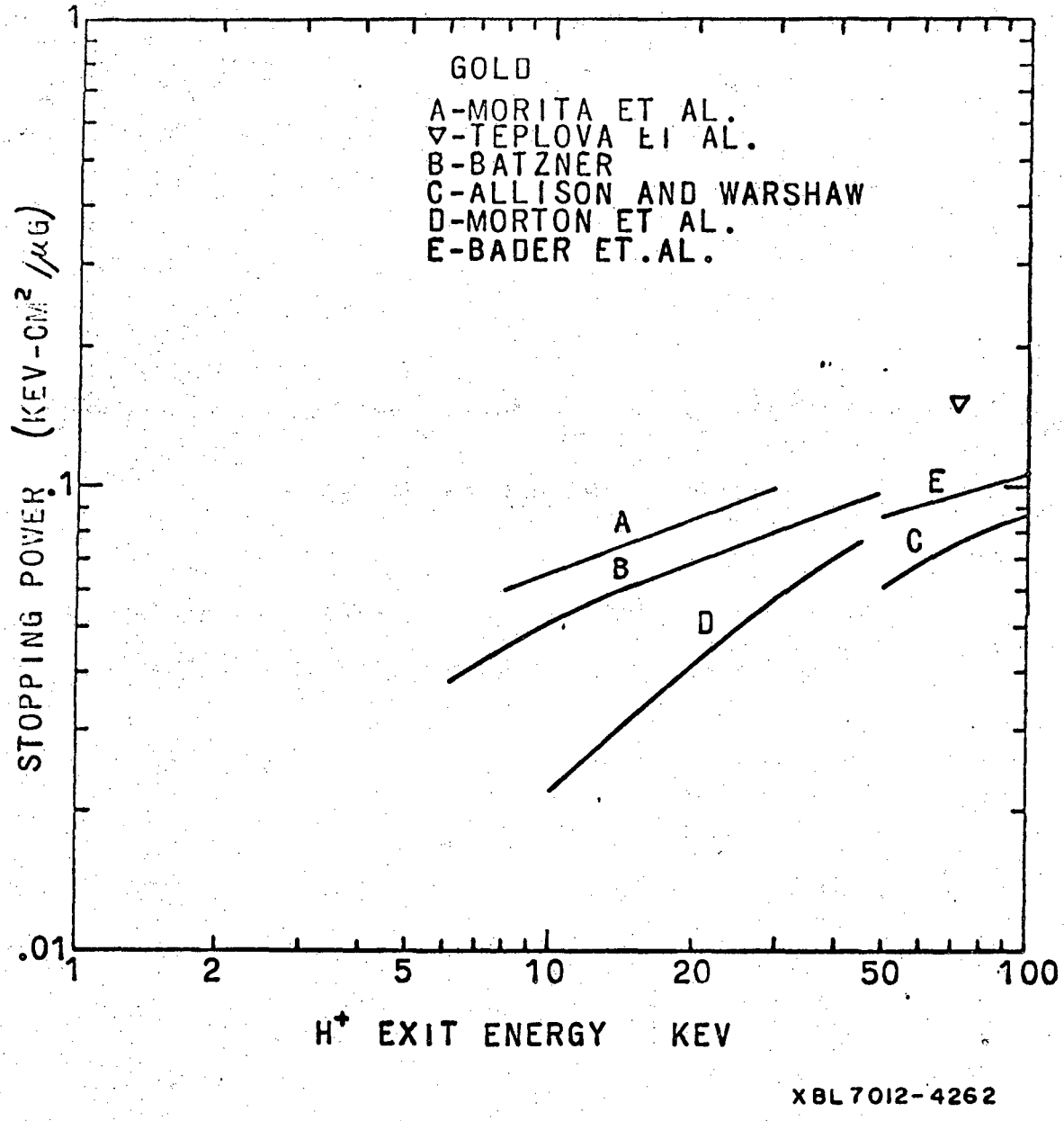

Fig. 34. Stopping power of gold foils for protons. A, Ref. 46; ▽, Ref. 47; B, Ref. 49; C, Ref. 56; D, Ref. 57; E, Ref. 58.

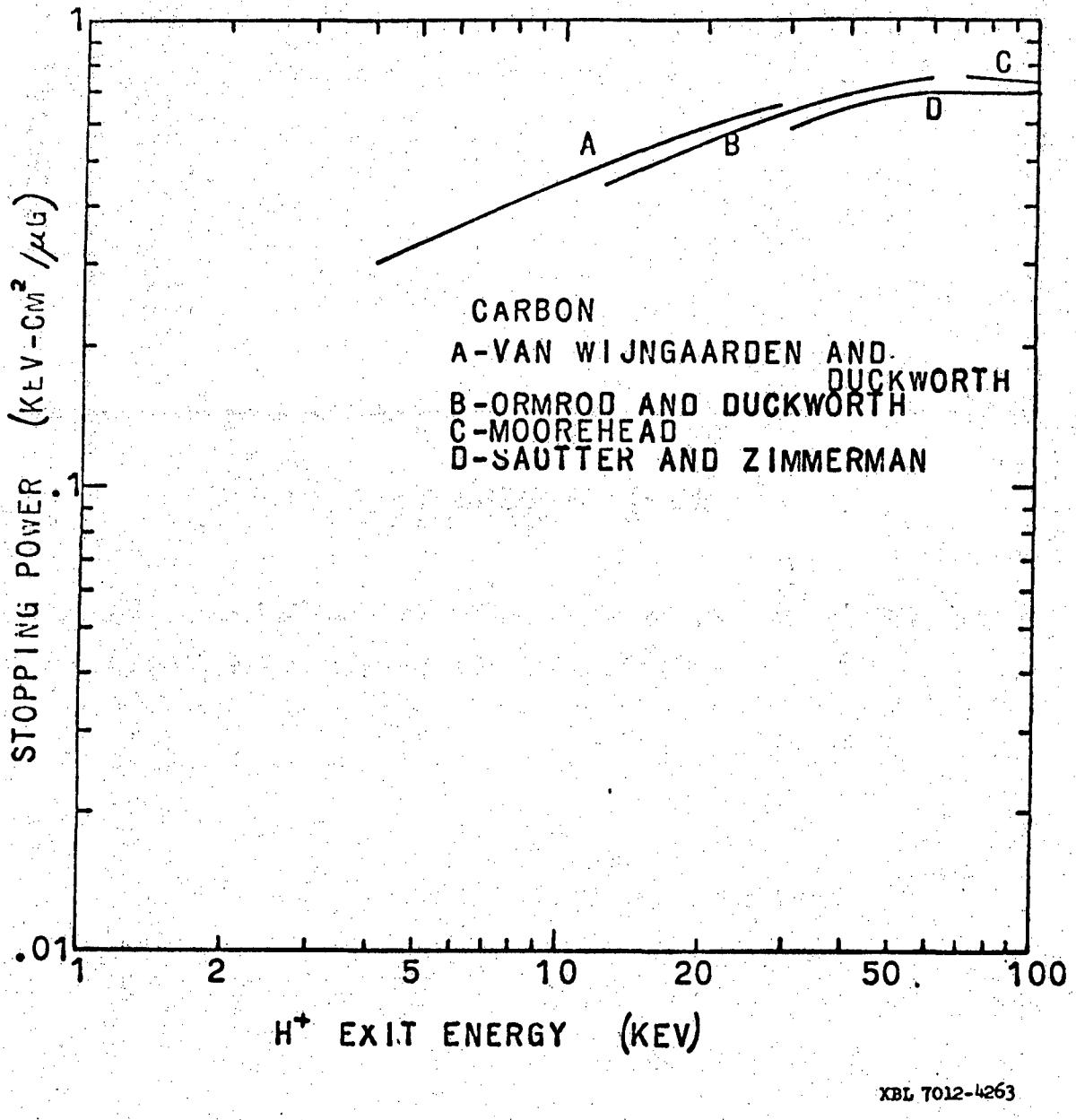

Fig. 35. Stopping power of carbon foils for protons. A, Ref. 42; B, Ref. 59; C, Ref. 60; D, Ref. 61.

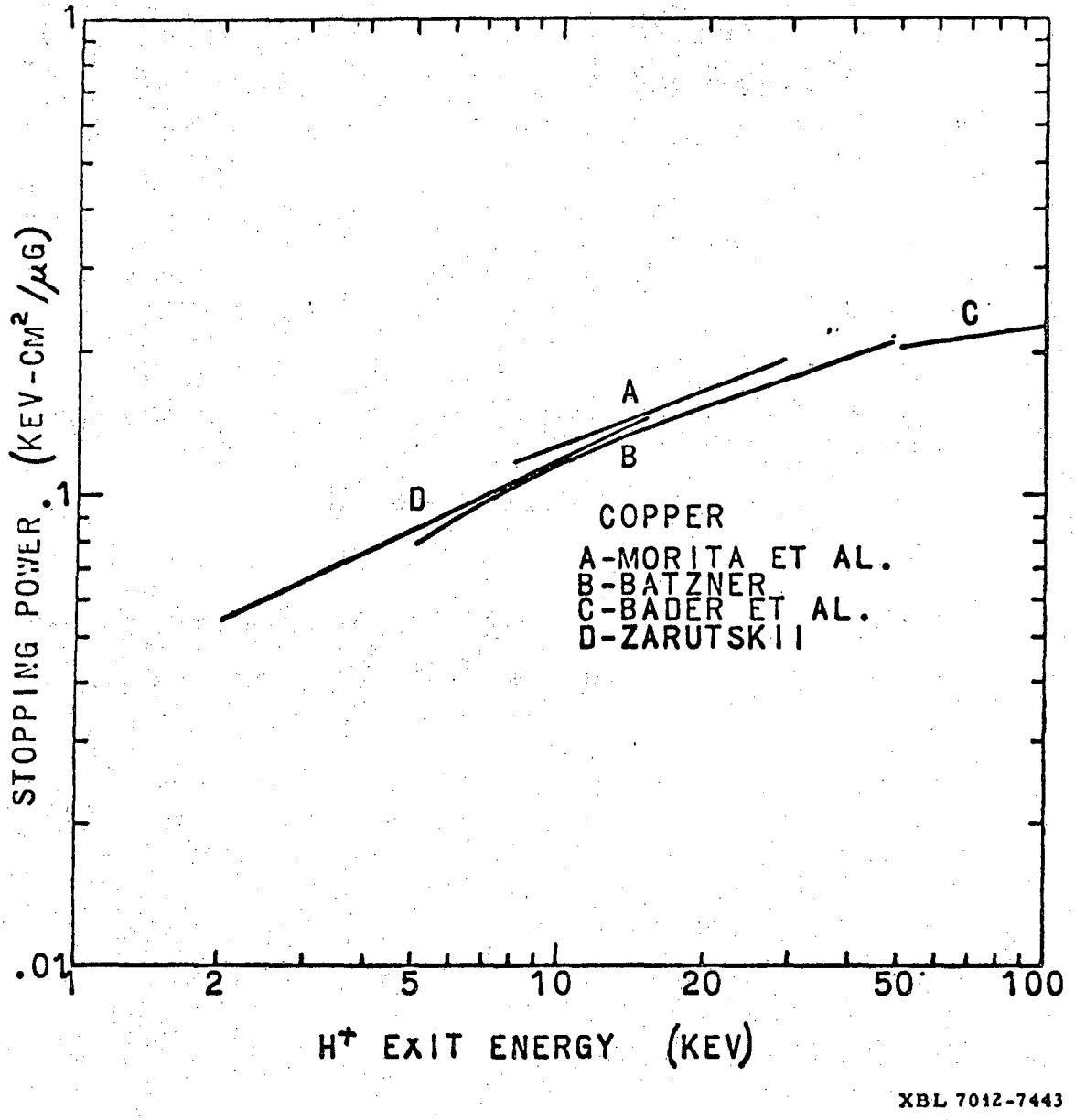

Fig. 36. Stopping power of copper foils for protons. A, Ref. 46; B, Ref. 49; C, Ref. 58; D, Ref. 62.

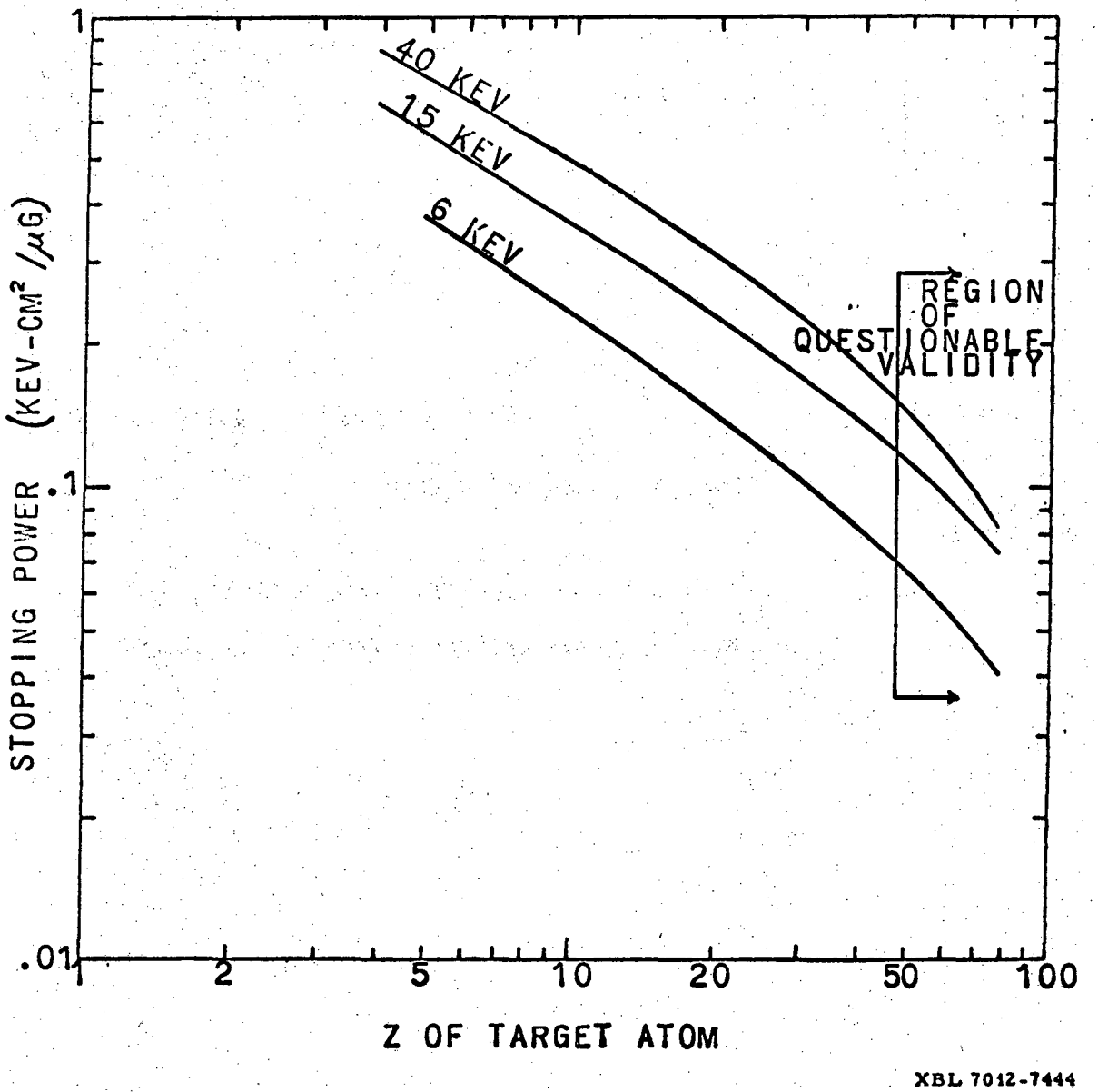

Fig. 37. Stopping power of foils as a function of the atomic number of the target and the incident beam energy.

is of questionable validity due to the large range of variation in the gold data.

E. Scattering from foils

In the energy range of interest (< 100 keV) there is no adequate theory for describing scattering from thin foils.[63] Moliere theory is not applicable due to the low energy[64] and Rutherford scattering theory doesn't apply because there is some multiple scattering. In this section, therefore, I shall try to find an empirical relation between reported scattering data.

Gott and Telkovskii[65] have studied scattering of protons and deuterons in the energy range $1.8 < E < 36$ keV through a 21 $\mu g/cm^2$ silver foil. Assuming a Gaussian distribution

$$f(\theta) = \frac{c}{\alpha} \exp - \frac{\theta^2}{2\alpha^2}$$

where $\alpha = (\overline{\theta^2})^{1/2}$ = rms scattering angle and using arguments based on the interaction potential they obtain

$$\alpha^2 = \frac{0.51 e^2 a Z_1 Z_2 (M_1+M_2) nd}{EM_2} \int_0^{\pi} \theta^2 \frac{\cos \theta/2}{\sin^2 \theta/2} d\theta$$

where

e = electronic charge

$a = \dfrac{.8853 a_0}{(Z_1^{2/3}+Z_2^{2/3})^{1/2}}$

a_0 = first Bohr radius

Z_1, Z_2, M_1, M_2 = atomic numbers and weights of incident particle and target atom respectively

n = atome density of target

d = thickness of target

E = incident particle energy

$$\int_0^{\pi} \theta^2 \frac{\cos \theta/2}{\sin^2 \theta/2} \, d\theta = 8 \int_{\pi/2}^{0} \phi^2 \, d(\csc \phi) = 9.57$$

If we let W be the foil thickness in $\mu g/cm^2$ then obviously

$$nd \sim \frac{W}{M_2}$$

and we have

$$\alpha \sim \sqrt{\frac{Z_2}{M_2} \frac{W}{E}} \approx \sqrt{\frac{W}{E}}$$

Inserting the proper values for a 21 $\frac{\mu g}{cm^2}$ silver foil, we get

$$\alpha = 125/\sqrt{E}$$

(α in degrees, E in keV). Experimentally, however, Gott and Telkovskii report that their data is better fit by

$$\alpha = 38/\sqrt{E}$$

Adding the W dependance this becomes

$$\alpha = 8.3 \sqrt{\frac{W}{E}}$$

Bogdanov and Lebedev[63] have measured the scattering of 15 to 90 keV protons in thin nickel foils. For foils in the thickness range of 11 to 30 $\mu g/cm^2$ I have found that their data fits the empirical form

$$f(\theta) \approx \exp(-.138 \frac{E}{W} \theta)$$

(E in keV, W in $\frac{\mu g}{cm^2}$, θ in degrees)

From this we find

$$\alpha = \sqrt{\overline{\theta^2}} \approx 10.25 \frac{W}{E} \text{ degrees.}$$

Note the difference in both W and E dependence between Gott and Telkovskii's results and Bogdanov and Lebedev's. The difference in magnitude in the region of overlap, however, is not that great, as can be seen in Fig. 38 where Bogdanov and Lebedev's results are shown with $W = 21\ \mu g/cm^2$ to correspond to Gott and Telkovskii's silver foil.

Wax and Bernstein[20] have measured the scattering through very thin (2 to $5\ \mu g/cm^2$) carbon foils in the energy range $3 < E$ 10 keV. In this range, their results can be written as

$$\theta_{1/2} = \frac{55.5}{E}$$

where $\theta_{1/2}$ is the half-angle at the half-maximum of the distribution (degrees) and E is the incident energy.

If we assume a weight of $3\ \mu g/cm^2$ for this foil, we would have

$$\theta_{1/2} = 18.8 \frac{W}{E}$$

which is larger than Bogdanov and Lebedev's results and considerably larger than Gott and Telkovskii's. The main discrepancy hinges on whether the energy dependence of the mean scattering angle at low energies is $E^{-1/2}$ as used by Gott and Telkovskii or E^{-1} as used by Wax and Bernstein. Unfortunately, there are no other data in that energy range nor any theory which extends to those energies.

At higher energies ($E > 75$ keV) Bednyakov et al.[64,66,67]

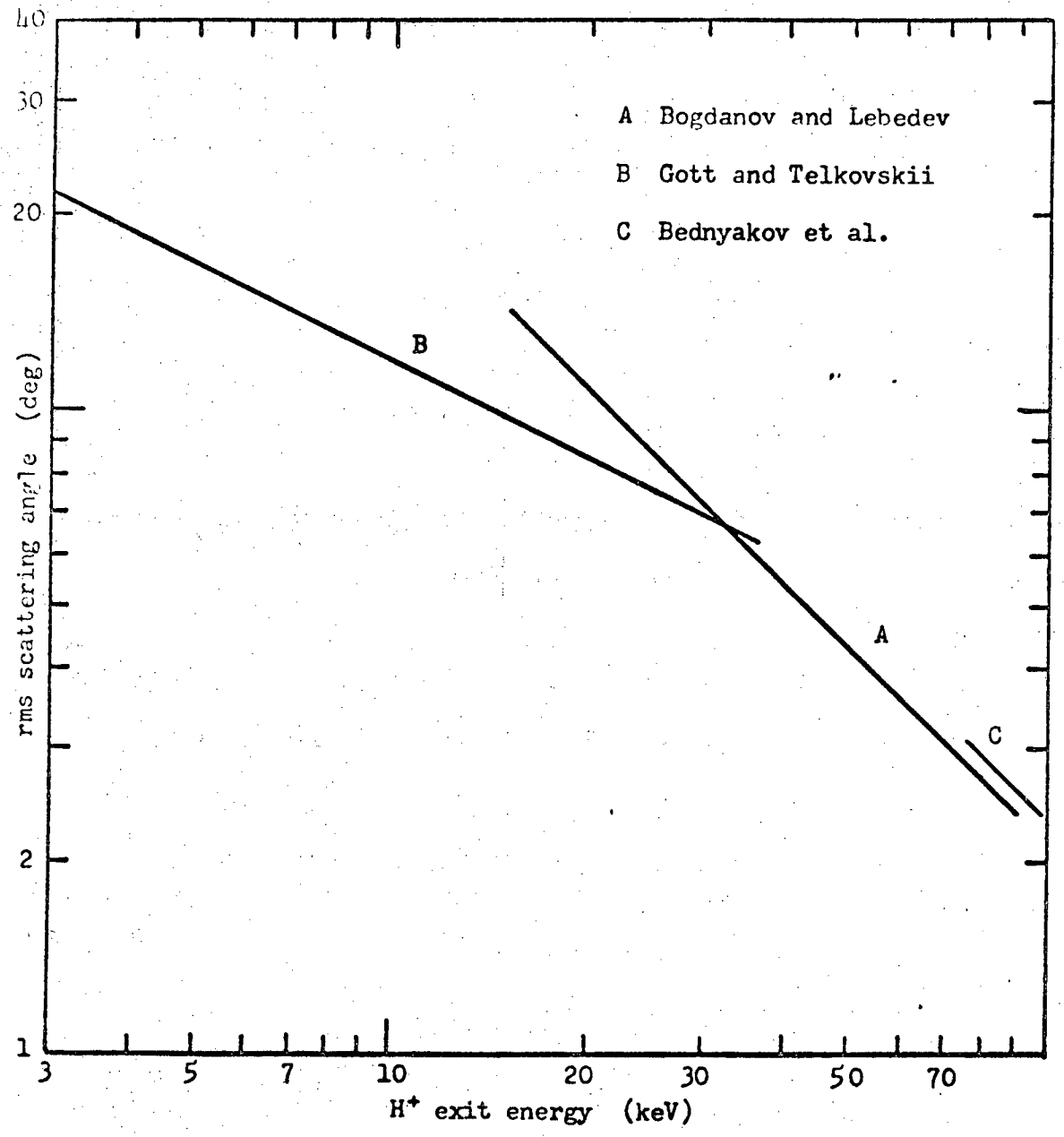

XBL 7012-7447

Fig. 38. Rms scattering angle of proton beams in a 21 $\mu g/cm^2$ silver foil vs energy. A, Ref. 63, extrapolated using the formula $\alpha = 10.25\ W/E$; B, Ref. 65; C, Refs. 64, 66, and 67 extrapolated using the formula $\theta_{1/2} = 11.4\ Z^{1/4} W^{2/3}/E$.

have measured scattering from foils of carbon, aluminum, and copper. At these high energies Moliere's theory applies and the authors report good agreement between experiment and theory. An empirical fit to their data gives

$$\theta_{1/2} = 11.4 \frac{Z^{1/4} W^{2/3}}{E}$$

where in this case E is an average energy of the proton in the foil

$$E = \sqrt{E_0 E_f}$$

An average was used in this case, as some of the foils in the experiment were as thick as 570 $\mu g/cm^2$.

This empirical formula is plotted in Fig. 38 and is seen to correspond closely with the results of Bogdanov and Lebedev; several points however, should be noted. First, the Bednyakov et al. data is in the form of $\theta_{1/2}$ and not α. The relation between these angles is a function of the distribution and for a Gaussian it is

$$\theta_{1/2} = 1.18\ \alpha$$

Next, in the energy and foil thickness range of interest, several effects take place which would limit the applicability of any empirical formula. At low energies, protons lose a large fraction of their energy in the foil, making the scattering a stronger function of the foil thickness than expected. For thin foils, the scattered spectrum is a mixture of small angle multiply scattered spectrum and a large angle singly scattered spectrum.[68] This mixture is also a non-linear function of foil thickness.

F. Sputtering from Foils

Robison[21] has developed a formula for transmission sputtering from thin foils by modifying the backward sputtering formula of Pease.[64] Pease assumes that each incident particle will produce a number of "primary knockon" atoms, each one of which will displace more atoms from the foil lattice and this will continue until either the atom escapes the foil or its energy is degraded to the point where it can no longer displace atoms. The number of sidplaced atoms produced per primary knockon is approximately

$$N_d = \frac{\bar{E}}{2E_d}$$

where

E_d = lattice displacement energy

$$= \frac{2M_1M_2}{(M_1 + M_2)^2} \; E_t$$

M_1 = incident particle mass

M_2 = target atom mass

E_t = threshold sputtering energy from Wehner[65]

$\bar{E}$ = average energy of displaced particles

$= \frac{1}{2} (E_{max} + E_d)$

$$E_{max} = \frac{4M_1M_2}{(M_1 + M_2)^2} \; E_o$$

E_o = incident ion energy

The effective collision area per atomic layer is

$$\sigma_d \, n_o^{2/3}$$

where

σ_d = displacement cross section

$$= \frac{\pi a^2 E_A}{e E_o} \left(1 - \frac{E_d}{E_{max}}\right)$$

$$E_A = \frac{2(M_1 + M_2)}{M_2} \, Z_1 Z_2 R_H \, \frac{a_o}{a}$$

R_H = 13.6 ev

a_o = first Bohr radius

$$\frac{a_o}{a} = (Z_1^{2/3} + Z_2^{2/3})^{\frac{1}{2}}$$

e = 2.718 . . . . .

n_o = atomic density

Assuming the atoms lose $\frac{1}{2}$ their energy in each collision, the average energy after n collisions is

$$E_n = (\tfrac{1}{2})^n \bar{E}$$

Eventually, the energy will be below the sublimation energy at the surface, E_s. This will take

$$n = \frac{\log (\frac{\bar{E}}{E_s})}{\log 2}$$

collisions. Assuming the collisions are a random walk process, the number of atomic layers taking part is

$$N = 1 + n^{\frac{1}{2}}$$

where the incident surface layer is considered separately. Thus, Pease's formula for sputtering yield is

$$S = \tfrac{1}{2} \frac{\bar{E}}{2E_d} \sigma_d n_o^{2/3} \left[1 + \left(\frac{\log \frac{\bar{E}}{E_s}}{\log 2} \right)^{\frac{1}{2}} \right]$$

The extra factor of 1/2 accounts for the fact that 1/2 of the atoms will be going the wrong way.

Robison modified this formula as follows to adapt it to transmission sputtering

a) consider energy loss in the foils by redefining:

$$E_{max} = \frac{4M_1M_2}{(M_1 + M_2)^2} E_f$$

$$\sigma_d = \frac{\pi a^2 E_A}{eE_f} \left(1 - \frac{E_d}{E_{max}} \right)$$

E_f = exit energy of beam.

b) The value of $\bar{E}$ used by Pease is the energy transmitted on collision; it should be reduced by the energy loss in displacement, i.e.

$$\bar{E} = \frac{E_{max} + E_d}{2} - E_d = \frac{E_{max} - E_d}{2}$$

c) Add as a multiplicative factor the beam loss due to scattering

$$e^{-\frac{T}{\lambda}}$$

T = foil thickness, $\lambda = \frac{E_o + E_f}{n_o \sigma_d E_f}$

d) Pease excluded the primary knockons as they were headed in the wrong direction. Therefore the factor $\frac{\bar{E}}{2E_d}$ should be replaced by

$$1 + \frac{\bar{E}}{2E_d}$$

Robison's formula is then

$$S = \frac{1}{2}\sigma_d n_o^{2/3}\left(1 + \frac{\bar{E}}{2E_d}\right)\left[1 + \left(\frac{\log \frac{\bar{E}}{E_s}}{\log 2}\right)^{\frac{1}{2}}\right] e^{-\frac{T}{\lambda}}$$

In the energy range $\bar{E} > E_d$ this formula agrees with experiment to within a factor of 2. In the incident energy range $5 < E_0 < 20$ keV and foil thickness range $100 < T < 400$ $\mu g/cm^2$ for sp uttering from a gold foil by deuterons, Robison's equation takes the empirical form

$$S = 10^{-3}\,(11.1 + 1.26E_0 - 0.0337E_0^{\,2} - 0.0373T)$$

Robison's experimental forward sputtering results are shown in Fig. 39. He showed that the backward sputtering yields are about twice as large.

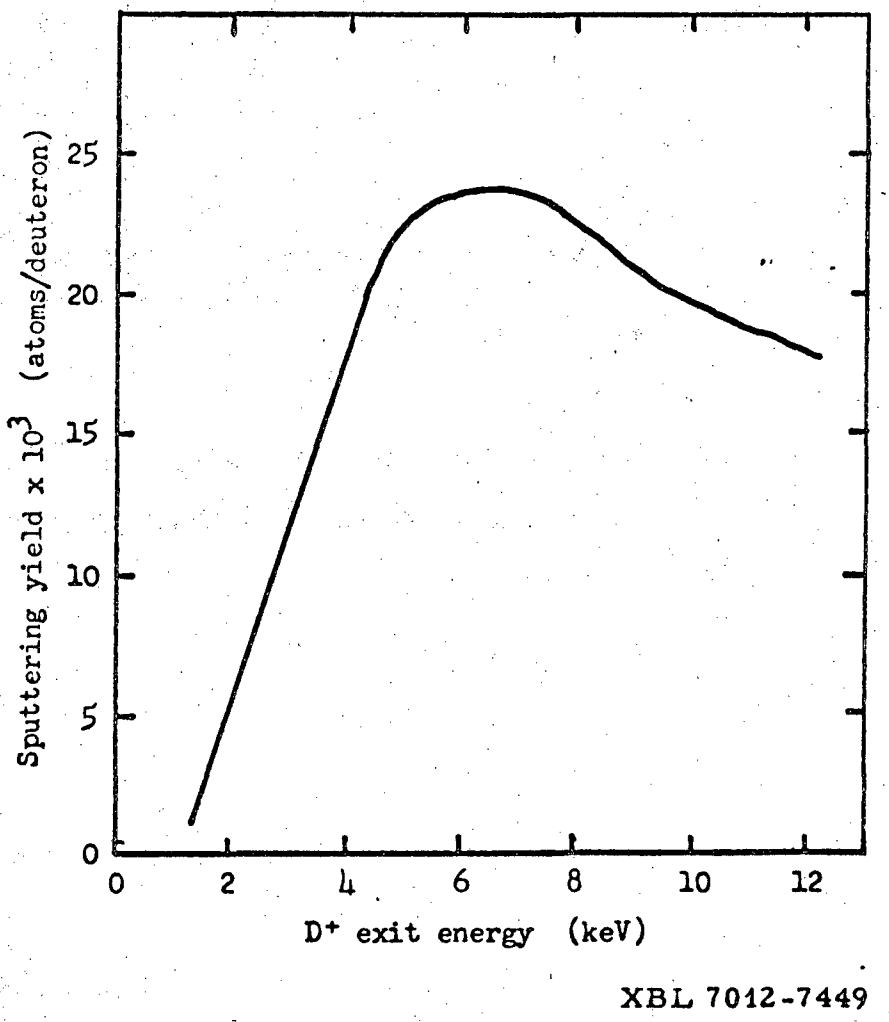

XBL 7012-7449

Fig. 39. Forward sputtering yield for deuterons on a gold foils as a function of exit energy (from Ref. 27).

G. Evaporation from a Carbon Foil

To make an estimate of the evaporation rate from a foil, we will assume that the only heat loss mechanism is black body radiation.

From Appendix D, we find that the stopping power of a carbon foil for 20 keV deuterons is 0.45 keV/$\frac{\mu g}{cm^2}$ so that in a five microgram foil, the beam will lose about 2.25 keV. Thus, for a beam of mA/cm^2, the energy deposition rate in the foil is given by

$$\Delta E_{gain} = 2.25 \times 10^7 \, \phi \, \frac{ergs}{cm^2 \, sec} .$$

Since the energy is radiated from both sides of the foil, the energy loss rate is given by

$$\Delta E_{loss} = 2\epsilon\sigma T^4$$

where $\epsilon \approx 0.85$ is the emissivity of graphite. Equating these we find the relation

$$T^4 = 2.33 \times 10^{11} \, \phi$$

for T in degrees Kelvin.

Table V shows the vapor pressure[24] of carbon in the region from 2000°K to 2600°K. A rough fit to that data gives

$$P = 1.111 \times 10^{-143} T^{40.2} \text{ atm.}$$

Converting to more practical units, we have

$$P = 1.126 \times 10^{-137} \, T^{40.2} \, \frac{dynes}{cm^2} .$$

Making use of the relations

Table V. Vapor Pressure of Carbon (from Ref. 24)

T (^{o}K)	Vapor Pressure (atm)
2000	6.00×10^{-11}
2100	5.20×10^{-10}
2200	3.76×10^{-9}
2300	2.30×10^{-8}
2400	1.22×10^{-7}
2500	5.60×10^{-7}
2600	2.32×10^{-6}

$$P = nkT$$

$$\bar{v} = \sqrt{\frac{8kT}{\pi m}}$$

and assuming a sticking probability of unity, we find that the evaporation rate is

$$2\,\frac{n\bar{v}}{4} = \frac{\sqrt{2}\,P}{\sqrt{\pi mkT}}$$

$$= 1.71 \times 10^{-118}\, T^{39.7}\ \frac{\text{atoms}}{\text{cm}^2\,\text{sec}}$$

or in terms of the beam flux, the rate is

$$1.29 \times 10^{-5}\, \phi^{9.9}\ \frac{\text{atoms}}{\text{cm}^2\ \text{sec}}$$

which is a very strong function of the flux.

From the foil burning experiments we see that removal of about 30 percent of the foil by sputtering is sufficient to break the foil. In Fig. 40 I have plotted the time necessary to evaporate 30 percent of a 5 μg carbon foil in terms of the incident flux. It can readily be seen that at the beam levels of the experiment (0.03 to 0.3 mA/cm^2) evaporation was negligible.

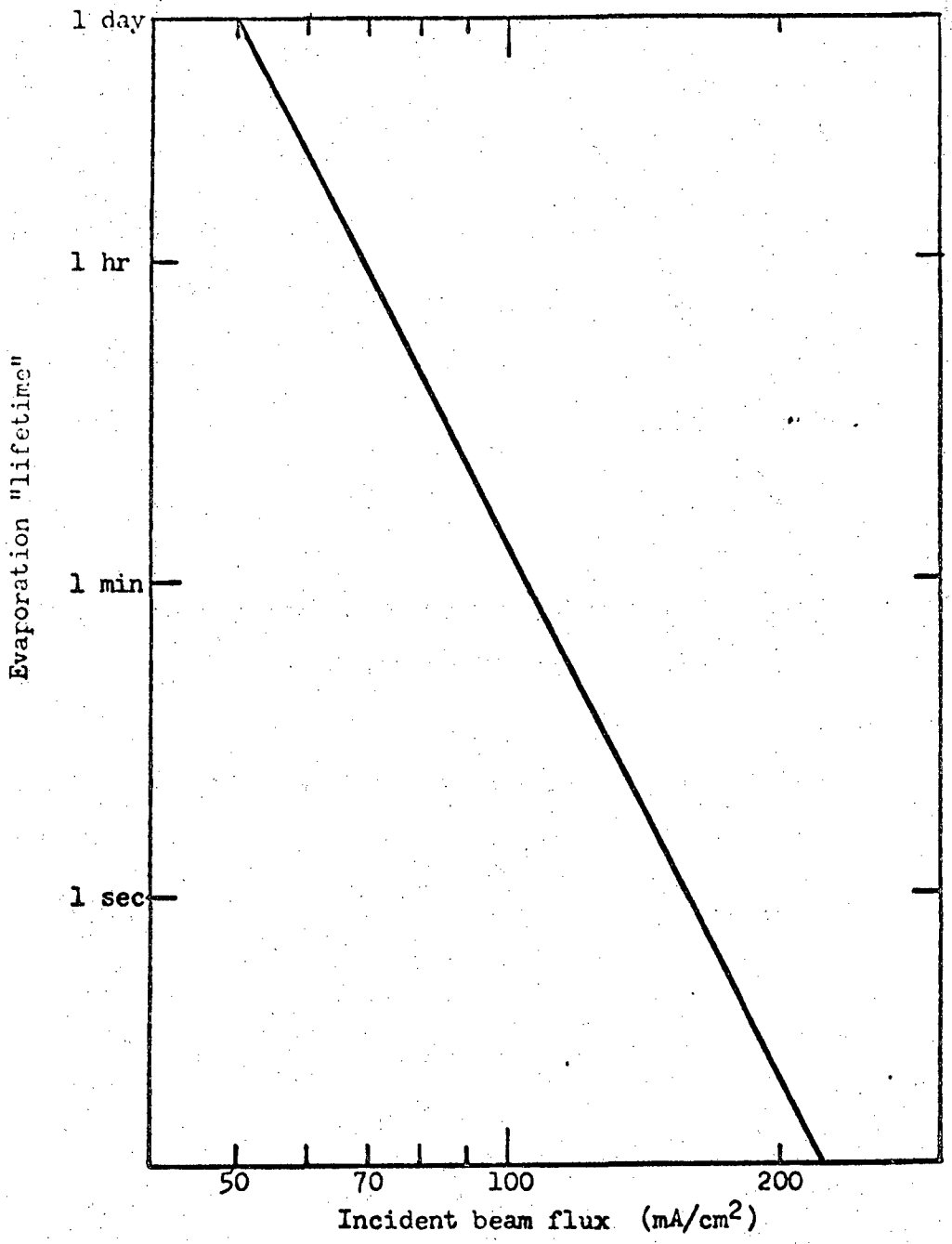

XBL 7012-7448

Fig. 40. Time to evaporate 10% of a 5 μg carbon foil vs incident beam flux.

H. Analysis of Published Data on 3914 Å Emission Cross Section

As can be seen in Figs. 25 and 26, there is a wide distribution in the values published for the 3914 Å emission cross section of molecular nitrogen. Essentially all of these curves have the same shape so the discrepancies probably arise from some systematic error that entered into their calculation independent of energy. A possible source of this error is an improperly calibrated standard light source.[71] As the emission cross section enters into the calibration of our optical system in the optical method, it is necessary for us to find some average value of this set of curves. Since the curves all have the same shape, we decided to average the curves at one energy (60 keV) and then draw an average curve through that point. Figure 41 shows the 60-keV values for five absolute measurements with their respective quoted uncertainties. In general the meaning of these uncertainties was not given. Also shown are five different mean values; as these different means differ by over 40%, I will explain the meaning of each and justify my choice of one of them.

A naive choice would lead us to one of the unweighted means. By taking an arithmetic mean, one implies that the function being averaged is best represented on a linear scale, that negative values of the function are possible, and that a value of 0.1 is much closer to zero than it is to 1. By taking a geometric mean, one implies that the function being averaged is best represented on a logarithmic scale, that negative values of the function are impossible and that 0.1 is closer to 1 than it is to zero.

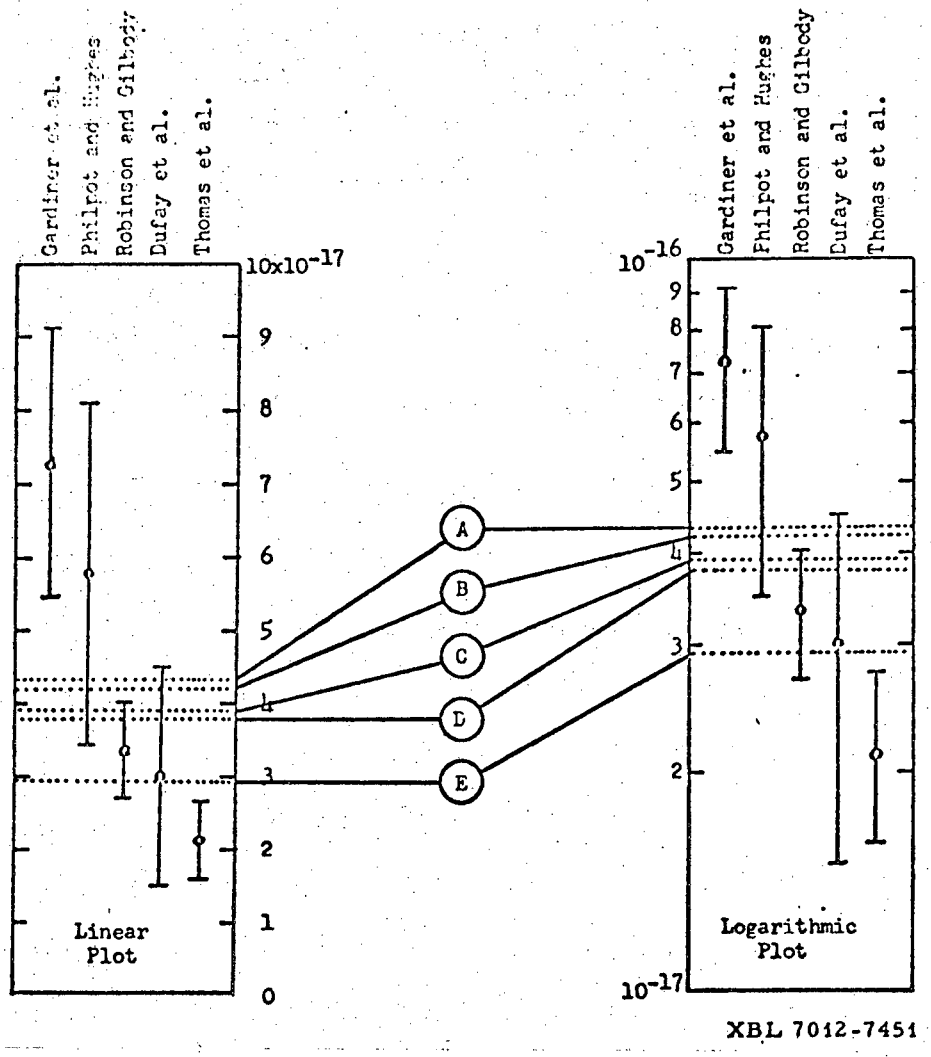

Fig. 41. 60-keV proton impact 3914 Å emission cross section as measured by five different experimenters. The error bars represent the reported uncertainties. The dotted lines show mean values obtained by the following methods: A, unweighted arithmetic mean; B, arithmetic mean weighted by the inverse square of the relative uncertainties; C, unweighted geometric mean; D, geometric mean weighted by the inverse square of the relative uncertainties; E, arithmetic mean weighted by the inverse square of the absolute uncertainties.

Since, however, we do have some error information, although we do not know what it means, we should make use of it. There are two possible weighting mechanisms; when one weights by the inverse square of the absolute error, one implies that an error of one unit should have equal weight whether the measured value is 1 ± 1 or 10 ± 1. Combined with an arithmetic mean, this gives the proper weighting for statistically distributed processes. When one weights by the inverse square of the relative error, one implies that it is the percentage error that is important. This is the proper weighting for a geometric mean.

From the nature of cross section measurements and from the fact that the distribution of points in Fig. 41 is determined by a systematic error and not a statistical error, I have decided to use a weighted geometric mean.

The equation for such a mean is

$$GM = \left(\prod_{i=1}^{n} x_i^{w_i} \right)^{\left[1/ \sum_{i=1}^{n} w_i \right]}$$

where

$$w_i = \frac{1}{(\text{percentage error in } x_i)^2}$$

and the value obtained for the cross section at 60 keV was 3.78×10^{-17} cm^2/molecule.

As can be seen in Fig. 26, there are only two absolute measurements of the cross section for emission due to H^0 impact; therefore, it

was decided to use the average value calculated for H^+ impact and relate it to H^0 impact by dividing it by the ratio of the 60 keV cross sections for the three authors who published data for both processes. This average ratio was 1.52, so the average curve for H^0 impact is normalized to 2.49×10^{-17} cm^2/molecule at 60 keV.

The uncertainty in the H^+ cross section assuming a 68% confidence interval is ±29%. To obtain the uncertainty in the H^0 cross section, one folds into this the uncertainty in the ratio of cross sections (±13%) and obtains ±31%. The cross section used im my calculations is a combination of the above weighted by the neutral fraction and therefore the uncertainty to be applied in my error calculation (Appendix C) is about ±30%.

FOOTNOTES AND REFERENCES

1. G. Gibson, W. A. S. Lamb, and E. J. Lauer, in Second United Nations International Conference on the Peaceful Uses of Atomic Energy (United Nations, Geneva, 1958), Vol. 32, p. 275.

2. R. F. Post, Ann. Rev. Nuclear Sci. 9, 367 (1959).

3. D. R. Sweetman, Nucl. Fusion 1962 Supplements, Part 1, p. 279.

4. J. R. Hiskes, Nucl. Fusion 2, 38 (1962).

5. R. N. Il'in, V. A. Oparin, E. S. Solov'ev, and N. V. Fedorenko, in Proceedings of the IVth International Conference on the Physics of Electronic and Atomic Collisions, Quebec, 1965 (Science Bookcrafters, Inc., New York, 1965); R. N. Il'in, V. A. Oparin, E. S. Solov'ev, and N. V. Fedorenko, Zh. Eksperim. i Teor. Fix., Pis'ma v Redaktsiyu 2, 310 (1965) English transl.: JETP Letters 2, 197 (1965) .

6. K. H. Berkner, W. S. Cooper III, S. N. Kaplan, and R. V. Pyle, Phys. Rev. 182, 103 (1969) and private communication.

7. B. A. Trubnikov and Yu. N. Yavlinskii, J. Exptl. Theoret. Phys. (USSR) 52, 1638 (1967) English transl.: Soviet Phys. JETP 25, 1089 (1967) .

8. G. J. McLelland, Production of Highly Excited Neutral Atoms by Charge Exchange in Solids, Ph. D. Thesis, School of Physics, University of Sydney, Sydney, Australia, 1968.

9. J. A. Phillips, Phys. Rev. 97, 404 (1955).

10. D. R. Sweetman, A. C. Riviere, and P. Hammond, in Culham Laboratory Progress Report CLM-PR-7, p. 47, 1964.

11. M. Kaminsky, Bull. Am. Phys. Soc. 13, 1405 (1968).

12. Carbon foils produced by Yissum Research Development Co., Jerusalem, Israel.

13. A. J. Summers, N. J. Freeman, N. R. Daly, in Proceedings of Nuclear Fusion Reactor Conference, Culham Laboratory, 1969, p. 347.

14. Yu. N. Yavlinskii, B. A. Trubnikov, and V. F. Elesin, Izv. Akad. Nauk SSSR ser fiz 30, 1917 (1966) English transl.: Bull. Acad. Sci. (USSR) Phys. Ser. 30, 1996 (1966).

15. K. W. Ehlers, The Use of Nitrogen Gas to Provide Vacuum, Lawrence Radiation Laboratory Report UCID-2595, 1965.

16. Liquid helium cryopump manufactured by Andonian Associates, Inc., Waltham, Massachusetts.

17. K. H. Berkner, B. R. Myers, and R. V. Pyle, Rev. Sci. Instr. 39, 1204 (1968).

18. K. H. Berkner, I. Bornstein, R. V. Pyle, and J. W. Stearns, Bull. Am. Phys. Soc. 13, 1562 (1968), and private communication.

19. R. N. Il'in, B. K. Kikiani, V. A. Oparin, E. S. Solov'ev, and N. V. Fedorenko, J. Exptl. Theoret. Phys. (USSR) 47, 1235 (1964) English Transl.: Soviet Phys. JETP 20, 835 (1965) .

20. R. L. Wax and W. Bernstein, Rev. Sci. Instr. 38, 1612 (1967).

21. A. L. Hunt, R. K. Goodman, G. L. Wegmann, and C. H. Robison, in Controlled Thermonuclear Research Annual Report, Lawrence Radiation Laboratory Report UCRL-50002-66-1, 1966, p. 45.

22. G. A. Sawyer, Rev. Sci. Instr. 23, 604 (1952).

23. T. W. Snouse, Appl. Phys. Letters 5, 122 (1964).

24. R. Hultgren, R. L. Orr, and K. K. Kelley, Supplement to Selected Values of Thermodynamic Properties of Metals and Alloys, Lawrence Radiation Laboratory Report

25. U. Haussr and W. Kerler, Rev. Sci. Instr. 29, 380 (1958).

26. D. C. Robinson, J. Sci. Instr. 44, 392 (1967).

27. C. H. Robison, Transmission Sputtering of Thin Films by Low Energy Hydrogen Ions, Ph. D. Thesis in Engineering-Applied Science, University of California, Davis, 1966.

28. J. L. Philpot and R. H. Hughes, Phys. Rev. 133, A107 (1964).

29. J. M. Robinson and H. B. Gilbody, Proc. Phys. Soc. (London) 92, 589 (1967).

30. M. Dufay, J. Desequelles, M. Druetta, and M. Eidelsberg, Ann. Geophys. 22, 619 (1966).

31. D. A. Dahlberg, D. K. Anderson, and I. E. Dayton, Phys. Rev. 164, 20 (1967).

32. E. W. Thomas, G. D. Bent, and J. L. Edwards, Phys. Rev. 165, 32 (1968).

33. N. P. Carlton and T. R. Lawrence, Phys. Rev. 109, 1159 (1958).

34. H. A. B. Gardiner, W. R. Pendleton, Jr., J. J. Merrill, and D. J. Baker, Phys. Rev. 188, 257 (1969).

35. J. R. Sheridan and K. C. Clark, Phys. Rev. 140, A1033 (1965).

36. R. J. McNeal and D. C. Clark, J. Geophys. Res. 74, 5065 (1969).

37. W. F. Sheridan, O. Oldenberg, and N. P. Carlton, in Second International Conference on the Physics of Electronic and Atomic Collisions, Boulder, Colorado, 1961, p. 159.

38. J. R. Hiskes and C. B. Tarter, Radiative Transition Probabilities in Hydrogen, Lawrence Radiation Laboratory Report UCRL-7088 Rev. I, 1964.

39. A. C. Riviere, in Proceedings of Symposium on Atomic Collision Processes in Plasmas, Culham, 1964, Atomic Energy Research Establishment Report AERE-R-4818, p. 124.

40. Measured by J. G. Conway of Lawrence Radiation Laboratory, Berkeley.

41. D. S. Bailey, J. R. Hiskes, and A. C. Riviere, Nucl. Fusion 5, 41 (1965).

42. A. Van Wijngaarden and H. E. Duckworth, Can. J. Phys. 40, 1749 (1962).

43. B. A. Trubnikov and Yu. N. Yavlinskii, J. Exptl. Theoret. Phys. (USSR) 48, 253 (1965); English Trans.: Soviet Phys. JETP 21, 167 (1965).

44. J. Linhard and M. Scharff, Phys. Rev. 124, 128 (1961).

45. H. E. Schiott, Mat. Fys. Medd. Dan. Vid. Selsk. 35, No. 9 (1966).

46. K. Morita, H. Akimune, and T. Suita, J. Phys. Soc. Japan 25, 1525 (1968).

47. Ya. A. Teplova, V. S. Nikolaev, I. S. Dmitriev, and L. N. Fateeva, J. Exptl. Theoret. Phys. (USSR) 42, 44 (1962); English Trans.: Soviet Phys. JETP 15, 31 (1962).

48. Yu. V. Gott and V. G. Tel'kovsky, Radiotekhn. i Electron. 7, 1956 (1962); English Trans.: Radio Engineering and Electronic Physics 7, 1813 (1962).

49. H. Bätzner, Ann. Physik 25, 233 (1936).

50. V. G. Tel'kovskii and V. I. Pistunovich, Doklady Akad. Nauk (USSR) 113, 1035 (1957); English Trans.: Soviet Phys. Doklady 2, 184 (1957).

51. W. White and R. M. Mueller, J. Appl. Phys. 38, 3660 (1967).

52. J. H. Ormrod, J. R. Macdonald, and H. E. Duckworth, Can. J. Phys. 43, 275 (1965).

53. R. L. Wolke, W. N. Bishop, E. Eichler, N. R. Johnson, and G. D. O'Kelley, Phys. Rev. 129, 2591 (1963).

54. S. K. Allison and S. D. Warshaw, Rev. Mod. Phys. 25, 779 (1953).

55. R. R. Hart, F. W. Reuter III, H. P. Smith, Jr., and J. M. Khan, Phys. Rev. 179, 4 (1969).

56. R. R. Hart, Characteristic Oxygen K-shell X-ray Production in Thin Films of Aluminum Oxide by 20- to 100-keV Protons, Ph. D. Thesis in Engineering Science, University of California, Berkeley, 1967.

57. A. H. Morton, D. A. Aldcroft, and M. F. Payne, Phys. Rev. 165, 415 (1968).

58. M. Bader, R. E. Pixley, F. S. Mozer, and W. Whaling, Phys. Rev. 103, 32 (1956).

59. J. H. Ormrod and H. E. Duckworth, Can. J. Phys. 41, 1424 (1963).

60. R. D. Moorehead, J. Appl. Phys. 36, 391 (1965).

61. C. A. Sautter and E. J. Zimmerman, Phys. Rev. 140, A490 (1965).

62. E. M. Zarutskii, Fiz. Tverdogo Tela 9, 1500 (1967); English Trans.: Soviet Phys. Solid State 9, 1172 (1967).

63. G. F. Bogdanov and F. V. Lebedev, Atomnaya Energiya 23, 347 (1967); English Trans.: Soviet Atomic Energy 23, 1096 (1967).

64. A. A. Bednyakov, V. N. Dvoretskii, I. A. Savenko, and A. F. Tulinov, J. Exptl. Theoret. Phys. (USSR) 46, 1901 (1964); English Trans.: Soviet Phys. JETP 19, 276 (1964).

65. Yu. V. Gott and V. G. Telkovskii, in 8th International Conference on Phenomena in Ionized Gases, 1967 (IAEA, Vienna, 1967), p. 53.

66. A. A. Bednyakov, A. N. Boyarkina, I. A. Savenko, and A. F. Tulinov, J. Exptl. Theoret. Phys. (USSR) 42, 740 (1962); English Trans.: Soviety Phys. JETP 15, 515 (1962).

67. A. A. Bednyakov, V. N. Dvoretskii, I. A. Savenko, and A. F. Tulinov, Vestn. Mosk. Univ., Ser. III Fiz. Astron. 1, 55 (1965).

68. J. D. Jackson, Classical Electrodynamics (J. Wiley and Sons, Inc., New York, 1962), pp. 456-459.

69. R. S. Pease, Rendiconti S. I. F. Corso 13, 158 (1960).

70. G. K. Wehner, Phys. Rev. 93, 633 (1954).

71. H. A. B. Gardiner, private communication.

TECHNICAL INFORMATION DIVISION
LAWRENCE RADIATION LABORATORY
UNIVERSITY OF CALIFORNIA
BERKELEY, CALIFORNIA 94720